RadioOnkologie und Strahlentherapie

Targeted Irradiation of Mitochondria

Dietrich Wyndham Michael Walsh

Vollständiger Abdruck der von der Fakultät für Medizin der Technischen Universität München zur Erlangung des akademischen Grades eines

Doktors der Naturwissenschaften

genehmigten Dissertation.

Vorsitzende(r): Prof. Dr. Martin Göttlicher

Prüfer der Dissertation:

1. Priv.-Doz. Dr. Thomas E. Schmid
2. Prof. Dr. Gabriele Multhoff
3. Prof. Dr. Lisa Wiesmüller

Die Dissertation wurde am 25.09.2017 bei der Technischen Universität München eingereicht und durch die Fakultät für Medizin am 21.02.2018 angenommen.

Targeted Irradiation of Mitochondria

Dissertation

zum Erwerb des Doktorgrades der Naturwissenschaften Dr.rer.nat

an der Medizinischen Fakultät

der Technischen Universität München

Von

Dietrich Wyndham Michael Walsh

2017

Table of contents

Abbreviations

AIFIRA	Applications Interdisciplinaires de Faisceaux d'Ions en Région Aquitaine
ADP/ATP	Adenosinediphosphate, Adenosinetriphosphate
CCD	Charge coupled detector
CsA	Cyclosporin A
DAPI	4′,6-Diamidin-2-phenylindol
DNA	Deoxyribonucleic acid
DTT	Dithiothreitol
ETC	Electron transport chain
FCCP	Carbonyl cyanide-4-(trifluoromethoxy) phenylhydrazone
Gy	Gray; Unit for radiation dose (Joule/kg)
IMM	Inner mitochondrial membrane
IMS	Intermembrane space
LCI	Live cell imaging
LET	Linear energy transfer
MM	Mitochondrial matrix
MTG	MitoTracker Green
MTP	Mitochondrial transition pore
OMM	Outer mitochondrial membrane
PI	Propidium iodide
ROI	Region of interest
ROS	Reactive oxygen species
S:N	Signal to noise ratio
SNAKE	Superconducting Nanoprobe for Applied nuclear (Kern) physics Experiments
SOD	Superoxide dismutase
STED	Stimulated emission depletion microscopy
TMRE	Tetramethylrhodamine ethyl ester
TPP+	Tetraphenylphosphonium
$\Delta\Psi m$	Mitochondrial membrane potential

Abstract

Targeted mitochondrial irradiation has been performed using protons and carbon ions at two separate ion microbeam facilities. Live cell imaging of mitochondria in cancerous and non-cancerous cells has been developed and performed to analyze mitochondrial factors *in situ.* Among the traits analyzed are mitochondrial membrane potential (polarization state), mitochondrial membrane integrity, plasma membrane integrity and mitochondrial reactive oxygen species production. The results from the experiments have shown that polarized and functional mitochondria can be depolarized and deactivated by targeted irradiation with both protons and carbon ions. The results indicate that the total energy deposited in the mitochondria is the factor which dictates the mitochondrial depolarization response not the particle specific LET. In addition there was no sign of mitochondrial membrane integrity change or plasma membrane integrity change after irradiation. The targeted irradiation and concurrent live cell imaging of mitochondria has also enabled the detection of mitochondria specific superoxide (O_2^-) production during irradiation. In conclusion, this thesis is the first documentation of targeted irradiation of mitochondria and the radiation induced superoxide production and mitochondrial depolarization following irradiation.

Motivation

This thesis will explore the role of mitochondria in the cellular response to ionizing radiation. The thesis covers the background of mitochondrial biology in form and function, the experimental ion microbeam setups used to perform targeted irradiation. The experiments performed and the insights gained from these experiments will enable a deeper understanding of mitochondrial radiation sensitivity and response to ionizing radiation.

Mitochondria are an organelle of interest in all fields of biology today due to their pivotal roles in energy homeostasis and cell death, radiation biology is no exception to this. However, radiation biology has, in the last decades focused mainly on the investigation of the nuclear (DNA) response to ionizing radiation, instead of investigating a specific organelles response. This thesis is the first of its kind to use targeted irradiation to investigate a novel and interesting field of study of organelle specific radiation response. The detection of a specific response of an organelle as diverse in its form and function as mitochondria is a challenge, as they do not only change their form (length and interconnectivity) irrespective of cell cycle but are, in their smallest form, in the range of 1µm. There are therefore only few labs worldwide who have the technical capabilities necessary to investigate the radiation induced mitochondrial response in individual mitochondria. The microbeam facilities SNAKE (Superconducting Nanoprobe for Applied Nuclear (Kern) physics Experiments) and AIFIRA (Applications Interdisciplinaires de Faisceaux d'Ions en Région Aquitaine) used in this paper had beam spot resolutions of <1 and 2 micrometer respectively, which are below the mitochondrial size enabling targeted irradiation.

The biological methods employed to investigate the mitochondrial response to irradiation were focused on live cell imaging of mitochondria *in situ* using fluorescence microscopy. The individual mitochondrial traits that have been analyzed were mitochondrial membrane potential, membrane integrity and reactive oxygen species (ROS) production. These factors are key mitochondrial traits known to have adverse effects on cellular function and survival when altered. To the authors knowledge this thesis is the first example of targeted irradiation of mitochondria and the accompanying publication was also the first on this topic. As mitochondria make up a large area of the cytoplasm of cells the radiation induced effects on mitochondria are of interest to fully understand the cellular response to ionizing radiation.

The ability to deposit a defined number of ions in highly localized areas of cells enables the quantification of energy deposited and will enable not only a more detailed insight into the mitochondrial response to ionizing radiation but also will enable the investigation of other subcellular organelles in future. The damage caused by a known number of ions gives a greater insight into the susceptibility of the biological system to ionizing radiation induced stress. Ion beam irradiation stands in contrast to similar targeted laser treatment of organelles, however the energy absorbed in the biological sample from laser irradiation is largely unknown and not quantifiable. Ion beam irradiation therefore offers a more selective and quantifiable approach to radiation induced damage in subcellular compartments.

In conclusion this thesis presents conclusive and novel evidence that targeted irradiation of subcellular organelles, in this case mitochondria, has the ability to probe not only their inherent radio sensitivity but also fundamental biological response to stress.

1. Mitochondria

The origin of mitochondria in eurkaryotic cells has been the topic of much research and discussion in the academic community since the first discovery of these subcellular organelles in the 1840s (Ernster and Schatz, 1981). Mitochondria from the Greek “mitos” for threads and “chondros” for granules, are vital to all eukaryotic cells, apart from the recently discovered Monocercomonoides genus (Karnkowska et al.). Mitochondria play a vital role in the cells in which they are contained in as they are the main site of many homeostatic processes vital to cell survival. The endosymbiotic theory of mitochondrial uptake into the predecessors of eukaryotic cells as we know them today is however the prevailing theory. The origin of mitochondria dates back to the evolution of the eukaryotic cell. Mitochondria have many bacterial traits, such as their double membrane, overall size (µm range) and circular DNA genomes. Most of the evidence in the literature points towards a bacterial origin of the mitochondrial genome, specifically from α-proteobacteria (Gray et al., 2001). This endosymbiotic theory explains the arrangement of early α-proteobacteria and the eukaryotic cell which yielded a relationship, which, over the evolution of the mitochondrial genome and the adaptation to its surroundings, has made mitochondria the major source of cellular energy, Adenosinetriphosphate (ATP) in modern day eurkaryotic cells. ATP is the main source of energy for all cellular processes and all cells rely heavily on readily available amounts of ATP produced by mitochondria.

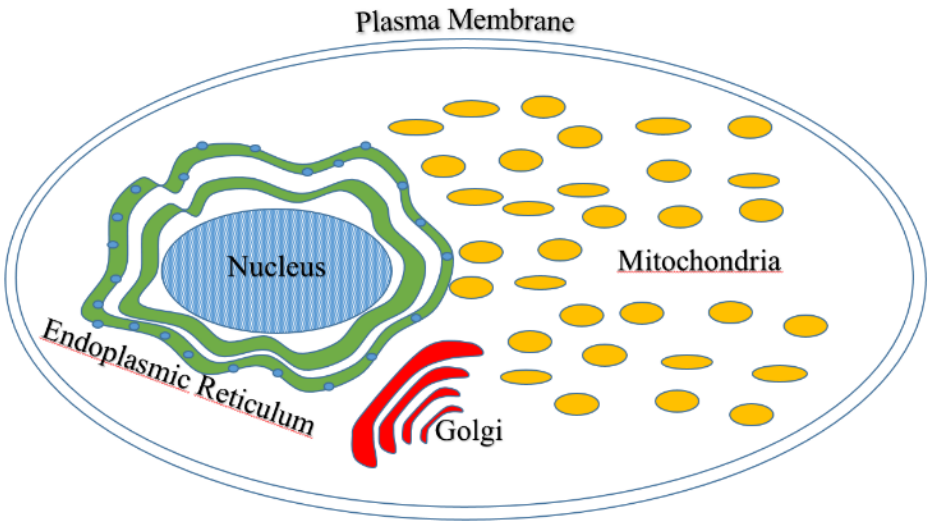

Fig.1: Overview of a mammalian cell depicting a rudimentary cell with the nucleus, mitochondria, endoplasmic reticulum and golgi marked in orange, green and red respectively.

Understanding the origin of mitochondria is useful as it enables us to begin to understand how mitochondrial structure, originating from that of the α-proteobacteria, enables its function in all mitochondria containing cells. Mitochondria do not just present the only other source of DNA genomes outside the nucleus in the form of double stranded circular 16.6kbp DNA packed densely folded around proteins forming individual "nucleoids". The genomes of mitochondria encode 13 of the 80 required proteins all of which are vital to the function of mitochondria as they provide the majority of all the cell's energy requirement in the form of ATP (Chen and Butow, 2005). Mitochondria perform a vast array of biochemical reactions involved in glucose metabolism, lipid metabolism (Alaynick, 2008) and apoptosis (Wang and Youle, 2009), just to name a few. These subcellular organelles, which are between 0.2-0.5µm in width, and can be longer than 10µm in some cases, make up a large proportion of the cytoplasm. Mitochondrial morphology is also a complex matter as mitochondria replicate via fission and fusion irrespective of the cell's DNA replication (cell cycle). Networks of interconnected mitochondria can form containing a large number of nucleoids (mitochondrial genomes) in a single interconnected functional mitochondrial strand. In other circumstances mitochondria can present themselves as spherical blobs throughout the cell and any variation of these two morphologies can exist in a single cell at one time. This heterogeneity in structure of mitochondria in cells has been well documented in the literature (Collins and Bootman, 2003). In addition to morphological diversity, the inherent mitochondrial form is a key to its functional ability. Mitochondria have a double phospholipid membrane with an intermembrane space (IMS) and a mitochondrial matrix (MM) (Fig.2). Proteins, which are part of the respiratory complex chain, are integrated into the inner mitochondrial membrane. These proteins are vital for cellular energy metabolism as they are involved in the production of ATP in the cell. More fundamentally however, these proteins regulate the flow of H^+ between the MM and the IMS. The regulation of the proton gradient and thus ATP production can only be generated when the H+, which have been pumped out of the MM by the electron transport chain, re-enter through the ATP synthase enzyme which acts as a membrane channel. The process enables ATP synthase to synthesize ATP from Adenosine diphosphate (ADP) and a free phosphate group to form ATP via its enzymatic activity and is shown in Fig.2.

The protons pumped across the Inner mitochondrial membrane (IMM) cause a potential difference (ΔV) between the IMS and the MM. This potential difference across the mitochondrial membrane is known as the mitochondrial membrane potential ΔΨm, and mitochondria which maintain such a potential are classified as "polarized" and functional. ΔΨm is maintained as long as the electron transport chain is functional. This unique characteristic of mitochondrial membranes and proton pumping makes this membrane the one with the highest electric field across it in the whole cell. The magnitude of the membrane potential is in the range of 100-180mV (Gan et al., 2011, Gerencser et al., 2012) depending on cell type and measurement accuracy. The electron transport chain (ETC) is the core mechanism by which mitochondria can produce ATP. By making use of the protein complexes in the mitochondria's membrane, protons can be pumped across the mitochondrial membrane and can be used by ATP synthase to convert Adenosinediphosphate (ADP) and free phosphate (p_i) into ATP.

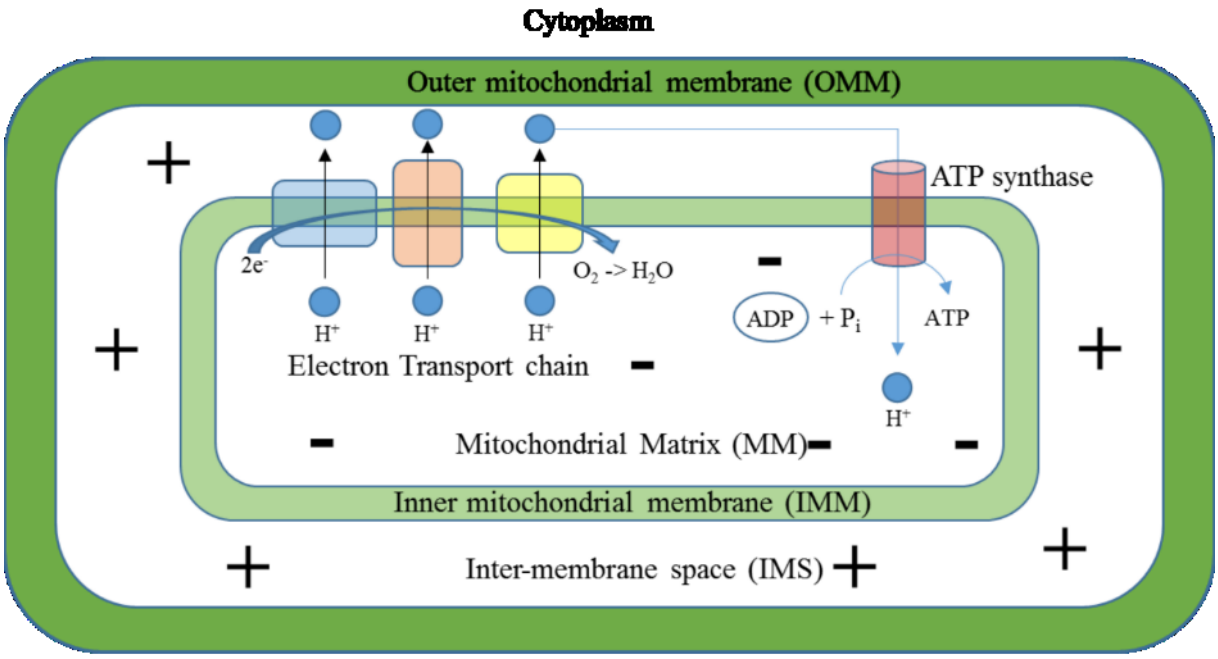

Fig.2 A depiction of the mitochondrial membrane organization, outer, inter membrane space and inner membrane, along with a simplified representation of the charge distribution in the mitochondria (+ and -). The electron transport chain is made up of a variety of proteins which pump protons across the membrane to enable the influx of protons via the ATP synthase channel, which in turn catalyzes the production of ATP from ADP.

This membrane potential of the mitochondria is a direct indicator of mitochondrial function since without an active membrane potential, mitochondria cannot perform the necessary metabolic processes to create ATP. The loss of membrane potential on the other hand is termed depolarization and is involved in processes surrounding cellular damage and death. The magnitude of ΔΨm is also an indicator of other cellular processes, as ΔΨm tends to zero when mitochondria depolarize in such processes as apoptosis, for example. Short term changes in membrane potential have also been observed and there is much controversy about the existence of short term depolarization events followed by repolarization events, which have been termed "flashes" (Wang et al., 2016). The original proposal for the mechanism was that these flashes were bursts of superoxide (O_2^-), however there is some controversy concerning this phenomenon as other groups cannot reproduce this work and it is more likely linked to short and sharp changes in mitochondrial pH (Schwarzländer et al.)

In order to maintain ATP production mitochondria have a high potential difference across their membranes, however this comes at a cost, as the process of producing ATP in large amounts has the side effect of reactive oxygen species formation. Reactive oxygen species (ROS) are formed in large quantities in mitochondria. Inside mitochondria, ROS in the form of superoxide is formed by the reduction of molecular oxygen via proteins in the respiratory chain complex which fundamentally convert glucose and oxygen into ATP (Murphy, 2009). However a high level of O_2^- maintained for a long period would soon lead to the demise of a cell and so the mitochondria use their own superoxide

dismutase enzyme (SOD) which converts O_2^- into H_2O_2 and O_2 to remedy the overproduction of damaging ROS. The production of ROS in mitochondria is a direct result of the regulatory and metabolic process in the mitochondria. The disruption of the regulatory processes has been linked to a variety of different diseases and aging (Raha and Robinson). Mitochondrial diseases usually manifest themselves in a wide variety of severe conditions with symptoms ranging from muscle loss, weakness, problems with vision and hearing, liver and kidney disease and dementia to name a few. An example of mitochondrial disease includes Wilsons disease in which high amounts of copper accumulate and cannot be cleared from the mitochondria leading to neurological problems and liver failure (Rodriguez-Castro et al., 2015). Keeping mitochondrial function in balance is therefore vital for health as any change to the delicate balance of the mitochondrial factors involved in energy metabolism can lead to major changes in the cells fate.

Not only the structure of mitochondria shows heterogeneity, but also other facets such as membrane potential (Kuznetsov et al., 2006), function and homeostasis (Andrey and Raimund, 2009). This heterogeneity in form and function indicates that the mitochondria, in a single cell may perform a variety of different tasks depending on where they are located and at what level they are currently working. This level of inherent complexity still leaves many unanswered questions about mitochondria even though they are arguably the subcellular organelle with the most associated Nobel Prizes (Pagliarini and Rutter, 2013). Every field of biology would therefore benefit from more in-depth knowledge of the mitochondrial function and a greater understanding of their responses to stimuli. Microbeams offer a highly precise and quantifiable method to manipulate individual mitochondria which will enable a way of analyzing individual mitochondria without the use of chemical inhibitors or reagents to invoke a mitochondrial response.

2. Mitochondria in radiation biology

The cytoplasm, and in particular mitochondria, have played a rather minor role in the field of radiation biology research. The central dogma of the field has been the radiation induced damage to the nucleus in the form of DNA damage (Waldren, 2004). Early experiments with radionuclides attached to different parts of the cell concluded that the nucleus was the site responsible for radiation induced division delay, rather than the cytoplasm (R.L. Warters, 1977). Moreover, the vast majority of radiation biology experiments analyse either whole cell or nuclear DNA responses after broad beam irradiation. This focus on DNA however does not mean that radiation biology has completely ignored cytoplasmic components and their interaction with ionizing radiation. In 1953, Zirkle and Bloom irradiated the cytoplasm of cells with 2 Mev protons and 4 Mev α-particles and discovered that the cytoplasm was in fact relatively resistant to the damaging effects of radiation when analysing cell survival (Zirkle and Bloom, 1953). Results from cytoplasmic irradiation using alpha particles show little to no change in survival, but may lead to increased nuclear DNA mutations (Wu et al., 1999). The latest preliminary results from the Japanese Photon Factory team indicates that cytoplasmic irradiation has no cell-killing effect when irradiated using X-ray microbeams (5.35keV) (Masao Suzuki, 2015). The cytoplasm is however a complex milieu to study as it is the space in which the majority of cellular processes take place. Unlike the nucleus it is therefore highly heterogeneous as it contains a variety of organelles (mitochondria, golgi, endoplasmic reticulum) and a vast array of proteins. Therefore an analysis of cellular response to cytoplasmic radiation may yield some valuable information however the source of that response will still be unknown as many different entities have been irradiated. Understanding each individual organelles response to radiation is however a daunting task as it requires not only highly precise deposition of radiation but also a readout system capable of capturing and analyzing the response after organelle specific irradiation.

Due to technical limitations of beam size and energy, the ability to target individual cytoplasmic constituents with ionizing radiation only became an option with the advent of microbeam technology. Before the widespread use of microbeams a lot of work was performed using lasers to induce highly localized damage. The advent of the ruby red lasers in the 1960's lead to the early work using lasers to irradiate mitochondria. In the early experiments, transmission electron microscopy (TEM) was used to look at the morphological changes after laser irradiation of mitochondria (Tanaka, 1969). Several groups then tried to classify what effects this kind of mitochondria specific irradiation had on function by irradiating cardiomyocytes to see if there was a functional change (Berns et al., 1972). The use of fluorescence markers for mitochondrial activity (Rhodamine 123) then enabled an analysis of membrane potential after laser irradiation which showed that laser ablation could lead to loss of membrane potential, interpreted as bleaching (Siemens et al., 1982, Amchenkova et al., 1988). Most recently femtosecond lasers have been used to probe the cytoplasmic and mitochondrial responses to laser irradiation.

Femtosecond lasers deposit large amounts of energy in small application spots in very short pulses of time. Femtosecond laser ablation has been used to target organelles (Watanabe et al., 2004) and specifically mitochondria (Shen et al., 2005, Watanabe et al., 2005). Laser irradiation, and consequent depolarization of an individual mitochondria was shown, in addition no effect on cell division was visible when applying millions of individual nano Joule pulses of energy to each diffraction limited spot (Shimada et al., 2005). Femtosecond laser irradiation has been used to induce apoptosis and cell membrane disruption along with a calcium signaling response (Jonghee et al., 2015). Although these experiments shed light on the cytoplasmic and mitochondrial responses to targeted irradiation, energy deposition by lasers in the cells is hard to quantify due to a mix of linear and non-linear interactions of photons with matter. In contrast to ionizing radiation using ions, track structure and linear energy transfer (LET) can be used to determine the amount of energy deposited in a volume of interest. Therefore it remains to be elucidated if the laser experiments are in any way directly comparable, in terms of energy deposited and response, with ionizing radiation experiments performed with particles and X-rays using microbeams.

Microbeams have been a key technological advancement that have enabled a highly localized probing of the cell's inherent response to ionizing radiation. Even with such fine tools available, the majority of research in the field has still focused on the nucleus. The reason for this is that even relatively small doses to the nucleus cause cell death. The interaction of ionizing radiation with DNA has been studied extensively and two main DNA repair pathways have been discovered (Hakem, 2008). The overall cellular response to broad beam irradiation has also been highly characterized for cellular survival by many groups. The few select papers which have covered cytoplasmic irradiation, claimed to have found nuclear effects after cytoplasmic irradiation, such as 53BP1 relocalization (Tartier et al., 2007), genomic instability (Zhang et al., 2014) and bystander effects in surrounding cells (Hongning et al., 2009, Shao et al., 2004). So far the mitochondrial response to cytoplasmic irradiation has been investigated by the Hei group at Columbia University. In their study they documented cytoplasmic deposition of α-particles and the consequent effects on mitochondrial fission/fusion, ROS production and morphological dynamics (Zhang et al., 2013). However the results are based on non-targeted irradiation so the statistical power of such small-number experiments, combined with the lack of evidence of specific mitochondrial traversal of the particles and the strong mitochondrial heterogeneity already present in cells, opens up the field for more detailed investigation. The limited number of microbeam facilities capable of performing these experiments and the large amount of technical knowledge required to perform such targeted irradiation means that progress is slow. The next logical steps would be to model the process of energy deposition in mitochondria to facilitate a deeper understanding into the processes seen after targeted irradiation and motivate further experiments into this area. Modelling of effects based on known parameters could be a great initial source of knowledge as mitochondria contain DNA, membranes and protein machinery that can all be damaged by ionizing radiation.

Modelling efforts based on particle track structure have been realized by the group of Friedland at the Helmholtz Zentrum München relating to the damage of nuclear and mitochondrial DNA (Schmitt, 2016).

The interaction and effect of ionizing radiation on the mitochondrial genome is, however, yet to be experimentally observed. The classical radiation-induced double strand break (DSB) in the nucleus, as can be labelled with the repair marker γH2AX, is not present in mitochondria and nor are there any studies claiming to have visualized DSB repair proteins in mitochondria. Due to the lack of double and single stranded repair proteins specific to the mitochondria, there has been a lack of understanding of the repair processes. The most recent findings indicate that there is no mitochondria-specific DNA DSB repair protein set (Alexeyev et al., 2013) and the same proteins that are found in the nucleus may be imported to the mitochondria from the nucleus (Mitoworld Congress meeting 2016). An alternative hypothesis is that the sheer amount of mtDNA (mitochondrial DNA) genomes present in a cell means that repair of mtDNA is not a priority as old, damaged mitochondria can be removed and replication of undamaged mitochondria can replace the damaged organelles. There is however evidence for a variety of other DNA damage repair mechanisms including single strand break (Alexeyev et al., 2013) and base excision repair (Prakash and Doublié, 2015). Therefore mitochondrial DNA damage is of interest, as inducing double strand breaks in all mitochondrial genomes could well lead to relative mitochondrial chaos as the genes encoded on the 16.6kb genome are unable to be read and transcribed. It is therefore evident that assessing the mitochondrial response to ionizing radiation is highly complex and requires interdisciplinary teams including physical setups and modelling.

A recent paper used a Web of Science (Thomson Reuters) query to analyse the prevalence of studies highlighting ionizing radiation damage to mitochondria compared to the nucleus (Fig.3). The study found that between 1990 and 2013 the published literature in the form of “Articles” showed that there were ~9x more articles concerning the nucleus then the mitochondria in the field of radiation biology (Kam and Banati, 2013).

Given the limited number of institutions able to tackle such a complex task as targeted mitochondrial irradiation, it is not surprising that there is not a large amount of documented research into this cellular component. However, despite the difficulty it demonstrates that there is an interest from the radiation biology community.

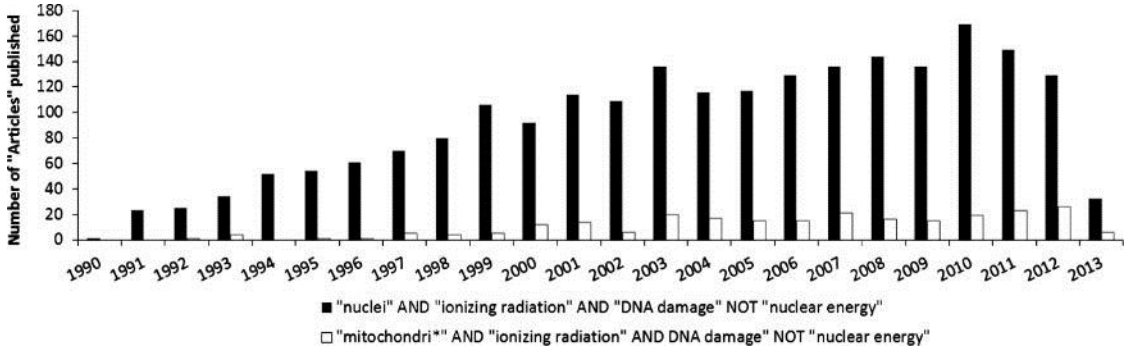

Figure.3 Histogram depicting the number of "Articles" in the field of radiation which involve research into the nucleus as compared to those with mitochondrial theme. The figure was taken from (Kam and Banati, 2013)

3 Ions, accelerators and charged particle microbeams

3.1 Ions

An ion is an atom or molecule within which the number of electrons and protons are not equal yielding either a net positive or negative charge on the atom. This charged state of an ion enables particle accelerators to make use of the inherent charged state of the ion to accelerate the ions using high electric fields, such as are created inside particle accelerators. Production of charged ions can be performed by physical or chemical means however for the sake of this body of work the production of ions will not be covered. Depending on the ions that need to be accelerated the types of sources vary, for the work contained in this thesis, a gas ionization source was used for protons and a sputter ion source for carbon ions. Carbon ions and protons were used in the experiments as the setup for live cell targeted irradiation is built around the physical properties of carbon ions. The 55 MeV carbon ions for example, are able traverse the targeted cell and are stopped in the scintillator below the cells to allow for detection of single ion application.

3.2 Accelerators

Particle accelerators have been fundamental tools used for decades in particle physics and material sciences to probe atomic structure of atoms or to analyse materials of unknown composition using a variety of techniques such as elastic recoil detection, Rutherford backscattering and particle-induced X-ray emission. More recently biologists and biophysicists have made use of accelerators as a source of ions for radiobiological research and for particle (proton or carbon ion) therapy. The ability to focus, control and count ions has meant that accelerators and experimental setups in the form of microbeam lines are capable of depositing known numbers of ions to highly defined micrometer sized beamspots and are therefore capable of probing the inherent radiation responses of cells in unprecedented detail.

Particles accelerators are the essential component behind all experimental microbeam setups. Particle accelerators fall into two categories; the electrostatic accelerators and the electrodynamic accelerators. For the sake of this body of work only electrostatic particle accelerators will be covered. Electrostatic particle accelerators can further be sub-divided into two categories; single end machines and tandem accelerators. The microbeams used for experiments in this work cover both categories: the Applications Interdisciplinaires de Faisceaux d'Ions en Région Aquitaine (AIFIRA) beamline is based around a single end accelerator; and the Superconducting Nanoprobe for Applied Nuclear (Kern) Experiments (SNAKE) is based on a tandem setup.

3.2.1 Single end

Single end accelerators were first introduced in 1932 by Cockcroft and Walton and work by producing a high voltage at a single static terminal at one end of the accelerator (J. D. COCKCROFT, 1932). Positively charged ions are injected into the accelerator and accelerated towards the high voltage terminal after which they exit the accelerator and can enter the evacuated beam tube. Single end accelerators are therefore capable of achieving high count rates of ions exiting the accelerator as there is only a single accelerator step and no stripping of electrons is needed. The AIFIRA beamline is based on a high voltage engineering single end machine with 3.5 MV terminal voltage (Sorieul et al., 2014).

3.2.2 Tandem

Unlike single ended accelerators tandem accelerators make use of negatively charged ions at the ground (entry) and then accelerate the negative ions towards a positive terminal at the center of the accelerator. Here the ions are stripped of all (in the case of light ions) or a certain fraction of their electrons by way of a gas or solid “stripper” material so the ions become positively charged. These now positively charged ions are then accelerated towards the ground potential and exit the tandem as positively charged and highly energetic, fast ions. The beam of ions is therefore accelerated in two stages, and hence the word “tandem” (Graaff, 1960). The SNAKE beamline is based around The Munich MP tandem accelerator at the Maier Leibnitz Laboratory (MLL) with a terminal voltage of up to 14 MV (Assmann et al., 1974).

3.3 Charged particle microbeams

Ion microbeams are a class of beam lines used for a variety of applications ranging from material sciences to radiation biology and are classified by their beam spot sizes in and below the µm range. At the time of writing, the International Atomic Energy Association (IAEA) accelerator knowledge portal (https://nucleus.iaea.org/sites/accelerators/Pages/default.aspx) lists 50 electrostatic accelerators with microprobes (microbeams) worldwide. Of these 50 microprobes, 11 are known to the microbeam community to be used for biological experiments (Barberet and Seznec, 2015). The focusing of the ions is usually performed over multiple stages using beam slits to collimate the beam and focusing magnets (sometimes superconducting) to further fine tune the beam to produce beamspots in the micrometer range. There are also examples of microbeams that use glass capillaries to cut the beam to the micrometer scale, however they offer a much reduced countrate, larger beam diameter and less flexible scanning possibilities (Jin et al., 2013). Fundamentally the mechanism by which each beamline focusses the beam may vary but to be a microbeam a micron range beamspot is required. The ability, not just to focus but also to count individually applied ions in a targeted fashion, is further limited to a few institutions worldwide of which the SNAKE facility in Munich is one of them. This microprobe is therefore an ideal candidate for analyzing cellular reponses to ionizing radiation as the beamspot is in the range of the subcellular components of a cell, such as mitochondria for example, and the energy deposited in the targeted area is quantifiable. This has situated microbeams as a key tool in the field of radiation biology and enables unprecedented experimental approaches

3.4 SNAKE

The charged particle microbeamline SNAKE is an experimental setup at the Maier Leibnitz Laboratory (MLL) in Munich Germany. The experimental setup is built up around a 14 MV tandem accelerator (Fig.4). The microbeam itself has a beamspot with an irradiation spot size of <1µm (Hable et al., 2009) and is capable of depositing counted individual ions to user defined irradiation points on biological samples.

The beam exiting the accelerator and analysed by a 90° deflection magnet is then collimated using deflection plates in the x and y directions into a beam of roughly 20x10µm. This beam is then further collimated in its angular divergence before it reaches the superconducting lens. What makes SNAKE unique is the focusing stage which employs a superconducting triplet of quadropole magnets which are maintained in a liquid helium cryostat (Hinderer et al., 1997). This secondary focusing element enables a fine tuning of the particles trajectory allowing the beam to be further collimated in x and y directions. Finally leading to a sub-micron beamspot as measured in air outside of the beam exit window. It is the only facility of its kind that combines such a fine beam size with a tandem accelerator of such a high voltage.

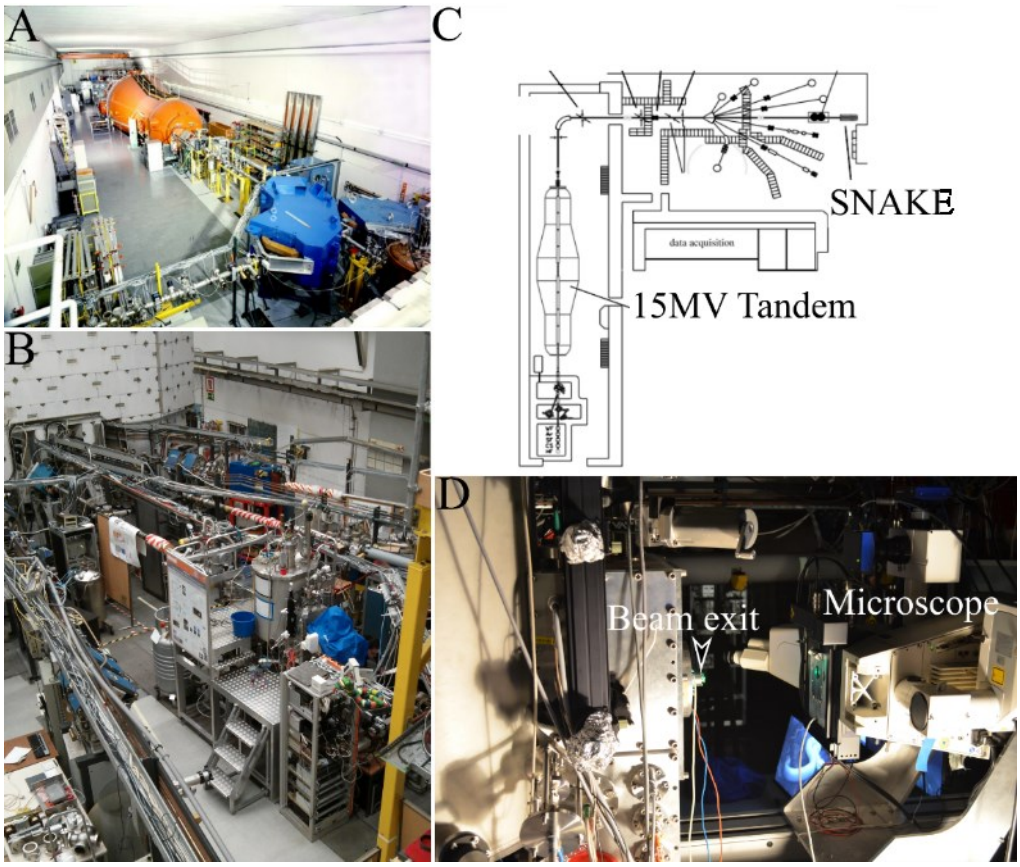

Fig.4 Overview of the SNAKE facility at the MLL in Garching. The 15MV tandem van de graaf accelerator (A) supplies SNAKE (B) with ions. The overview of the beamlines (C) adapted from Gerd Datzmann et al.(Datzmann et al., 2001). The microbeam exit window and the microscope for biological imaging are shown in (D) [Image credit: Image D, Christian Siebenwirth]

3.4.1 Setup for biological experiments

The beamline at SNAKE is capable of depositing a counted number of charged particles to a sub-micron (<1µm) beamspot. The experiments performed in this work make use of 55 MeV carbon ions with a Linear Energy Transfer (LET) of 350 keV/µm (at the cells) however SNAKE is capable of accelerating a large range of ions from protons to uranium. Carbon ions were chosen as single ion detection was possible using the imaging system. Being able to apply single, counted, ions to cells in a defined manner requires some complex technical solutions which have been developed over the years. The single ion detection method used at SNAKE makes use of a custom built live cell imaging container (Fig.5) which is fitted with an EJ-228 scintillator (Scionix, the Netherlands). The scintillator emits light in the UV range (390nm peak) when hit by an ion, which can partially be detected by the microscope's CCD camera. Imaging of the beam enables a calibration of the beam location based upon the detection of the signal emitted from the scintillator. The cells to be irradiated are plated on this scintillator coated with CellTak (Corning) which enables cells to grow on this surface and can then be targeted with the beam. The carbon ions, after leaving the beam exit window traverse the cells and are stopped in the scintillator where they produce a burst of light which is

detected and fed back to the irradiation system to verify the number of ions deposited. This system enables targeted deposition of counted ions at a known position. In the last few years the system and the software has been developed by Christian Siebenwirth (Siebenwirth et al., 2015).

The ability to target ions in this form enables a wide variety of possible ways to target cells and subcellular structures within them. Irradiation point matrices made up of any number of points, such as 6x6, can be created and loaded into the software. This custom creation of irradiation points enables a highly versatile irradiation pattern production. This flexible irradiation point system allows for the targeted irradiation of many cellular structures with any number of points using any geometry. Further automation can be integrated into the targeting system by using a thresholding macro which can analyse a micrograph and overlay irradiation targets over an automatically detected area of high signal. These features make the SNAKE microbeam an ideal candidate for answering complex biological questions regarding the irradiation response of subcellular targets such as mitochondria. Further experiments involving probing the radio sensitivity of sub nuclear regions such as nucleoli (Drexler et al., 2015), experiments for DNA double strand break protein structure (Reindl et al., 2017) and assessments of the cellular response to varying LET have been conducted (Schmid et al., 2017).

3.4.2 Imaging of cells using fluorescence microscopy

Irradiation and imaging of samples at SNAKE is performed using a Zeiss Axiovert 200M with a 63x oil objective (LCI Plan-Neofluar 63x/1.3 Ph3 Imm Corr M27, Zeiss) and a Colibri v1 LED light source (Zeiss) in combination with filter cubes and has been described in depth before (Hable et al., 2009). Briefly, the epiflouresence microscope is tilted 90° and mounted on a motorized table so that the microscope can be moved back and forth from the beam exit window to enable sample loading and imaging (Fig.5). The microscope is further equipped with a heated automated stage so that the samples can be not only kept at 37°C during the whole experiments but can be moved around on the stage to enable the irradiation of different areas on the sample. The LED modules available for the Colibri enabled a precise and narrow excitation light source and when combined with the Zeiss filter cubes enabled an efficient live cell imaging illumination system enabling a wide variety of fluorescence dyes and genetically modified fluorescence probes to be used during the experimentation. For detection, the fluorescence microscope makes use of a Zeiss Mrm CCD camera to capture images, the system is limited to 3 frames per second with the current software setup. This epifluorescence setup is capable of imaging before and after irradiation as well as concurrently to irradiation at a rate of 3 frames per second. This enables not only time series and Z-stacks of cells before irradiation and after to compare the outcome of the irradiation but also moving images of the direct response of ionizing radiation to cells as the ions traverse the cell in question. Moving images were however irradiated in a different way than the before/after type as concurrent imaging and irradiation bypasses the ability to count the individual incoming particles and must rely instead on a stable count rate from the accelerator. Therefore moving images at 3 frames per second induced an error in the region of

20% of applied ion number as a fixed time was chosen to irradiate a given target volume and count rate stability fluctuation during the irradiation would lead to the error in ion application.

3.4.3 Live cell imaging container

The Live cell imaging container (LCI) as shown in Fig.5 is a stainless steel container in which the EJ-228 scintillator has been inserted. Generation 1 LCI (Fig5.A) was based on the original hinge design and was updated to a hingeless screw design which was implemented during this thesis. The generation 2 LCI (Fig5.B) did not make changes to the imaging or cell growth however it increased handling significantly. The required number of cells are plated directly onto the scintillator which has previously been coated with 3.5µg Celltak per cm² and are allowed to adhere for at least 4 hours but in most cases overnight before experiments. Any staining procedures performed on the cells can be performed within the LCI under the flow hood in sterile conditions and just before imaging. The dye and medium contained within up to 6ml can be incubated in the incubator for the required time so that the cells do not suffer temperature related stress during staining in the LCI. The foil in the folding lid which is a 3.5um polypropelyene foil which, in the closed form (A, right) is the barrier between the beam exit window and the cells. The system enables irradiation and imaging of cells without detrimental effects for up to 6 hours as the medium is buffered and the temperature is kept constant using the heated holder (37°C), evaporation is minimized as the system is closed.

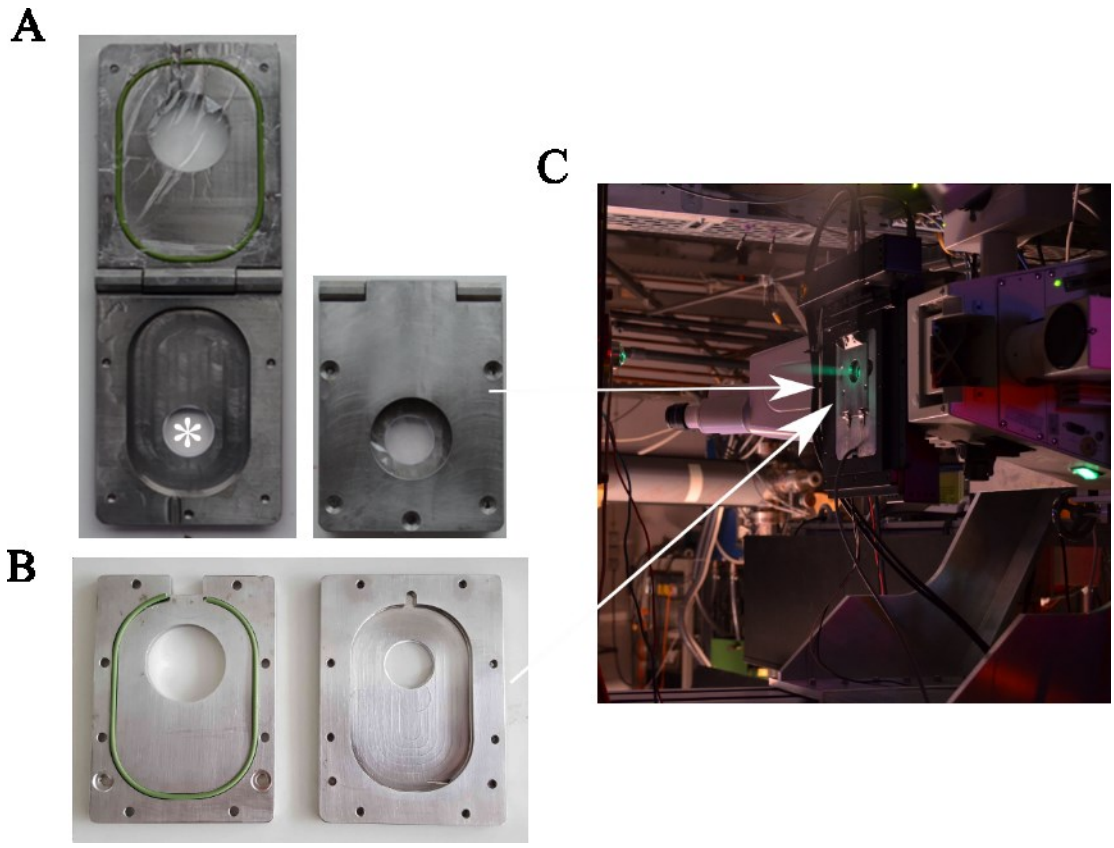

Fig.5: Live cell imaging container version 1 (A) in its closed and open form with an (*) showing the scintillator on which the cells can grow. The live cell imaging container version 2 without hinges used in the majority of experiments from 2015 onwards (B). An image of the LCI containers built into the microscope at SNAKE (B) the LCI contains up to 6ml of buffered media and is warmed to 37°C on the microscope stage making the setup ideal for longer term observations of up to a few hours.

3.4.4 Irradiation points

As mentioned in the introduction to SNAKE, the ability to set user-defined irradiation targets in the form of points or patterns is a great advantage that is available at SNAKE. The majority of the experiments performed at the SNAKE beam line for this body of work were performed using small matrices of irradiation points. Each point, represented by a white pixel was the target for the beamspot. The patterns most commonly used in this work were 4x4 and 6x6 irradiation point matrices (Fig.6) with distances of 0.489µm between points (Fig.6). Matrices were created using a text image with a defined number of pixels. The spacing between the individual irradiation points was then defined based on the known distance of a single pixel. The microscopy setup for live cell irradiation with the camera adapter and objective used defined a pixel size of 0.163µm per pixel. As the beamspot was <1µm in size, a 0.5µm spacing between points ensured overlap between irradiation points so that the area of interest could be totally and homogenously irradiated. Given the distance between the irradiation points (0.5µm) and the size of the beamspot (1µm) the irradiated fields were nearly homogenously covered by the beam ensuring all of the mitochondria under the target matrix were irradiated.

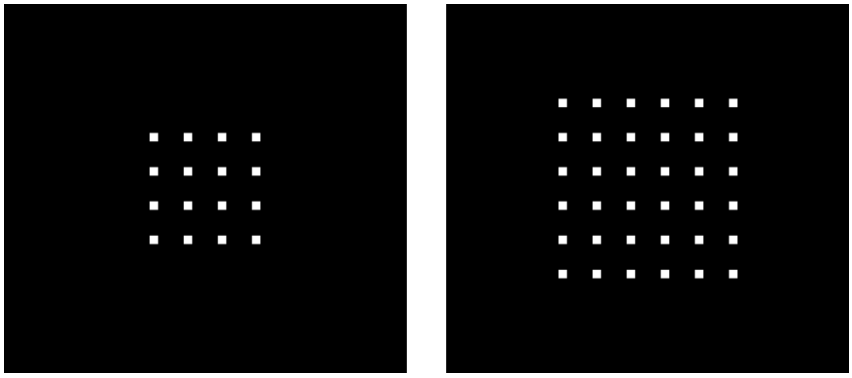

Fig.6 Overview of two irradiation point matrices; pixel size is 0.163µm (when using 63X objective with a 0.63X adapter) and each pixel is 0.489 µm apart. The matrices are user defined and can be made in any shape or form: the two depicted above (4x4, 6x6) are the most common ones applied.

3.5 AIFIRA

The Charged Particle microbeam AIFIRA (Applications Interdisciplinaires de Faisceaux d'Ions en Région Aquitaine) is an experimental microbeam setup at the Centre d'Etudes Nucléaires de Bordeaux-Gradignan (CENBG) in Bordeaux. The beamline is built up around a 3.5MV single end electrostatic accelerator (Fig.7). The microbeam used for biological experiments is collimated using platinum-irridium object apertures 5µm in diameter, as commonly found in electron microscopes. Following this initial aperture comes a second aperture in front of the magnetic lens which is adjustable between 20-200µm depending on the beam flux required. The beam is then further focussed by a triplet of magnetic quadropoles similar to those used in SNAKE however in this case not cooled by liquid helium. The beam then passes from the third magnet through the electrostatic deflection plates used to scan the beam over the sample to the target. The beam size in air is estimated by Monte-Carlo simulations and measurements to be 2µm (Bourret et al., 2014). The beamline as featured above is the same as the "nanobeamline" at CENBG, with only one triplet of magnetic lenses (Barberet et al., 2011)

Fig.7: The 3.5MV single end accelerator used at AIFIRA in Bordeaux (A) along with the beamlines of which the 0° beamline leads to the AIFIRA microbeam setup (B).

3.5.1 Setup for biological experiments

The setup with which it is possible to producs a beamspot of 2µm is used to focus 3 MeV protons with an LET of 11 KeV/µm. The irradiation method used is different as compared to SNAKE. At AIFIRA, particles are counted with a dummy sample holder which includes a 500µm thick scintillator (EJ-204, Scionix, NL) instead of foil (Fig.8). The protons are stopped inside the scintillator and the flash of light created is detected by a photomultiplier tube (PMT) detector (Hamamatsu) placed behind the dummy sample holder. The beam flux (particles/second) is inferred from the flashes of light detected after proton traversal of the scintillator by the PMT. From the value (counts/sec) measured more than 100 repeat measurements are taken and a mean and SD are calculated for the repeats to form a mean number of ions (N). The statistical fluctuation is ~ $\sqrt{N}$ then it can be assumed that a stable countrate has been measured. Based upon this, the number of ions required can be calculated as an aperture opening time and this time is applied to the beam aperture to achieve the deposition of the required number of ions. In case of pure statistics the uncertainty of the applied

protons is defined by the Poisson distribution ($\sqrt{N}$). Thus the relative error is smaller then 10% for high N (>100 number of ions) however increases for low ion number applications. The uncertainty $\Delta N = \sqrt{N}$ on short timescales (minutes) but the mean countrate fluctuates on a longer time scale (>30 mins). Therefore between every 1-2 samples the countrate is checked applying the method above to verify how stable the beam output is. This second component has been estimated by the group in Bordeaux to be in the range of 5%.

3.5.2 Cell container and seeding

Live cell imaging at AIFIRA was performed in stainless steel live cell imaging containers designed specifically for use at AIFIRA (Fig.8). The cells are grown on a polycarbonate disc covered with polypropylene foil of 4µm thickness with a working area of 8mm in diameter. The polypropylene foil was treated with Corning CellTak (Sigma Aldrich) to ensure adhesion of cells to the foil as samples are irradiated vertically. The cells were plated onto the polypropylene foil overnight by depositing a 500µl droplet of cell suspension containing 40 000 - 60 000 cells onto the foil. After one hour at 37°C and 5% CO_2, initial cell adhesion was sufficient so that another 500µl of medium could carefully be added to cells to stop the cells from drying out overnight. After overnight incubation, the medium was replaced with fresh imaging medium containing 25mM HEPES buffer and a round coverslip was placed over the disc to seal the cells in. This disc and coverslip were then placed into the holder and fixed in place by a stainless steel plate and a lock ring. The sealed imaging container was then transported to the beamline in a pre-warmed container and placed in front of the beam exit window in the microscope box (Fig.9) which was pre-warmed to 37°C.

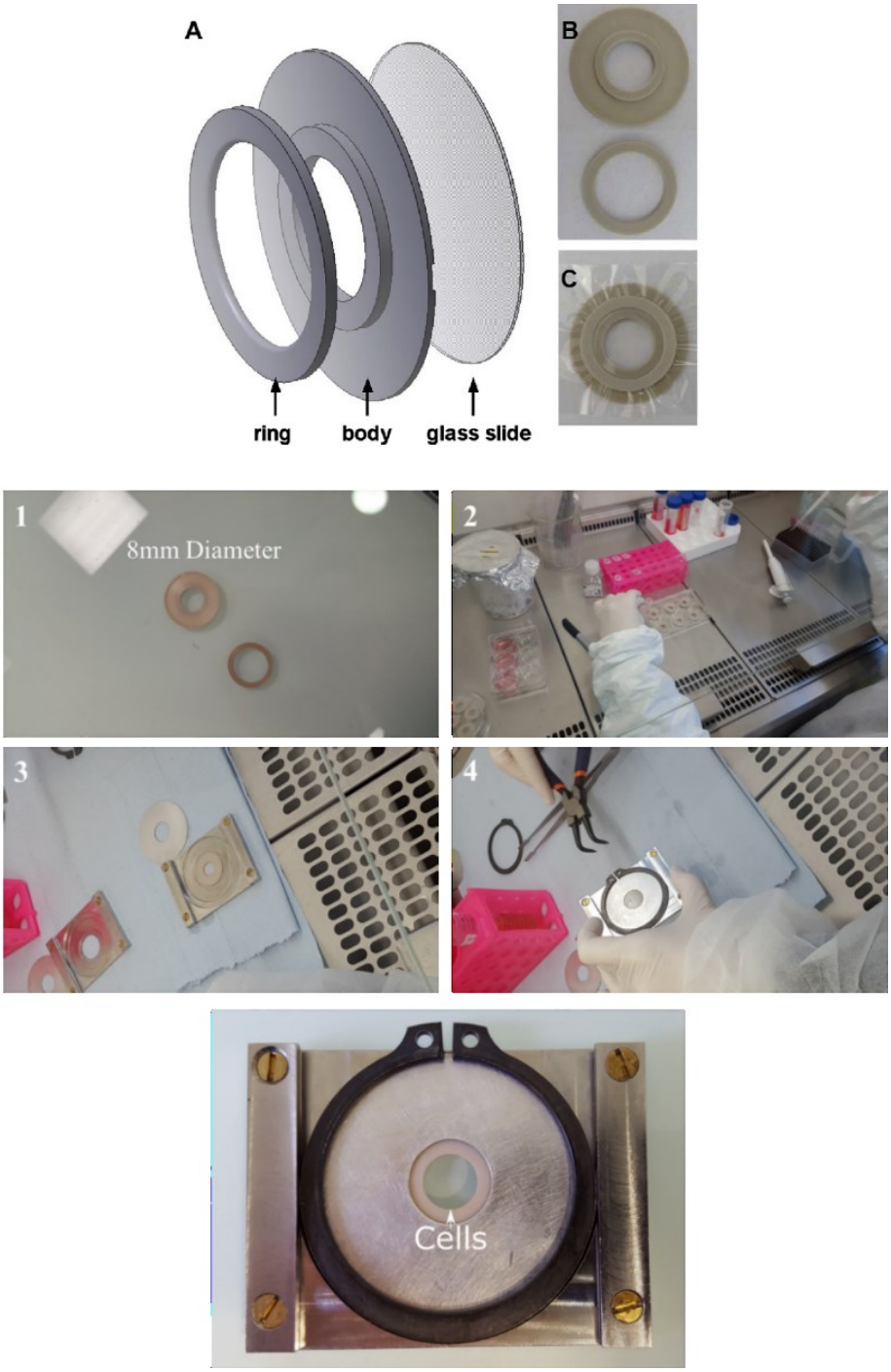

Fig.8 Overview of the imaging container used in irradiation experiments at AIFIRA (A,B,C) and the seeding and preparation for insertion into the beamline (1-4). The polyurethane ring holds a 4µm thick polypropelene foil (1) on which the cells are seeded overnight (2). The disc with the cells is then placed on a glass coverslip and into the holder (3) which is then fixed into place via the lock ring (4). The sample is then ready for irradiation and can be transferred to the beam for irradiation. Fig.A, B, C adapted from Bourret et al. (Bourret et al., 2014).

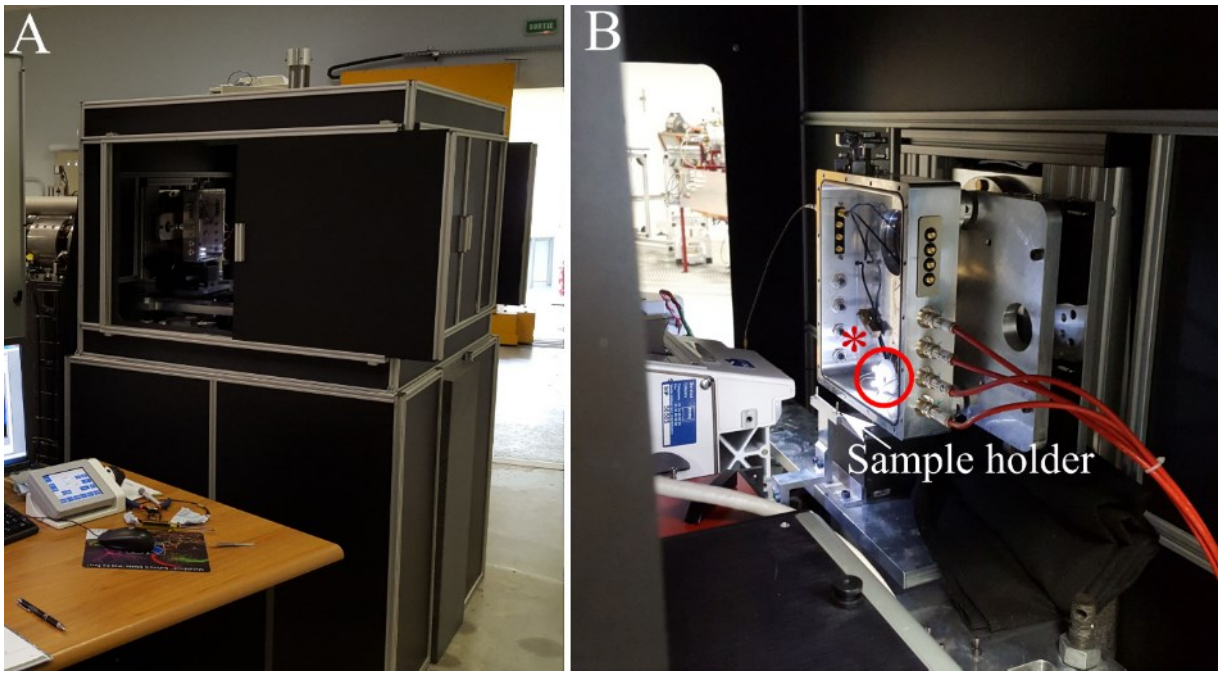

Fig.9: Live cell imaging microscope and enclosure used at AIFIRA. The imaging system is at the end of the beamline and is encased by a black box (A) to ensure minimal disturbance of the system. The box can be heated for longer imaging times and the microscope can be moved closer to the beam exit window and the sample holder (B) which has its own external phase contrast light source.

The live cell imaging setup at AIFIRA as depicted in Fig.10 is based around a Zeiss AxioObserver Z1 epifluoresence microscope and axiovision software package and enables live cell imaging of cells before, during and after irradiation at AIFIRA. The irradiation and target acquisition is performed by a piece of custom software, so both imaging and irradiation can be controlled separately or in sync by the software. The system uses the Zeiss Colibri LED system which enables a precise tuning of LED intensity for every desired excitation wavelength required and in combination with filter cubes enables a wide variety of imaging options. The fluorescence light emitted from the sample is detected by an Axiocam CCD Mrm Rev 3 as 8bit Tiff images. LED units and filter cubes were compatible between the two systems so the same LED units (555nm, 400nm, 480nm) were used for excitation of the samples and the same filter cubes were used as at SNAKE.

The imaging at the AIFIRA setup was however different in many ways from the imaging at SNAKE due to differences in hardware setup. As far as possible the parameters which could be kept the same between SNAKE and AIFIRA were maintained. Differences in the two imaging setups were mainly based on the difference in microscope setup and imaging containers. Imaging magnification was limited to a 40x long distance objective LD Plan-Neofluar, NA 0.75 at AIFIRA as imaging with a 63x and oil objective was not possible in this setup. Although the same Colibri LED light source was used in both cases, the microscope at AIFIRA was fitted with a Fluorescence Recovery After Photobleaching (FRAP) laser system which required a dichroic mirror (beam splitter) to be inserted into the main beam path of the microscope. The presence of this beam splitter leads to a partial absorption of the excitation light. The 2-3% LED settings

which were established at SNAKE had to be optimized for the light absorbed by the beamsplitter and the different objective. LED intensities of 20-25% were tested and showed little to no phototoxicity and similar intensities as with 2-3% at SNAKE and were therefore used in the experiments at AIFIRA.

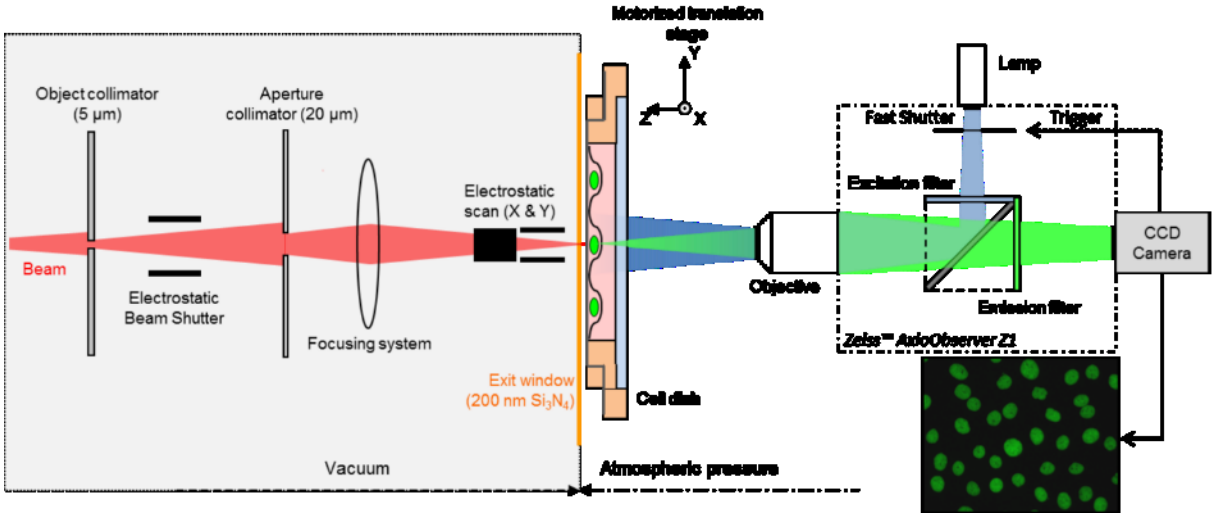

Fig.10: Overview of the irradiation and imaging setup used at AIFIRA: The beam enters the setup from the left and is collimated by two collimators after which it is focused using a magnetic focusing element. From Bourret et al (Bourret et al., 2014).

The less complicated sample installation setup at AIFIRA also provided definite benefits over that at SNAKE. The time from inserting the live cell imaging container to first images was substantially shorter which enabled a quick sample replacement if the staining was not ideal or any other problems were detected. This also meant that the number of different kinds of experiments performed could be maximised as sample swapping took 5 minutes in comparison to nearly 30 mins at SNAKE. The drawback was that there is no way to count single particles traversing the sample at AIFIRA so the number of applied particles comes with a larger error than at SNAKE.

3.5.3 Ion conversion between SNAKE and AIFIRA

To perform experiments initially performed at SNAKE with carbon ions at AIFIRA a conversion process was necessary. Since both experimental setups use high LET particles it was decided that the total deposited energy per unit area would be used as a unifying calibration aid factor. The protons used for irradiation at AIFIRA had an LET of ~10 keV/µm and the carbon ions at SNAKE 350 keV/µm. Given the difference in LET and the differences in beam size (1 µm vs 2µm), we calculated that per carbon ion applied at SNAKE, 35 ions would need to be applied at AIFIRA. To account for the difference in beam spot size, one AIFIRA beamspot was used in place of four SNAKE beamspots therefore each beamspot at AIFRA was targeted with four times the number of protons to make up for the difference in beamsize.

At AIFIRA 3.5MeV Protons with an LET ~10 KeV/µm were targeted to a beamspot of 2µm. To calculate the number of protons needed to deposit the same amount of energy per µm² a conversion based upon beamspot size and LET was performed and a conversion table was created. The energy was defined using a 4x4 irradiation point matrix at SNAKE. Taking only the LET values of both particles would indicate that 35 protons were needed for each carbon ion applied. When normalizing the energy applied per unit area, the beamspot size must be taken into account as the beamspot is 2µm at AIFIRA and the current 4x4 matrix was set at 0.5µm between each irradiation point thus four SNAKE irradiation points would fit into a single AIFIRA point to apply the same energy to the same area. So the number of protons needed was multiplied by 35 to ensure the same energy and then by four to ensure the correct total energy per unit area was applied. Therefore one beamspot of 100 carbon ions was equal to a single beamspot in Bordeaux with 14000 protons.

SNAKE	AIFIRA	
Carbon/point	equiv. Proton/point	equiv. Energy per area
200	7000	28000
100	3500	14000
90	3150	12600
80	2800	11200
70	2450	9800
60	2100	8400
50	1750	7000
40	1400	5600
30	1050	4200
20	700	2800
10	350	1400

Table 1 The conversion table used for application of ions at AIFIRA compared to SNAKE. The calculation is based upon the number of carbon ions and their energy at SNAKE presuming an LET of 350 kev/µm at the cells. The LET of the protons at AIFIRA was approximated to be 10 kev/µm.

4 Offline imaging: Pre-experiments

All dyes and experimental setups needed to be optimized and tested before being experimented on at the beamlines SNAKE and AIFIRA. Due to the limited availability of the microscope at SNAKE, many of the experiments were tested using the Leica SP8 laser scanning confocal microscope at the Universität der Bundeswehr München (Fig.11). The microscope is equipped with a heated and CO_2 aerated chamber which can be used for live cell imaging experiments. The majority of the dyes used were tested on this setup before being adapted for live cell imaging experiments at SNAKE. Cells were seeded in 35mm round glass bottom IBIDI imaging chambers and stained with TMRE, DAPI, PI, MTG and all other dyes before being tested with control chemicals to elicit positive responses.

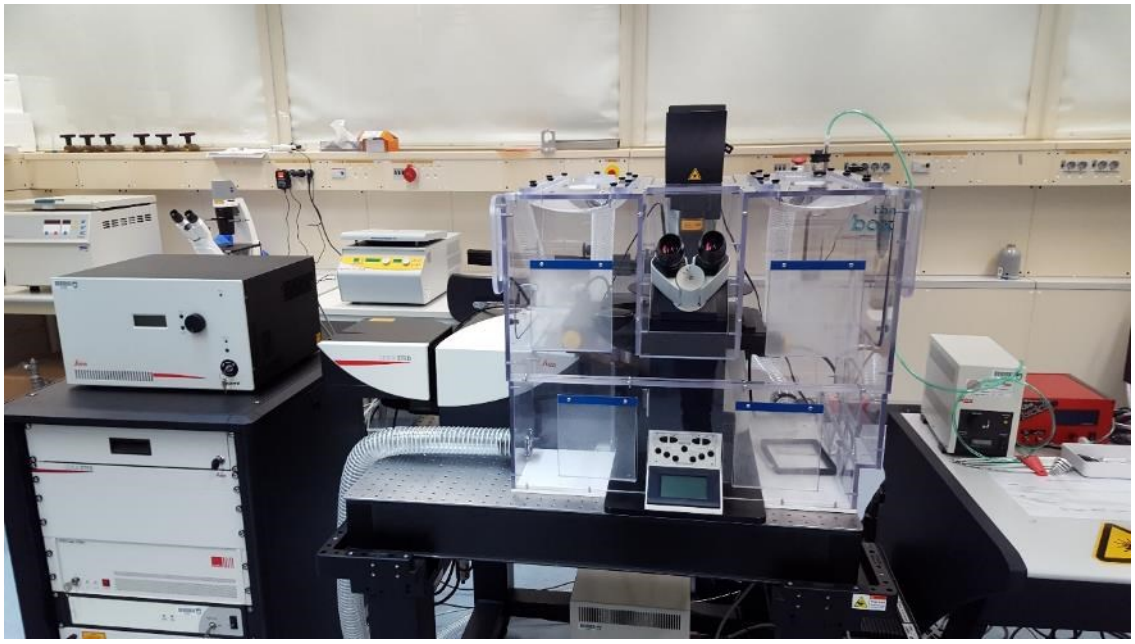

Fig.11 Leica SP8 STED unit at the Universität der Bundeswehr München. The microscope and the incubation chamber were used for pre-experiments to verify the staining patterns of dyes used in experiments at SNAKE and AIFIRA

5 Methods

5.1 Cell culture

Three different types of cells were used for the experiments in this thesis: MCF7 breast cancer cell line (American Type Culture Collection, ATCC, HTB22); A549 adenocarcinoma cell line (ATCC, CCL-185); a non-cancerous cell line EA.HY 926 umbilical cord endothelial cells (ATCC, CRL-2922). All cell lines were cultured in DMEM high (D6429, Sigma Aldrich) supplemented with 10% FCS (Sigma Aldrich) and 100mg/ml Penicillin Streptomycin (Sigma Alrich). The cell lines were initially chosen for their large number of mitochondria per cell and ease of cultivation of cell lines. The genetically encoded roGFP2 U2OS cells used for experiments in Bordeaux were cultivated in Mccoys Medium (Dutscher). Initial tests were also performed with other cell lines including human lymphocytes and HepG2 cells. Irradiation experiments with these cells were not performed as their cultivation procedures were not as reproducible as for the three cell types given above. Having reproducible cell growth and monolayer formation is essential for experiments at SNAKE and AIFIRA as cells which do not adhere well or form multiple cell-layers do not allow for reproducible results.

5.2 Analysis of mitochondrial traits

The experiments performed in this thesis were all based around live cell imaging of fluorescent dyes or GFP probes using microscopy. The details of each individual probe and their function will be explained in section 6 before each set of experimental results. The staining procedures for each probe are detailed below.

5.2.1 Mitochondrial membrane potential

Mitochondrial membrane potential was analysed using TMRE (Enzo lifesciences) at concentrations of 250nM or 500nM diluted in full culture media (DMEM High). The staining procedure was established by incubating cells with TMRE containing medium at 37°C, 5% CO2 for 30 minutes before washing and imaging. TMRE is cationic dye which accumulates in polarized mitochondria in direct relation to the charge present in the polarized mitochondria. The stain enables visualization of active mitochondria as well as sudden changes in membrane potential.

5.2.2 Mitochondrial membrane integrity

Mitochondrial membrane integrity was analysed using MitoTracker Green (Thermo Fischer) at a concentration of 200nM in full culture medium (DMEM High). Mitotracker green staining was performed by incubating cells in MTG containing media at 37°C, 5% CO2 for 30 minutes before washing twice and imaging. MitoTracker green binds to the OMM and therefore represent the membrane integrity of the outer membrane. Any changes in the membrane would lead to a change in signal distribution of MitoTracker green which can be analysed.

5.2.3 Mitochondrial superoxide production

Mitochondrial Superoxide Production was analysed using MitoSOX (Thermo Fischer) at a concentration of 1µM in full culture medium. MitoSOX staining was performed by incubating cells in MitoSOX containing media at 37°C, 5% CO2 for 20 minutes before washing and imaging. MitoSOX is a dihydroethidium derivative with a TPP+ (Tetraphenylphosphonium) targeting sequence enabling the uptake into polarized mitochondria. Upon interaction with superoxide MitoSOX fluorescence intensity increases up to 10 fold indicating an interaction with superoxide.

5.2.4 Mitochondrial ROS production

Mitochondrial ROS generation as measured by Glutathione redox potential Probe mito-roGFP2 was performed using a cell line generated for us in collaboration with the AIFIRA group in Bordeaux. The U2OS Cells were transfected with the roGFP2 using Viromer Red (LipoCalyx) and selected until a stable cell line was generated. These cells could then be imaged and irradiated in experiments at AIFIRA. The roGFP protein undergoes a conformational change when it becomes oxidized which leads to a shift in excitation wavelength which can be measured by dual excitation ratiometric imaging.

5.2.5 Plasma membrane integrity

Plasma membrane integrity after irradiation was analayzed using Propidium iodide (PI) in full medium. The cells were incubated with TMRE as explained in 5.2.1 and then washed, medium containing 1µM PI was then added to the cells before imaging and stayed on the cells throughout the imaging process. PI will not enter cells with intact plasma membranes, however if the plasma membrane becomes porous PI will enter the cell. PI enters into cells with membrane damage and intercalates with the nuclear DNA to produce a highly specific nuclear fluorescence staining. Cells which have undergone membrane damage and are incubated in PI containing medium will show a nuclear staining to indicate plasma membrane damage.

5.3 Analysis of microscopic images

Images taken on the Zeiss (Axiovert 200M, Z1) and Leica (SP8) microscopes during the work in this thesis are opened in FIJI (Fiji Is Just ImageJ) an imaging software package for microscopic analysis adapted from ImageJ (Schindelin et al., 2012). The images are then subjected to various analysis methods as detailed in the individual experiments of chapter 6.

6 Experimental results and analysis

6.1 Mitochondrial membrane potential: TMRE Imaging

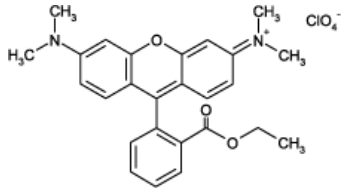

Tetrmethyl rhodamine ethyl ester (TMRE)

Tetramethyl Rhodamine ethyl ester (TMRE) is a cationic fluorophore of Molecular Weight (MW): 515 with a peak excitation wavelength of 549nm and an emission peak at 574nm (Fig.13). TMRE was chosen as it is a well-documented method to assess mitochondrial activity and function by looking at mitochondrial membrane polarization state. A variety of such cationic markers exist however two in particular exhibit the ability to show fast changes in polarization state, TMRE and TMRM. TMRE's cationic nature allows the fluorophore not only to permeate the plasma membrane but also the mitochondrial membrane readily and does not aggregate or bind to membranes (Perry et al., 2011).

The accumulation of TMRE within a cell allows for an assessment of membrane potential as TMRE abundance in the cell is relative to the charge (-ve) present in any given intracellular space, cytoplasm or mitochondria. The charge on the dye molecule (+1) is therefore used as a targeting mechanism as all intracellular spaces are negatively charged compared to the extracellular space (Fig.12).

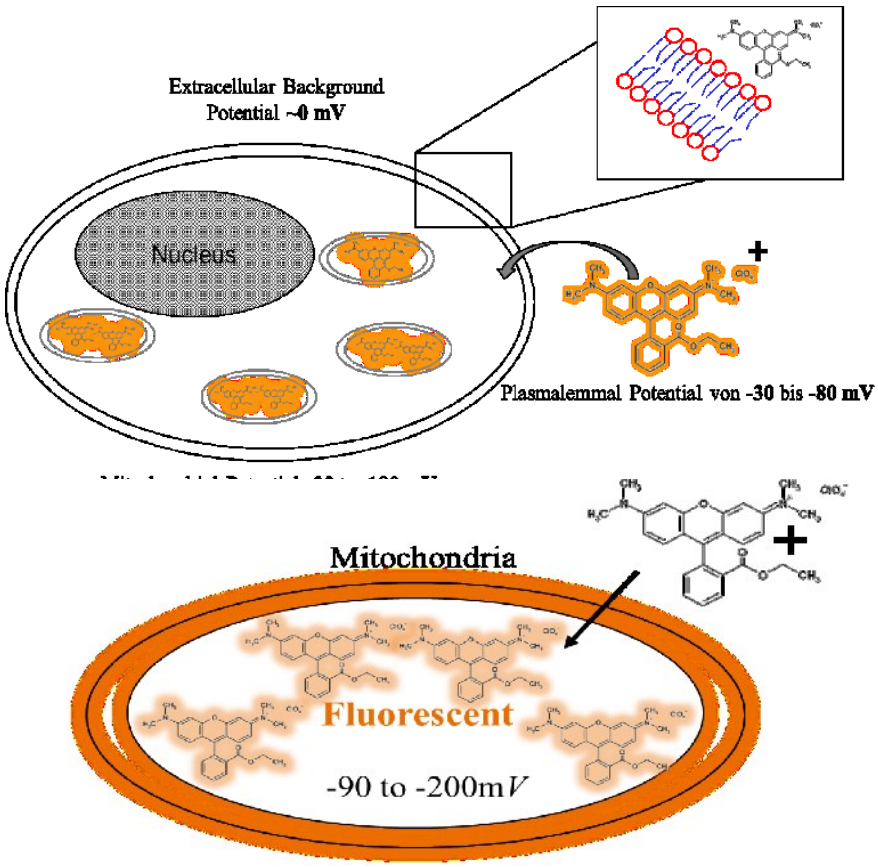

Figure.12: Representation of the uptake of TMRE by the cell and the mitochondria. The upper section shows the fluorescent, positively charged TMRE entering the cell by freely diffusing through the plasma membrane (upper right box) towards the relatively negative space of the cytoplasm and on into the mitochondria. The lower section shows the accumulation of the TMRE within the mitochondria and the overall increase in mitochondria specific fluorescence along with the relative membrane potential of the mitochondria.

The ability of TMRE to pass through cellular membranes allows for TMRE to quickly spread throughout the sample and into the mitochondria in concentrations high enough that the mitochondria exhibit a point like fluorescence when imaged (Fig.13). The concentrations used for live cell imaging (250-500nM) enable bright and stable mitochondrial signal due to the accumulation of TMRE in the mitochondria. To achieve such stable mitochondrial staining, the dye must be loaded until it reaches equilibrium to ensure no more TMRE is flowing into oppositely charged regions of the cell and therefore changing the signal during imaging. To ensure good signal-to-noise ratio (S:N), washing steps are vital as they help to remove the excess background signal created by TMRE present in the media. Loading of the TMRE into the cells requires a dilution from the 12mM stock to the working concentration of 250-500nM, a concentration ideal for the imaging system and the cells, the dye is then allowed to equilibrate in the growth medium for 20-50 min at 37°C in the dark (time was variable depending on cell type). After staining polarized mitochondria with TMRE, the signal was readily observable with our fluorescence microscope at SNAKE (Filter: 43HE Zeiss) and can be imaged in cells in real time. The fluorescence micrographs obtained from cells loaded with TMRE depict mitochondria with intact membrane potential (Ψ_m). Mitochondria which are unable to maintain their membrane potential would not be able to develop the charge difference needed to accumulate TMRE.

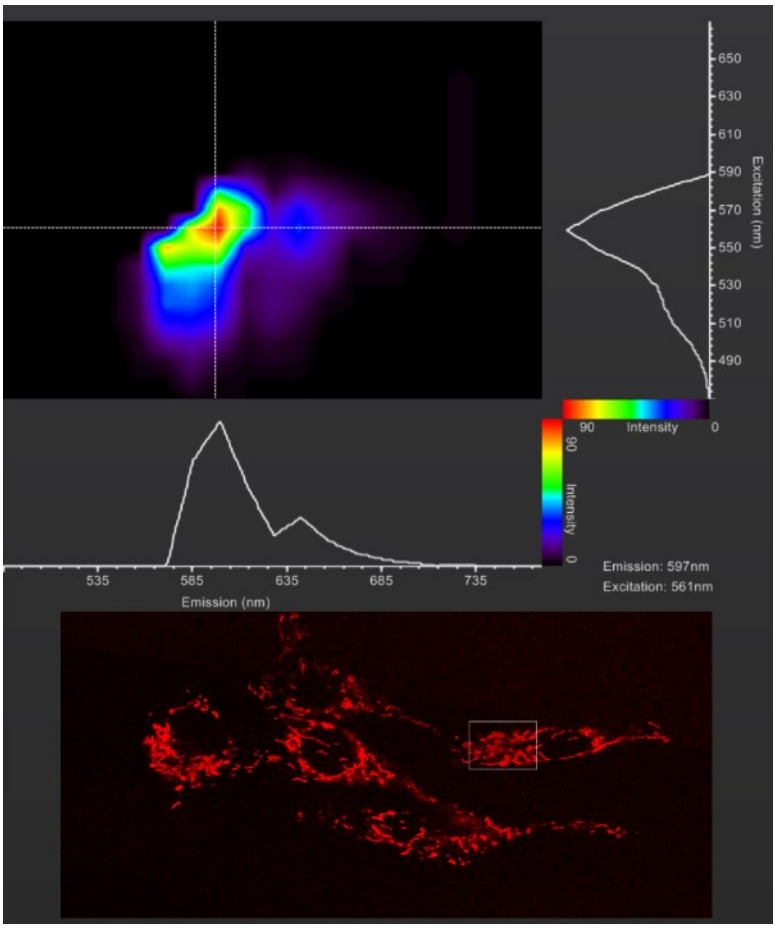

Figure.13: Excitation emission wavelength scan performed on MCF7 cells using the Leica SP8 scanning confocal microscope. The figure depicts the stained cells (lower) and the chosen Region of Interest (ROI) for the wavelength scan (Box) along with the measured excitation/emission peaks (upper). The Leica SP8 scanned all emission wavelengths for every block of excitation wavelengths. The wavelength block size for detection and excitation was 10nm.

6.2.2 Photoactivation of TMRE

Photo activation of TMRE stained mitochondria manifested itself as a light induced loss of mitochondria specific TMRE signal in response to overexposure to the Zeiss Colibri 555nm LED emitting the excitation light (Fig.14). Photo activation was one of the major limitations to the acquisition parameters in early experiments, as taking a large number of short exposure images for more than a minute would yield a total or partial depolarization of the whole area observed. Initial experiments, where mitochondria were irradiated, showed false positive depolarization of mitochondria after irradiation due to the photo activation effect induced by 100% LED intensity (Fig.15). A set of timelapse images is shown in Fig.15 illustrate the photoactivation effect. The upper panel shows that even 25 cycles of 700ms of 100% LED exposure was enough to depolarize the majority of the cells in the field of view and cause redistribution of TMRE from the mitochondria to the cytoplasm and the extracellular space. In order to rule out the effect of light induced depolarization in the irradiation experiments, images were consequently acquired at lower LED intensity and less frequently.

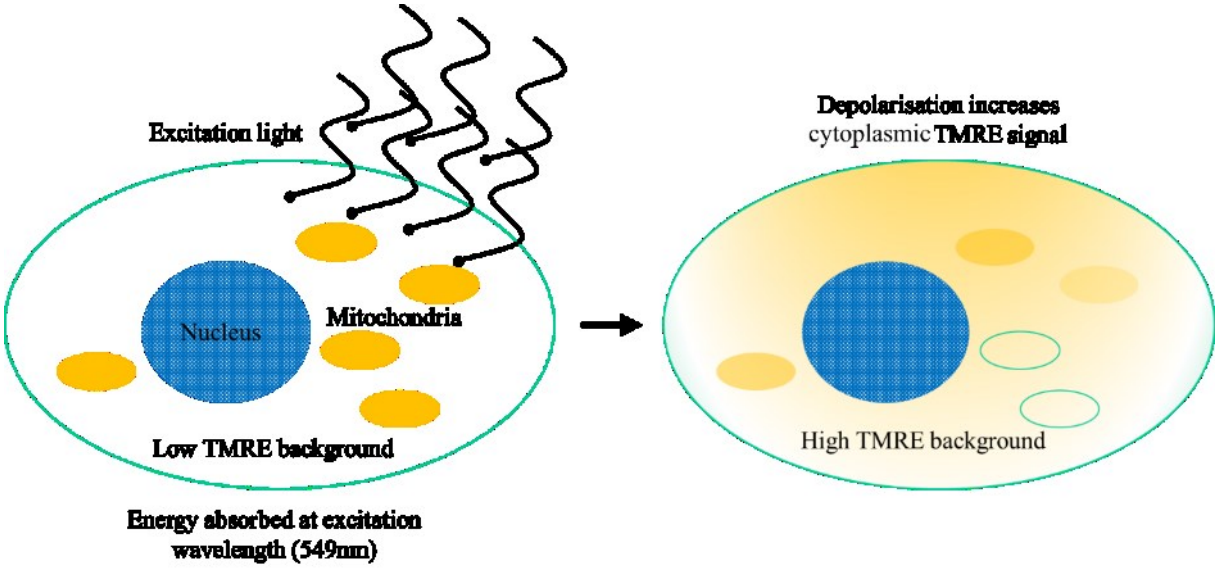

Figue.14: A representation of light induced depolarization and relocalization of TMRE. Exposing TMRE to long periods (minutes) of high intensity LED excitation light induces mitochondrial depolarization. The depolarization leads to a relocalization of the TMRE dye from the mitochondria to the cytoplasm which causes an increased cytoplasmic background.

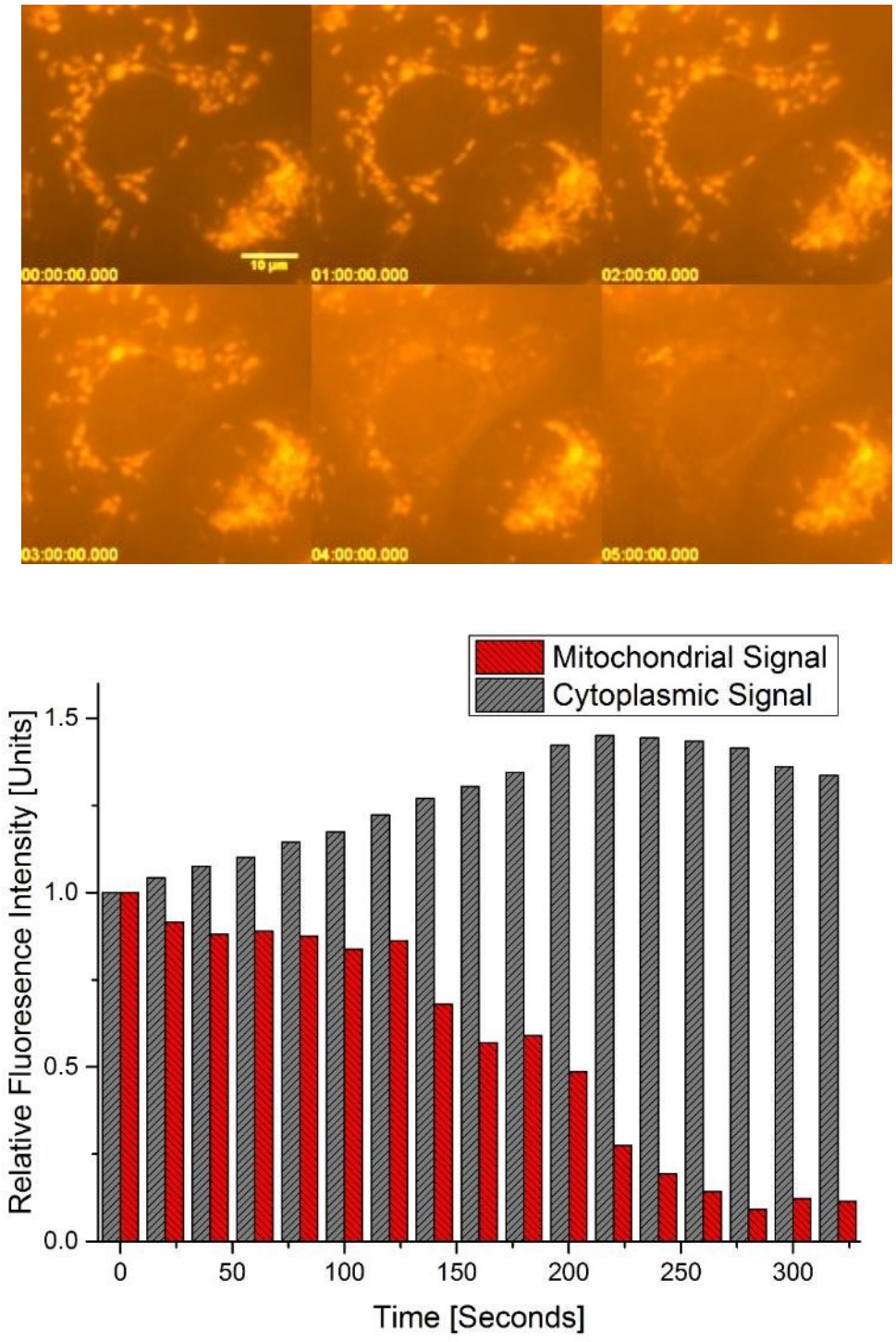

Figure.15 Micrographs and quantification of micrographs depicting phototoxic depolarization. Micrographs of MCF7 cells attained with 500nM TMRE in an unwashed state were taken every 20 seconds for 5 minutes using 100% 555nm excitation light. The micrographs (upper panel) show the light induced depolarization of mitochondria and relocalization of TMRE. The quantification (lower panel) shows the relation of mitochondrial signal vs the cytoplasmic signal (as measured over the nucleus). The graph shows a rise in cytoplasmic signal as the mitochondria specific signal decreases.

To separate out the radiation induced depolarization events from the light induced depolarization, experiments were performed on the beam line under the same microscopic conditions so as to best match the experimental conditions but without targeted irradiation. Light induced depolarization is however not a new phenomenon in the area of mitochondrial biology and has been experimentally examined in the literature (Perry et al., 2011). According to work by Distelmaier et al., the continuous illumination of membrane potential dyes such as TMRE may trigger singlet oxygen ($^1O_2$) production which in turn can lead to damage of the mitochondria and depolarization (Distelmaier et al., 2008). Therefore, to enable fast sequential imaging of mitochondria after/during irradiation, the 555nm LED intensity was modulated down from the initial 25-30% to 2-3%. In combination with 500nM TMRE staining and using the defined illumination settings, enough light reached the cells for high quality noise-free image acquisition to enable acquisition every 500ms for up to 10 minutes without visible phototoxic damage. Further indication of light induced singlet oxygen production was seen in mitochondrial superoxide detection experiments performed using MitoSOX (See 3.6.1)

Live cell imaging of mitochondria stained with TMRE requires a delicate balance of exposure time, image frequency and LED intensity. As mitochondria are highly dynamic organelles it is important to image frequently enough that individual mitochondria can be tracked. On the other hand, it is important not to image too frequently and with too high intensity as this causes phototoxicity. These issues extend also to the staining procedures, as staining mitochondria for too short a time does not allow for the equilibrium of TMRE to be achieved in mitochondria. Washing of the sample after staining is equally as important as the other experimental variables for obtaining a good S:N. The method detailed in this section and the limitations and pitfalls documented were experimentally investigated and were considered during all of the experiments using TMRE to ensure a highly reproducible staining procedure.

6.2.3 Mitochondrial membrane potential visual analysis

The mitochondrial response to targeted deposition of ions was subjected to a simple visual analysis of the TMRE signal. When mitochondria undergo depolarization, the membrane potential cannot be maintained across the IMM leading to a loss of membrane potential ($\Delta\Psi_m$) present across the mitochondrial membrane. When polarized (charged) mitochondria are loaded with TMRE and begin to show fluorescence signal due to TMRE accumulation, it was hypothesized that damaging mitochondria with ionizing radiation could lead to a loss of the highly localized mitochondrial signal. This hypothesis was tested by highly localized mitochondrial irradiation using a spot application of carbon ions at SNAKE and protons at AIFIRA. Mitochondrial membrane potential is directly related to mitochondrial function and is therefore an ideal parameter for analyzing radiation effects on mitochondrial function. In order to probe mitochondrial membrane potential after irradiation, cells were first seeded into the LCI setup at SNAKE and stained with 500nM TMRE until the dye reached equilibrium. The sample was then placed into the microscope (Fig.5C) at the beamline for image acquisition and irradiation. The image acquisition followed the same pattern at both experimental setups, an initial image of an area of interest was taken. This initial micrograph was used as the template to choose an area of interest to target. Targets in the form of individual pixels (points) or matrices, for example a 6x6 point matrix were placed and then the sample was irradiated (Fig.16).This process of target selection initially required manual selection of ROI's (Regions Of Interest) on a template image and took some time as areas with very strong signal or mitochondrial overlap were not ideal for post irradiation analysis. With time and experience this process was sped up and target areas were selected in under 20s. The time between the "Before" image and the first "After Irradiation" image was therefore a combination of image acquisition times, target selection and irradiation and could take anywhere from 30s to 2minutes depending on the complexity of the field and the targets defined.

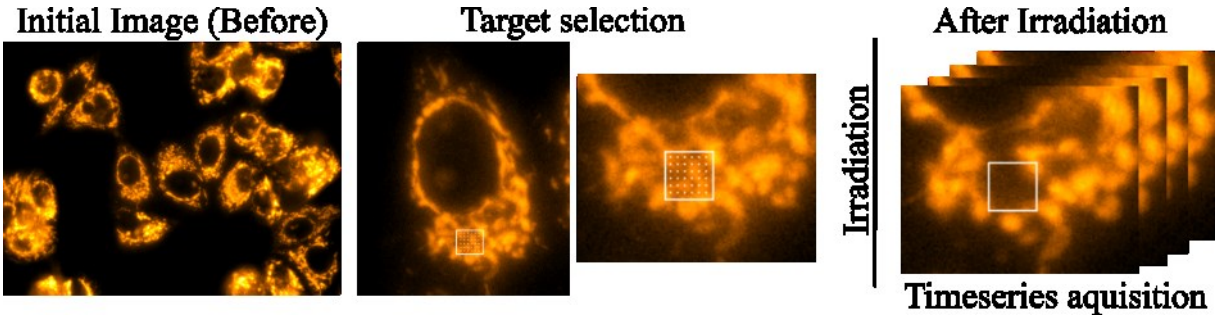

Fig.16: An overview of the steps in image acquisition common to both SNAKE and AIFIRA. Initial images are taken, target areas defined by the user (Left). The targets are then selected and irradiated (Centre) and the timeseries image acquisition is started automatically (Right).

The process for target selection and image acquisition was the same at both the SNAKE and AIFIRA facilities. Even though the software was different, in both cases the workflow followed the same steps as depicted in Fig.16. In later experiments, automatic matrices were overlayed over mitochondria using the macro "AutoTarget" to perform live imaging of the irradiation of individual mitochondria. The image acquisition was different in this case. As in the previous setup an initial image was used as a template for target selection, on this image all mitochondria in a region of interest were selected and the "AutoTarget" routine then determined mitochondrial regions. Inside this region a matrix was overlayed where the distance between points was user defined. The input parameters, matrix size and cell of interest were selected by hand and the "AutoTarget" procedure overlayed a matrix of irradiation points over the selected mitochondria in the cell of interest. Time series were then acquired, and the irradiation was started allowing imaging concurrently with irradiation (Fig.17). This setup enabled an unprecedented view of the response of mitochondria as they were being irradiated. The minimum time achievable between images with the current setup was limited to 300ms, predominantly set by excitation light, exposure time and the limitations of the imaging software. The resulting time series therefore enabled a more detailed look at the response of the mitochondria to irradiation in real time as compared to the before/after images (Fig.18) taken where there is a delay between the before image and the irradiated image.

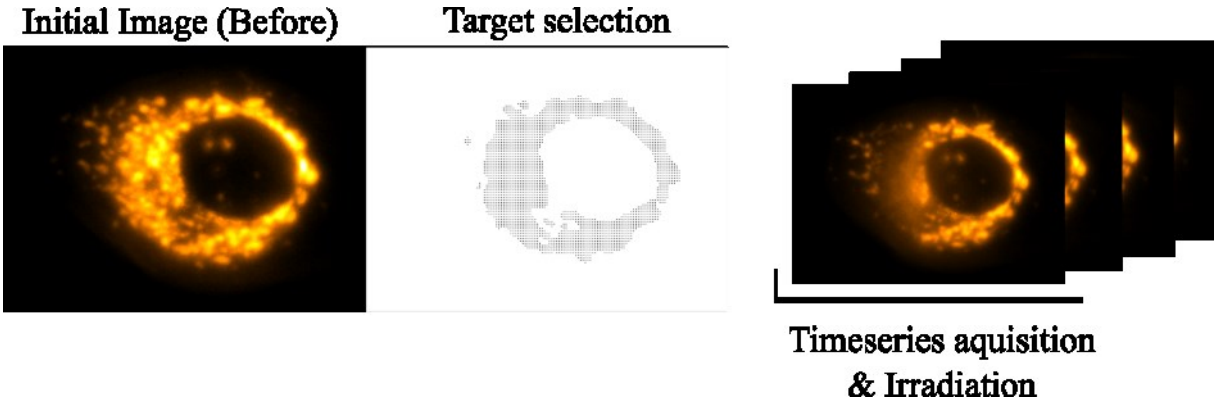

Fig.17: The figure depicts an overview of concurrent irradiation and imaging performed at SNAKE. The initial image is taken (Left), the macro defines the AutoTarget region (Centre) then the irradiation and imaging are started (Right) and continued until the desired number of ions have been applied.

Images acquired using both of these approaches could then be analyzed using the FIJI. In order to ensure the least amount of background noise, dark field images were taken to determine the background CCD noise and subtracted from the images before analysis. The image sequences taken in the before/after mode were then stitched together so that the "before" image with the targets and the time series of "after", or "during" in case of the live imaging/irradiation, could be handled as a single stack file in which all images are contained.

6.2.3.1 Experiments (SNAKE and AIFIRA)

The initial experiments were not optimized for excitation light intensity and the application of single ions was masked by the phototoxic effects discussed above (Fig.15). This lead to a brute force initial experiment whereby 56 irradiation points were manually inserted into the initial (before irradiation) image of the TMRE stained MCF7 cells. 100 carbon ions were then applied to each spot, a total of 5600 ions. The cells were imaged after completion of irradiation every 2 min for up to 10 min. After application of 5600 ions to 12 positions in a total of 9 cells, these initial experiments were concluded. The outcome of which showed that each targeted area in question showed total loss of mitochondrial TMRE signal intensity in only the targeted areas as shown by (Fig 18, upper) in which 2 of the 9 cells are shown as a representative samples. The images depict TMRE stained mitochondria before, before with targets overlayed and just after irradiation of all cells was completed, the estimated length of time between irradiation and the "after" image is in the range of 30s for this experiment. All 12 fields (56 points) were irradiated between image "before" and image "after", with a carbon ion count rate of ~2kHz. This carbon ion deposition would take ~30s so in this case image acquisition delay between initial images was due to the long irradiation time.

Analysis of signal intensity in the irradiated areas showed a drastic reduction in signal intensity in the targeted area (Fig.18). The reduction in signal was such that the intensity nearly reached intracellular background post irradiation. The loss of signal in the irradiated area was initially attributed to the depolarization of the targeted mitochondria but could be due to destruction of the TMRE molecules as the number of ions used was high. Further verification was required to ensure that the loss of signal seen was due to mitochondrial depolarization and not due to TMRE destruction.

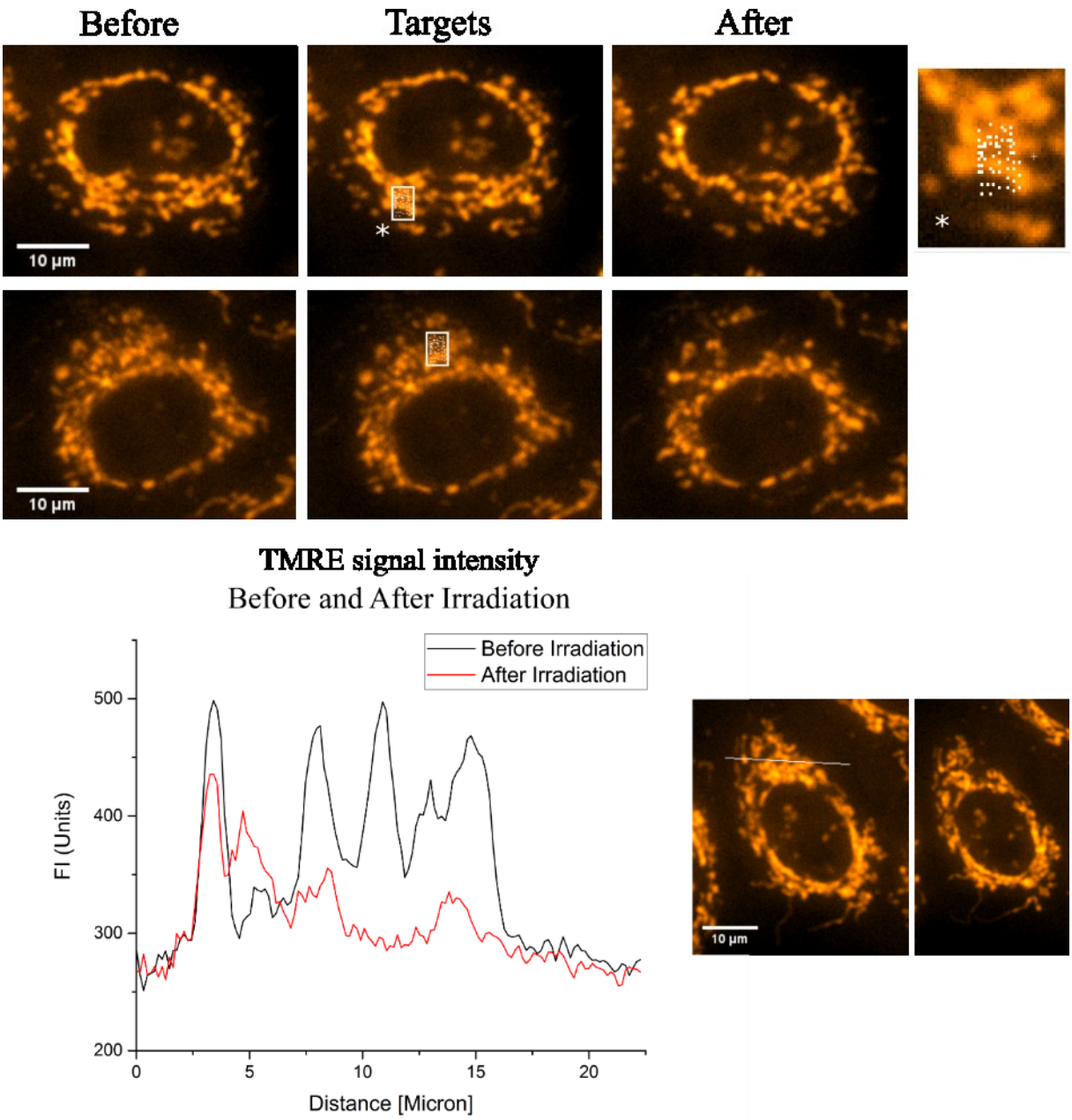

Figure.18: The figure shows the initial experiment performed at SNAKE. The upper two sets of micrographs each show one representative cell before irradiation, with targets, and after irradiation. The targets were placed manually by creating a 56 point target and applying this to an area of high TMRE stain, a close-up of the target area is shown in the sub-image (*). The lower graph and corresponding micrographs depict a cell irradiated with the same irradiation pattern (*) before and after irradiation.

The initial experimental results indicated that some direct mitochondrial response was visible after ionizing radiation, the origin and or mechanism of this response however was unknown. To further investigate this presumed biological loss of function seen in the initial experiment, a more comprehensive approach was taken to attempting to understand the phenomenon seen. The applied number of ions (5600) would need to be reduced and a less random irradiation point matrix would need to be constructed to further investigate the process suspected to be a membrane depolarization process.

Even after this initial experiment, there were some indications in the data that suggested that the depolarization was indeed a biological response and not just a physical destruction of the TMRE molecule as mitochondria outside of, but connected to mitochondria inside the irradiated field, also depolarized while other clearly non-connected mitochondria outside of the field showed no response. In order to visualize all depolarized mitochondria, the image “before irradiation” was divided by the resulting “after irradiation” image and was output as a 32bit float image which enabled integer pixel values to be displayed. Values <1 indicate an increase in signal intensity and values >1 indicate a net decrease in signal intensity as depicted in Fig.19. The resulting images show a group of mitochondria in a gray scale image where the white pixels indicate the area of signal loss. If the integer values are then further subdivided into a colour scale a heatmap of the affected area can be created showing the relative loss of signal.

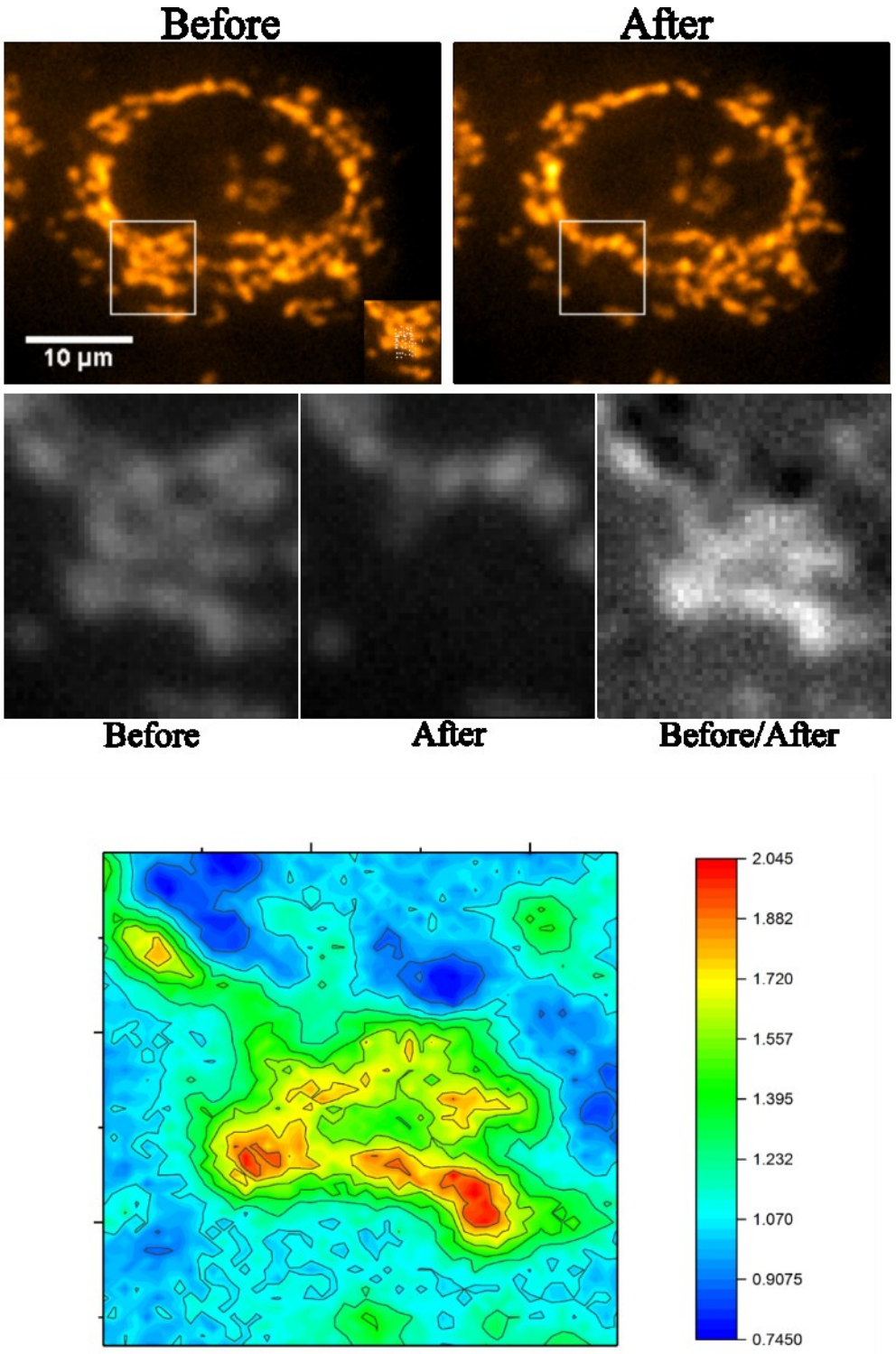

Figure.19:The Figure depicts an MCF7 cell stained with TMRE (orange) and the targeted area (box) along with the irradiation pattern before (left) and after(right) irradiation. Below is the irradiated area of interest before (left) after (centre) and as a quotient signal (before/after) (right). The heatmap is a pseudocolour representation of the relative change in signal intensity where red indicates a large loss of signal and blue indicates a relative gain in signal.

The heatmap shows that one distinct mitochondria at the top left of the map has also depolarized even though it was outside of the direct irradiation field. This loss of signal was an initial indication that the phenomenon of TMRE loss, which was hypothesized to be depolarization, was not just a highly localized destruction of TMRE but an actual loss of membrane potential within a connected network of mitochondria (Fig.20). In addition the mitochondria next to those in the targeted area gained in fluorescence intensity relative to those in the irradiation field which further strengthened the idea that TMRE was relocalized after targeted irradiation. More of these out-of-field depolarization events were observed throughout the experiments with TMRE. However, due to the lack of highly interconnected mitochondrial networks seen during the initial beam times at SNAKE with MCF7 cells no larger scale network depolarization was observed. It was not until further experiments at AIFIRA and SNAKE were performed that large scale network depolarization was observed for the first time.

Networks of interconnected mitochondria and their response to targeted ionizing radiation would play an important role in dispelling the idea of TMRE destruction. Experiments performed at the AIFIRA beamline in October 2015 were able to capture a whole interconnected network of mitochondria depolarizing after targeted irradiation with protons. A network of connected mitochondria depends on the overall intact polarization state for its function, so if one area of the network is damaged the rest of the connected organelle will be affected and consequently depolarize. An experiment was performed in Bordeaux where a single 6x6 irradiation point matrix was targeted to an area of highly interconnected mitochondria (Fig.20). The analysis of the targeted cell was performed in a similar way as with the heatmap. The initial “before” images were divided by the consequent images at each timepoint. The resulting 32bit float images were depicted as grayscale images so the white pixels (values >1) indicate a loss of mitochondrial signal in comparison to the gray (values ≤ 1).

The resulting depolarization extended throughout the network to areas more than 15µm away from the initial 6x6 irradiation field. The result reinforces the results (Fig.19) seen in initial experiments at SNAKE but on a larger scale. The mitochondrial TMRE signal outside of the irradiation field is lost; this is a further indication that TMRE is not destroyed by the irradiation but the mitochondrial charge is lost and therefore the charged dye leaves the mitochondria and dissipates into the cytoplasm.

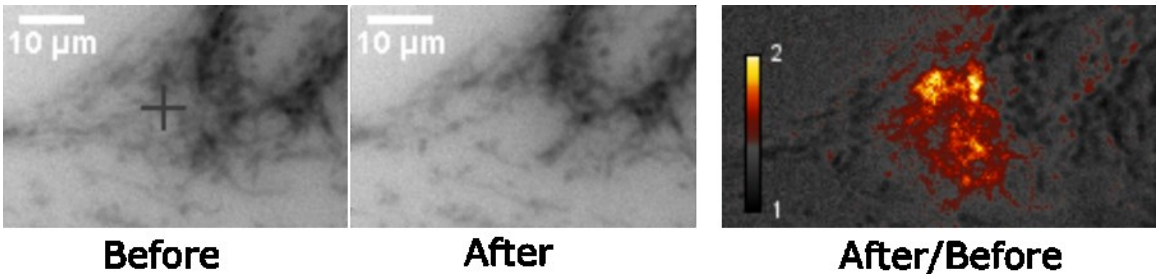

Fig.20: Images from a timelapse before and after irradiation. The image represented in pseudocolour (right) shows the quotient of the signal intensity (before/after). The mitochondria in the irradiated area are highly interconnected and all connected mitochondria, even those >15um away from the irradiated area, show a loss of signal (black to white). The cross in the before image shows the centre of the 6x6 irradiation matrix used to apply protons.

To ensure that the TMRE which is released from the depolarized mitochondria actually entered the cytoplasm, all mitochondria would have to be irradiated in a cell and the cytoplasmic background would have to be measured to verify an increase in signal in the background and a loss of highly localized signal. To perform such an irradiation the automatic targeting routine "AutoTarget" (described in previous section) was applied to MCF7 cells at SNAKE. All mitochondria within a user-defined area with a signal above a detectable threshold were overlayed with a defined point matrix. This enabled detection and consequent irradiation of all mitochondria in a defined area or a whole cell. This technique enabled a closer look at the depolarization effect as it occurred.

The network depolarization effects seen at AIFIRA were also replicated at SNAKE using the AutoTarget routine. Part of a cell with elongated mitochondria was targeted making sure not to target the elongated mitochondria themselves. After irradiation, the un-irradiated elongated structures which did not directly receive radiation also depolarized indicating a connectivity with the irradiated area (Fig.21). In addition to this whole network depolarization, a redistribution of TMRE signal which left the irradiated mitochondria was seen. The mitochondria outside the targeted area showed an increased change in signal intensity (white) indicating that the TMRE is taken up by the neighboring mitochondria. This was a further conclusive piece of evidence for the lack of destruction of TMRE but for the redistribution and uptake after irradiation.

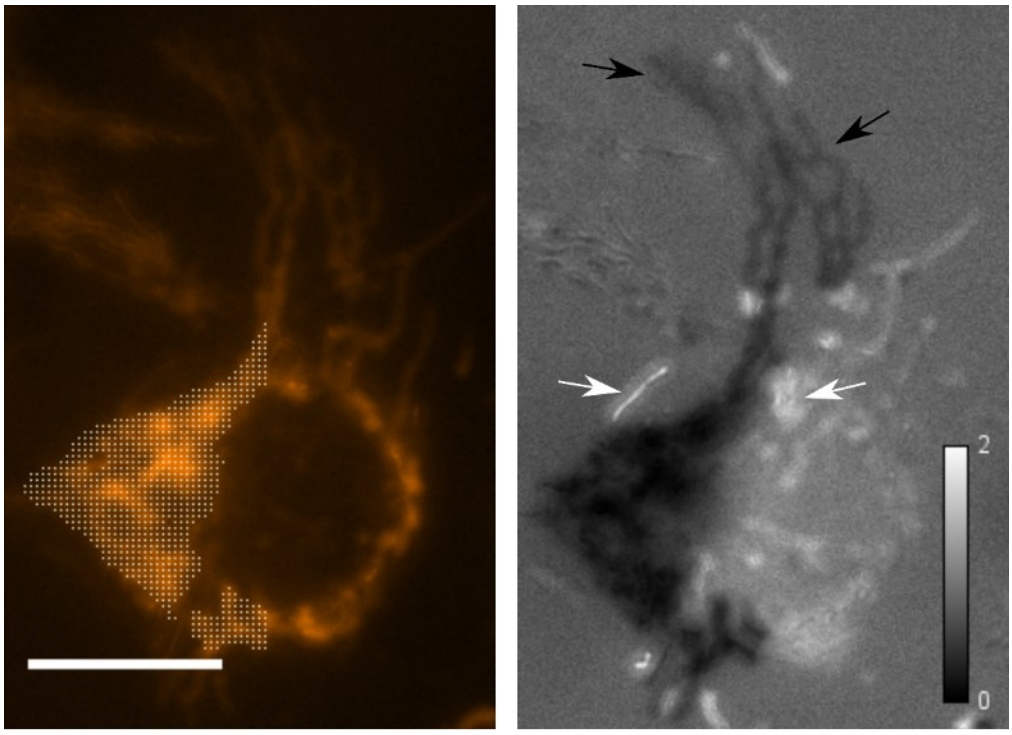

Fig.21: The figure represents TMRE stained mitochondria with an irradiation matrix overlay in the left image. The image on the right is a quotient signal image constructed form the before and after irradiation images (before/after). The greyscale ranges from 0-2 where 0 is a relative loss of signal and 2 is a high relative gain. The arrows point to out-of-field mitochondria which have increased dramatically in TMRE signal intensity after irradiation (white arrows) and out of field mitochondria which were not directly targeted and have also lost their fluorescence intensity (black arrows). The scale bar represents 10µm.

The AutoTarget routine could also be used to perform irradiation of all mitochondria in a cell. A manual selection of the cells of interest was still necessary but the target overlay worked well and in images with decent signal, automatic detection was able to identify the majority of the mitochondria (Fig.22). After detection, it was then possible to target each cell with a different number of ions in order to test for mitochondrial response to varying ion number in the same field of view. The experiments performed in this way were able to induce a much larger scale of depolarization than previously performed with the smaller matrices. However the biggest advantage of the AutoTarget routine was the ability to perform concurrent imaging and irradiation to produce time-lapse videos of depolarization.

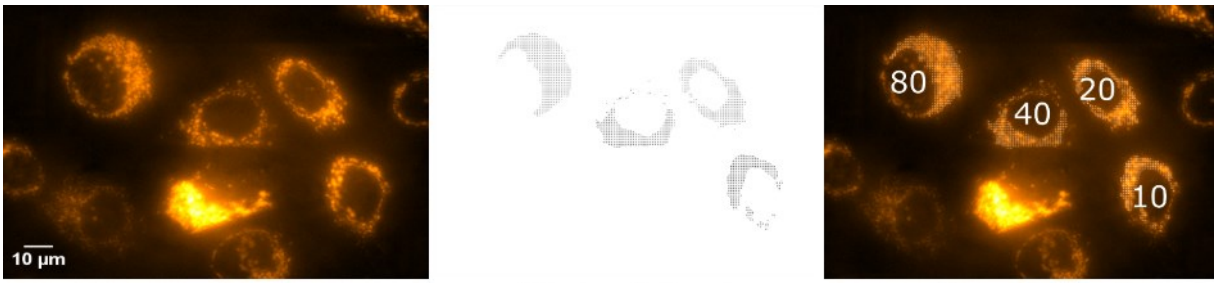

Figure.22 Depiction of a method whereby multiple cells' mitochondria in field can be selected and all mitochondria in each can be irradiated using the AutoTarget macro while using different ion numbers for each cell. The cells before irradiation (left) are then targeted with the AutoTarget macro which yields a point matrix covering all mitochondria (centre). The cells are then irradiated, one after another, with different numbers of ions (80, 40, 20, 10) (right).

6.2.3.2 Live cell imaging analysis of mitochondria during irradiation

The ability to image and irradiate mitochondria concurrently by relying on the stable ion count rate of the SNAKE beamline enabled fast imaging of mitochondria as they were being irradiated. In combination with the "AutoTarget" macro based on a single step of thresholding available in the Zeiss Axiovision software, the targeted irradiation software was able to target all mitochondria in a cell and overlay the targeted area with irradiation points. These technological advances enabled targeted irradiation of all detectable mitochondria and concurrent imaging. The time series obtained with such imaging methods allowed new insights to be gained into the depolarization mechanism and to reinforce even further the concept that biological depolarization was the driving force behind the effects seen and not TMRE destruction.

Analysis of the video files was performed to understand the redistribution of TMRE following radiation induced mitochondrial depolarization. The nucleus, which is naturally devoid of mitochondria was defined as a cytoplasmic background (Fig.23.D (cytoplasm)) and was used to analyze changes in cytoplasmic TMRE levels. Individual mitochondria within the irradiated cells were chosen and a ROI placed around them to measure mitochondrial changes during irradiation. (Fig.23). As the beam of carbon ions was scanned over the overlayed mitochondrial targets the point-like accumulations of TMRE defining the mitochondrial signal disappeared. The time required for mitochondria depolarization is less than that of the imaging system temporal resolution (500ms). The signals captured from the selected mitochondria showed that the last mitochondria to be irradiated had the highest hyperpolarization peak before the depolarization. This overload of TMRE could be explained by the increased background of TMRE in the cytoplasm which has been released from the already depolarized mitochondria. The experiments depicted in (Fig.23 A) were performed with 500nM TMRE solution. Therefore based on the previous results from partial irradiation (Fig.21) the TMRE that was released into the cytoplasm after irradiation could have led to the accumulation of more TMRE in the final mitochondria (highest peak). To test if this was only the case with 500nM, the experiments were also performed with 250nM TMRE as a comparison. The results with 250nM show the same trend. The

redistribution of TMRE to the surrounding mitochondria is however not surprising as the free TMRE changes the equilibrium between mitochondria and non-mitochondrial TMRE. Mitochondria that are still polarized will therefore appear significantly brighter as they are absorbing TMRE from the surroundings.

To fully analyze the TMRE redistribution process, it was important to understand not just the redistribution within the cell but the flow of excess TMRE out of the cell following mitochondrial depolarization and release of TMRE. To do this, extracellular background measurements were taken in four areas in the micrograph where no cells were present and these values were averaged. This background measurement (extracellular BG) showed a slight increase over time during the irradiation process Fig 23B, which could be stipulated to be due to the release of TMRE from the irradiated cell. In comparison a more local effect was measured on the corona of the irradiated cell. In order to do this an area bounding the cell was drawn to define the outline of the cell. Outside of this, a ring was drawn around the cell and measurements were taken in this area over time. Therefore any change in this extracellular area would be related to movement of fluorescent signal in or out of the cell indicating a transfer of TMRE. In this coronal region there was a relatively small but distinct increase in fluorescence intensity. This signal was seen from the moment when the beam started depolarizing mitochondria and reaching its maximum when the last mitochondria was depolarized. The kinetic analysis of redistribution of TMRE in irradiated mitochondria with AutoTarget as shown in Fig.23 was key to dispelling the idea that TMRE has been destroyed or damaged by ionizing radiation. Tracking of the release of TMRE in individual mitochondria (Fig.23B) shows that not only is there an increased cytoplasmic signal directly after the first mitochondria are irradiated and the TMRE leaves the depolarized mitochondria but also that TMRE signal outside of the cell increases as all mitochondria are depolarized and thus lose their specific TMRE signal. The change from a heterogeneous mitochondria specific staining pattern to a homogenous background staining after irradiation is also evident in Fig 23A.

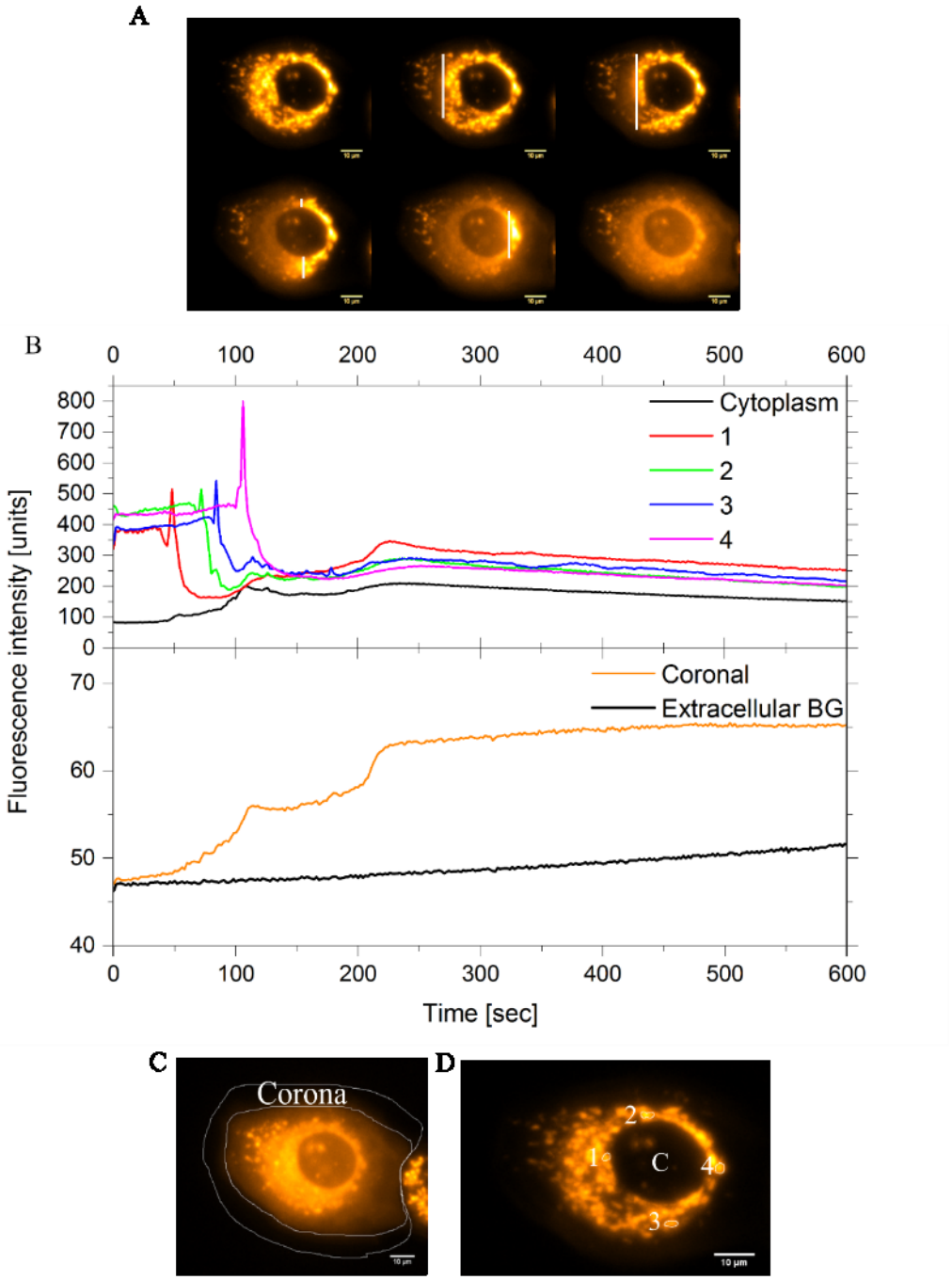

Fig.23: Live cell irradiation analysis: The micrographs (A) show images from the concurrent live cell imaging in which all mitochondria in a cell are irradiated, the white line represents the estimated current position of the beam. The line graphs (B) show the values over time for 4 selected mitochondria (numbered 1-4) and the cytoplasmic background (D) as well as the coronal measurement (C). The graph tracks the release of TMRE into the cytoplasm, the individual depolarization of 4 mitochondria and the release of TMRE to the extracellular space along with an extracellular background value which is measured in frame.

In order to further back up the hypothesis that irradiation of TMRE stained mitochondria lead to a highly localized loss of TMRE which then in turn could be taken up by the surrounding mitochondria, experiments were performed using live cell imaging. A section of a cell was manually chosen and the AutoTarget macro was used to place a matrix of irradiation points over the cell. The area chosen corresponded to a particularly dense region of mitochondria. The beam is then scanned across the point matrix boustrophedonically from top to bottom irradiating all points (left to right). Three measurement areas within the irradiated area were then chosen. The first at the beginning of the irradiation matrix within the first few lines of irradiated points. The second in the middle of the irradiation field and the third at the end of the irradiation matrix. The graph and corresponding micrographs (Fig.24) show that the peak of the fluorescence intensity signal before depolarization, rises the further the area is into the field of irradiation. The graph indicates that the TMRE which is now not present in mitochondria is free and the more TMRE that has been made available means that the later area can reabsorb more TMRE and will therefore show a higher baseline value and higher peak before depolarization.

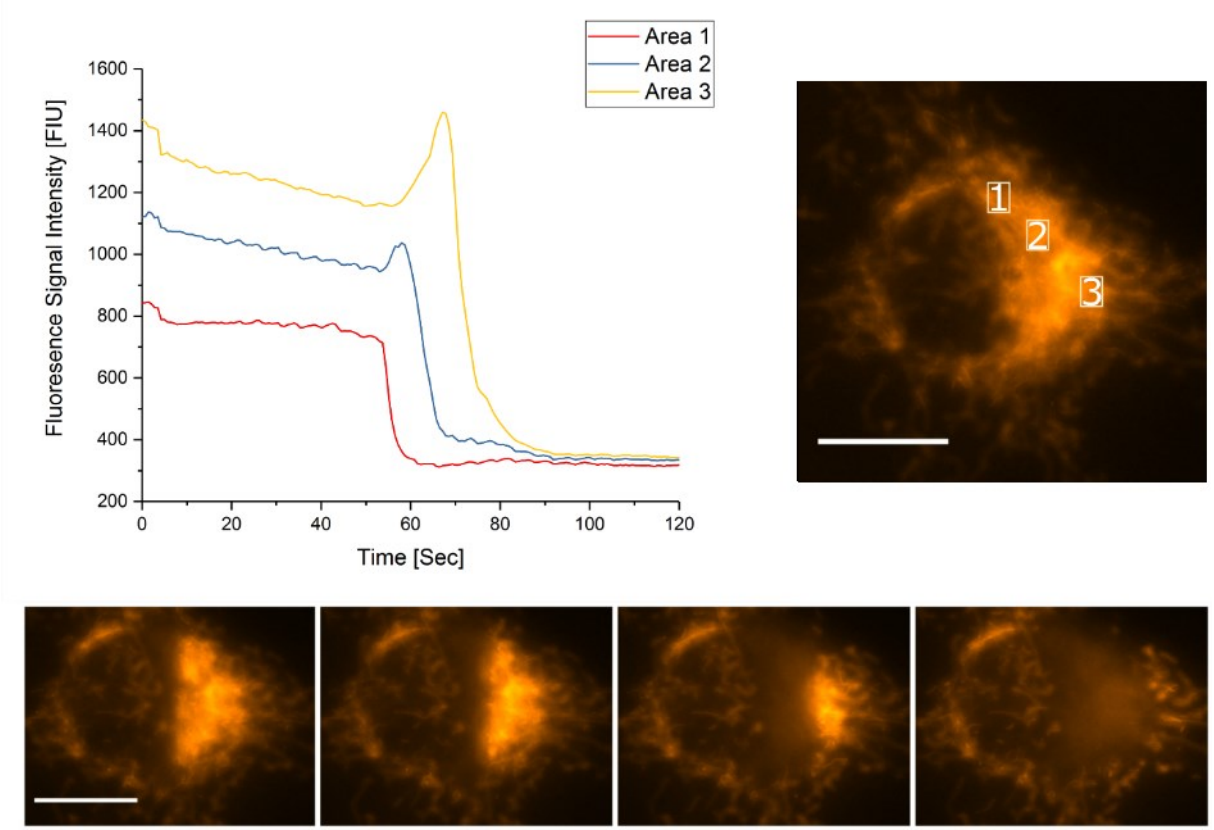

Figure.24: Image sequence depicting the increased peak height just before radiation induced mitochondrial depolarization. The micrograph (upper right) shows the regions of measurement along the area of irradiation. The graph shows an increase in the peak before depolarization the further the area is from the initial start of radiation (sequence 1-3). The increased peak represents the uptake of mitochondria at the end of the irradiation area of the TMRE lost by the initially irradiated areas. Therefore region 3 has a higher peak than region 1 or 2. The lower four micrographs show snapshots from the live cell irradiation from start to end and the extent of the overall depolarized mitochondria. Scale bars represent 10µm.

The experiments investigating TMRE redistribution confirmed the initial hypothesis, the next aim was to compare the radiation induced effect to a chemical induced depolarization to see if there were any differences. Carbonyl cyanide-4-(trifluoromethoxy)phenylhydrazone (FCCP) is an agent known to depolarize mitochondria by uncoupling the proton transport system of the mitochondrial membrane and therefore depolarizing mitochondria (Benz and McLaughlin, 1983).To compare response of radiation induced depolarization and FCCP induced depolarization, 20 mitochondrial areas were irradiated with 6x6 matrices of 80 carbon ions per point, a number of carbon ions known to cause instant depolarization. As an internal control, mitochondria more than 10µm from the irradiated area were chosen. Images were taken before and after irradiation and the areas targeted by radiation were analyzed for mean fluorescence intensity. The maximum loss of potential was seen in the first frame after irradiation (~10s) and so this value was taken for the irradiated areas. Unirradiated control mitochondria in the same cell were analysed for an effect too. The region of interest was also analyzed for mean fluorescence intensity before and after the irradiation event. These data were then compared to an offline experiment using FCCP whereby 10 areas were observed and analysed during live cell imaging of MCF7 cells stained with TMRE and then, depolarized by the addition of FCCP and imaged using the same seconds.

MCF7 cells were plated in 35mm glass bottom live cell imaging dishes (Ibidi) and stained with 500nM TMRE for 30 mins in the incubator. The TMRE was then washed and the cells were imaged. An automatic timelapse imaging sequence was started and FCCP was added to the cells in the dish. The maximum effect of the FCCP happened within a few frames of the addition and the values of two areas in a total of five cells were analyzed before and after FCCP effect. The data was plotted with the data from the irradiation experiments as the imaging settings, staining and cells were the same and could therefore be compared. The resulting plot shows the effect of irradiation and FCCP uncoupling of the membrane potential (Fig.25). The result indicates that the chemically induced depolarization is within the same range as the irradiation induced depolarization although the standard deviation of the two treatments varies (32.5 for Irradiated, 13.5 for FCCP). Radiation induced depolarization shows a wider range of responses than FCCP.

The results further back up the notion that chemically mediated uncoupling of membrane potential and the radiation induced membrane potential loss have the same effect and are the same process albeit with a different mechanism. The strong similarity of effect seen by FCCP and by irradiation in both magnitude and overall effect would suggest as much. The variation in magnitude is likely due to the fluctuation in depolarization efficiency as radiation interacts and causes ionizations and consequently damage in the mitochondria and the cell compared to FCCP which has a direct and selective role on the proton pump of mitochondria.

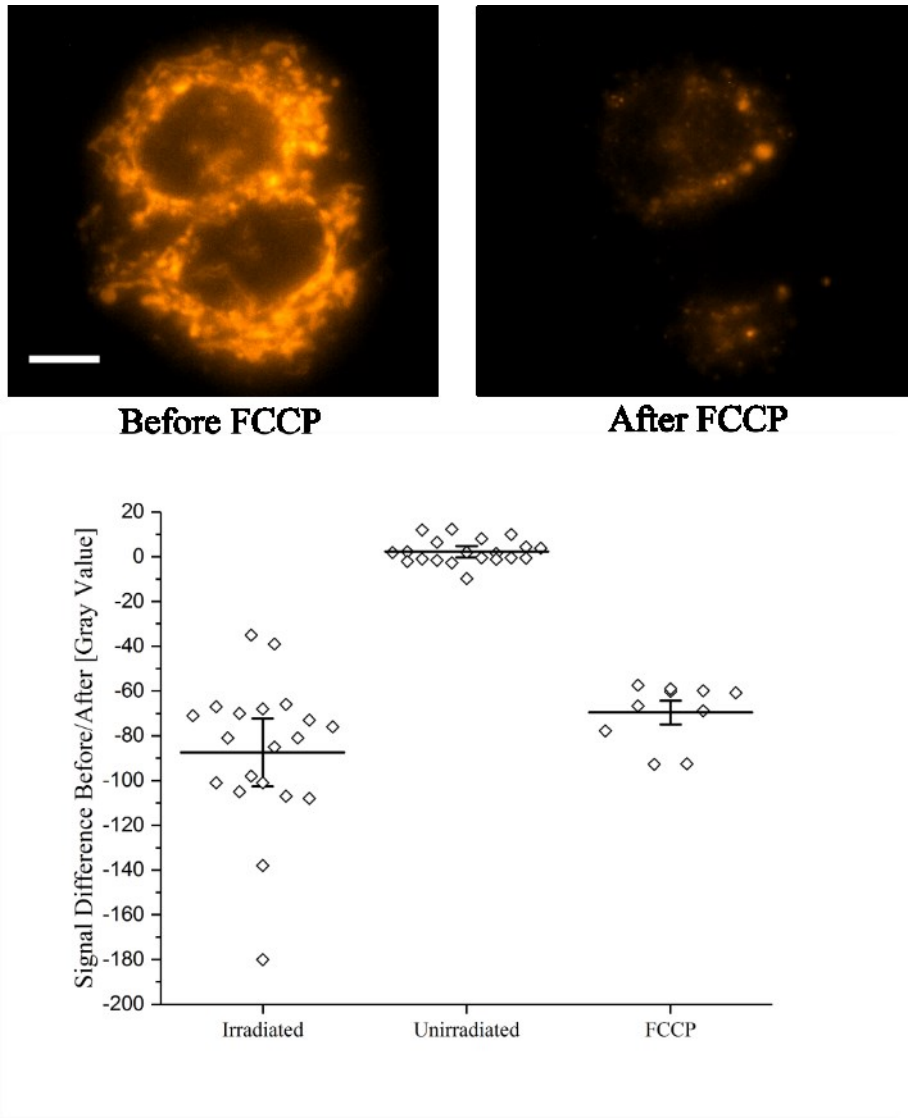

Fig.25: The figure shows a quantification of irradiated (80 carbon ions, 6x6), unirradiated and mitochondria treated with FCCP, a known membrane potential decoupling agent. The graph shows the difference in signal before and after irradiation. In the case of the unirradiated sample the same time points on the same micrographs were chosen and mitochondria in the same irradiated cell but outside of the irradiated area were analyzed. FCCP experiments were performed offline with the same microscope settings and staining procedures and the images were taken as "before FCCP" and "after FCCP" as the lowest value after FCCP induced depolarization. The diamonds represent measured values, the horizontal line represents the mean and the error bars represent the 95% CI of the mean.

Non-cancer cell lines

All the experiments described previously were performed on cancer cell lines MCF7 and A549. Mitochondrial function has previously shown to be different in cancer cells compared to non-cancerous cell lines (Zong et al., Amoêdo et al., 2013). In order to investigate whether any difference in depolarization response following targeted irradiation could be perceived, human fibroblast cell line EA.Hy 926 were irradiated in the same fashion. One hundred carbon ions per point were applied to Ey.Hy 926 mitochondria in a 6x6 matrix. The result was the same as was seen in both A549 and MCF7 cells, total depolarization in the targeted area straight after irradiation (Fig.26). This test dispelled the idea that non-cancerous mitochondria would react in a different way to ionizing radiation. The depolarization effect seen is therefore not related to the differences in mitochondria between cancerous and non-cancerous cell lines but upon a common response to the energy deposition in the mitochondria.

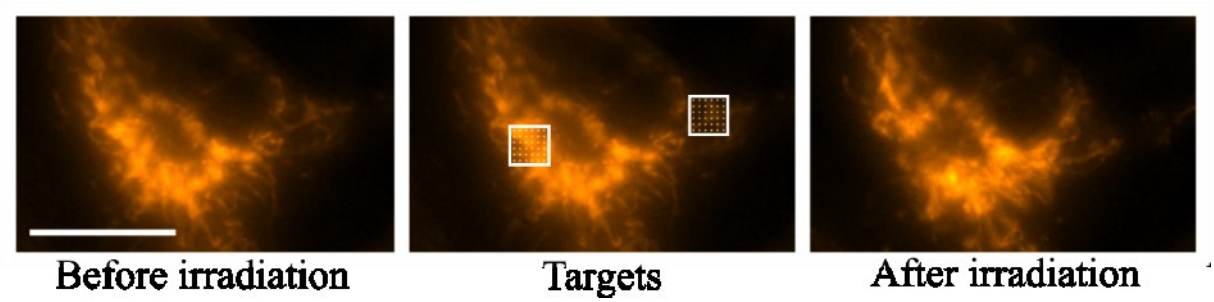

Fig.26:The micrographs depict EA.Hy 926 "normal" cell line before irradiation, with two overlayed 6x6 targets (100 Carbon) and directly after irradiation. The micrographs show that a highly localized loss of TMRE is seen in both of the irradiated areas.

6.2.3.3 Nernstian image analysis

Quantification and measurement of the mitochondrial membrane potential is a topic which has been widely discussed and analyzed in the literature. Apart from complex and highly technical patch clamp measurements on extracted mitochondria using electrodes to measure mitochondrial potential in a sealed vessel, secondary methods of measurement using cationic fluorescent chemicals have become increasingly popular as an alternative to the cumbersome and complex electrophysiological setups (O'Reilly et al., 2003, Scaduto Jr and Grotyohann, 1999). TMRE is widely used as a candidate for measurement of membrane potential as it is cationic and therefore accumulates readily in polarized mitochondria. TMRE is a single positively charged cation and can therefore be integrated into the Nernst equation to assess the equilibrium potential for the ion. The Nernst equation is used to calculate the potential difference which is established across a cellular membrane based on the charge and concentration gradient of an ion.

Nernst equation.

$$V_{eq} = \frac{RT}{zF} \ln \frac{[X]_0}{[X]_i}$$

where:

V_{eq} is the Nernst potential for the calculated ion (Volt)

R is the universal gas constant (8.314 Joule $K^{-1}mol^{-1}$)

T is the temperature in Kelvin at which the experiment took place

z is the charge of the ion chosen (for TMRE which takes the value of +1e)

F is Faraday's constant (96485 Coulomb. mol^{-1})

$[X]_0$ is the concentration of the ionic species outside of the cell

$[X]_i$ is the concentration of the ionic species in the mitochondria

When applying the Nernst equation to mitochondria and TMRE in this fashion it is important to take some experimental and imaging parameters into account to ensure that the value best reflects the mitochondrial membrane potential. From the literature it is known that loading of the cells with TMRE must occur in such a way that equilibrium of TMRE in the mitochondria is achieved (Perry et al., 2011). The cells are incubated at 37°C with TMRE containing growth medium for 30 minutes before being washed with pre-conditioned medium to ensure that the concentration of the TMRE present in the background is kept to a minimum. Next it is vital to ensure that the background signal (Dark current) of the Zeiss CCD is established as this can also alter the calculated value of membrane potential. To perform the background reduction, blank images (no cells, no dye) are taken with the CCD corresponding to various exposure times used experimentally (300ms, 500ms, 1000ms) without the presence of a light source. The average value of all of the pixels in the frame for the exposure time used was then subtracted from all images taken to ensure as little contribution of the noise as possible. Furthermore excitation light settings were kept sufficiently low that no phototoxic effects could induce spontaneous depolarization events. If all of these parameters are taken into account it is possible to achieve reproducible results which match those published in the literature on mitochondrial membrane potential (Scaduto Jr and Grotyohann, 1999).

This analysis method to determine the magnitude of the mitochondrial membrane potential was performed in Fiji using a simplified version of the Nernst equation –59log (A/B) (Lemasters and Ramshesh, 2007). The equation was applied to every pixel of every frame of the time series in question using the "image expression parser" integrated into Fiji. The values A and B in the simplified Nernst equation are the values of the individual mitochondrial pixels (A) and the extracellular fluorescence (B) intensity respectively. Using this simplified expression it was possible to create false-colour micrographs in which the more negatively charged mitochondria are darker and the extracellular background hovers between 0-10 grey values (Fig.27). The representation is a simplified visual representation of the mitochondrial membrane potential and its variation throughout the cell. The micrograph also shows a raised intracellular signal corresponding to the plasma membrane potential, indicating a raised level of free TMRE within the cell but outside of the mitochondria.

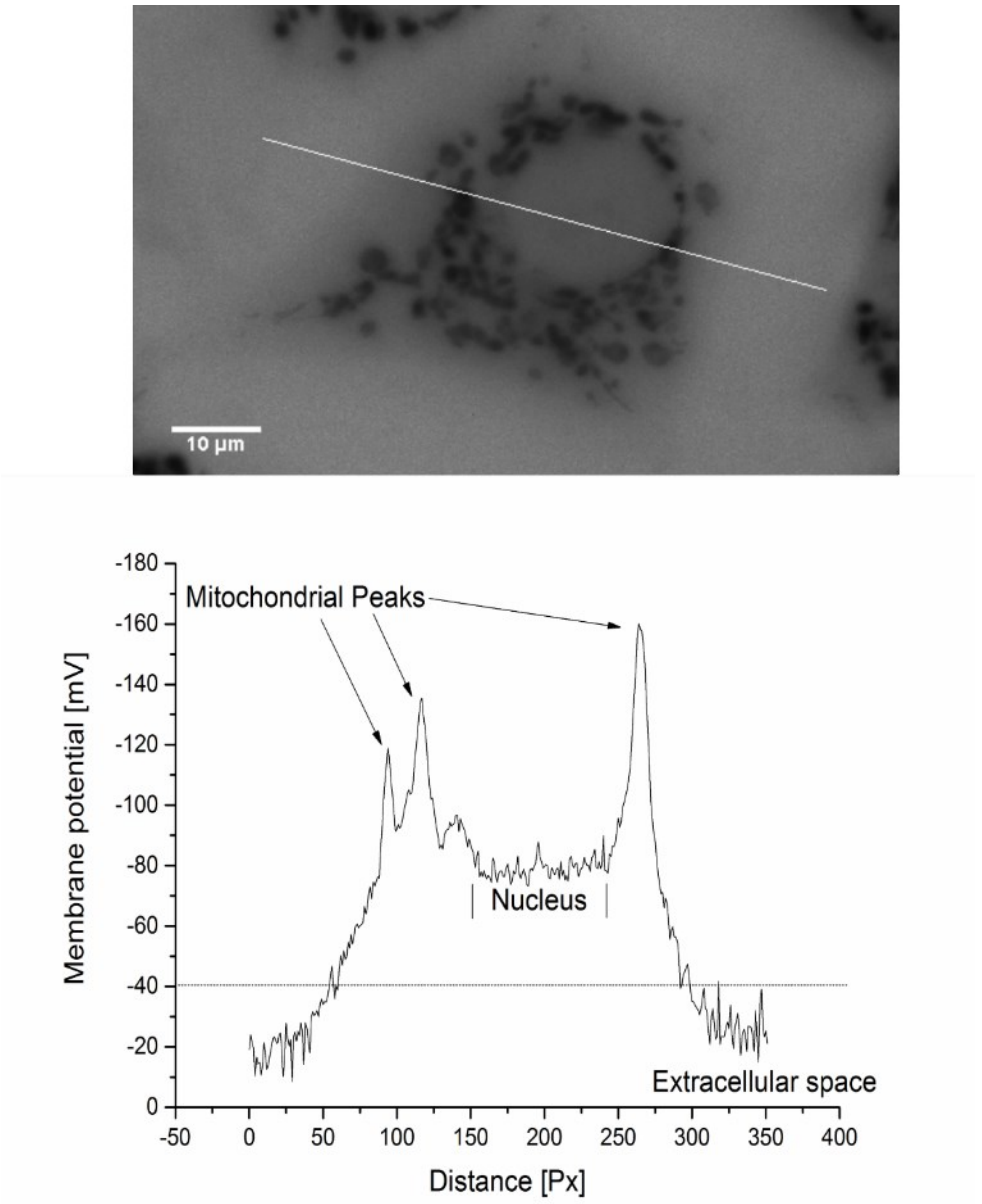

Figure.27: The upper figure shows a pseudocolour image of mitochondria which have been stained with TMRE and each pixel has been calculated by the simplified Nernst equation in relation to the extracellular background values from 4 fields in the same micrograph but outside of the cells. The darker the region, the lower the membrane potential is. The lower graph shows a section taken over the upper micrograph showing a relative cross section of the cell and the mitochondrial peaks along with the intracellular background over the nucleus and the extracellular space.

6.2.3.4 Energy deposited in mitochondria following targeted irradiation

In order to further understand this radiation induced mitochondrial membrane depolarization, experiments were performed at SNAKE and AIFIRA to see if there was an energy threshold below which depolarization does not occur. A standardized radiation matrix was created consisting of 6x6 points spaced 0.5µm apart for the irradiation with the 1µm beam spot at SNAKE. A corresponding irradiation matrix was setup at AIFIRA with 1µm between irradiation points for the AIFIRA beam spot of 2µm. Using these irradiation matrices equivalent quantities of energy could be deposited per unit area in Munich and Bordeaux at the same rate.

Using this setup and a calculation of equivalent energy deposited based upon carbon ion irradiation at SNAKE and optimized for the proton irradiation at AIFIRA, a comparison of two high LET particles; carbon ions (LET 350 kev/µm) and protons (~10 kev/µm) could be performed. The details of the conversion are covered in 3.6.3

After determining that mitochondrial depolarization was in fact a biological process and showing the redistribution of TMRE after irradiation using live cell imaging, the question arose what effect the number of applied ions had on depolarization. To further asses the relation of the ion number to the effect observed in the experiments at SNAKE and AIFIRA were performed with varying numbers of ions. The number of ions per irradiated point ranged from 100-10 carbon ions and 3500-700 protons (17 – 1.7 kGy, in the 6x6 matrix area). Experiments at SNAKE have already defined that 100 ions per point leads mitochondria to completely depolarize and not repolarize within the observation times. It was therefore of interest to determine at what number of ions this effect is no longer seen. We first defined three categories of state post-irradiation which best defined the results seen: total depolarization, which is the total loss of signal in a mitochondria without recovery of the signal; partial depolarization, a prolonged loss of signal followed by a partial recovery in specific signal and or a flickering; no depolarization, i.e. no prolonged loss of signal. Examples of these three event categories are shown in Fig.28.

To calculate the energy deposited in Gy the equation below is used.

$$\text{Dose} = \frac{0.16 * \text{LET} * \text{Particle Nr}}{\text{Area}}$$

Dose: is given in Gy (Joule/Kg)

LET: is given in keV/µm

Area: is given in µm²

Therefore when using the 6x6 point irradiation pattern with an area of 11.56μm² and a total of 36 irradiation points (Fig.6) with 100 Carbon ions per point (LET at cells of 350 keV/μm) the dose in the area is 17.4 kGy. If the irradiated area is defined as a cuboid with depth 1μm and sides of 3.4μm and the change in LET of the particle is negligible then the energy deposited in the target area is 2.02×10^{-10} Joule. The same amount of energy is therefore deposited for the equivalent 3500 protons per point applied at AIFIRA when the application error of ± 25% is not included.

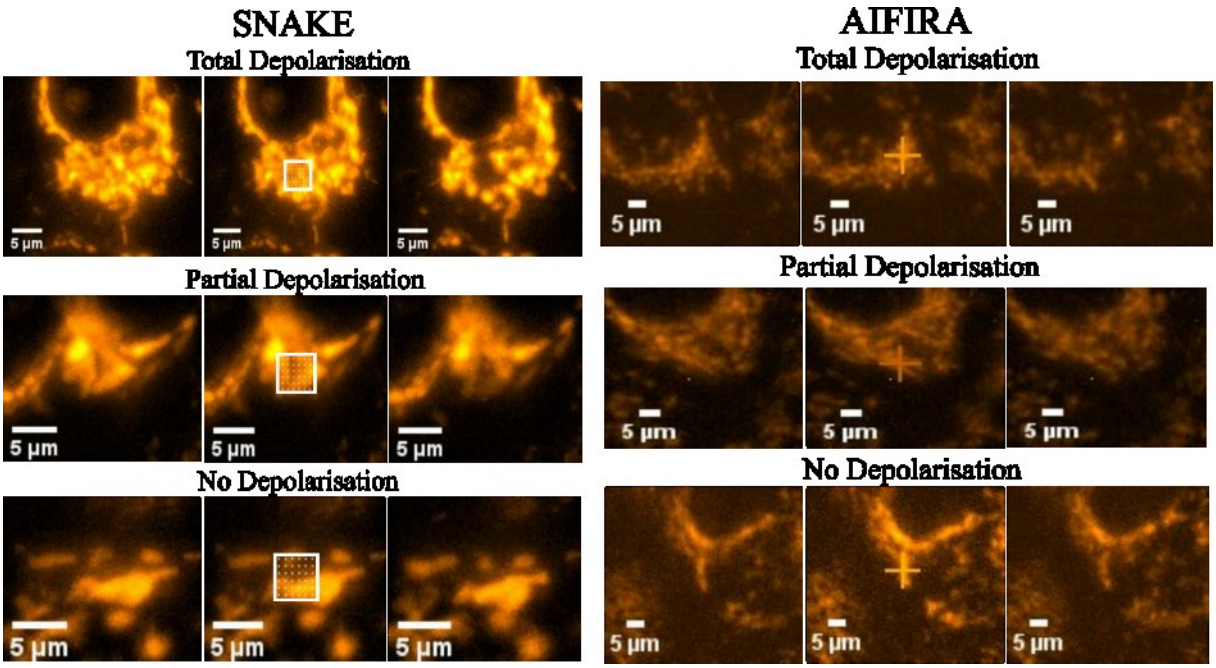

Figure.28: Two sets of micrographs from SNAKE and AIFIRA experiments which show the varying effects of radiation, on the mitochondrial membrane potential. Each triplet of images shows the cell before irradiation, with targets and after irradiation and is grouped into the overall effect type; total, partial and no depolarization. For total depolarization, micrographs with 100 carbon ions and 3500 protons are shown; partial depolarization 40 carbon ions and 1500 protons; no depolarization 20 carbon and 700 protons per point are depicted. The cross in the AIFIRA images represents the center of the targeted area.

With the categories defined, the results of each irradiated cell at SNAKE and AIFIRA could be assigned into each category for the number of ions applied to the mitochondria in question (Fig.29). The results indicated that given 100 carbon ions or 3500 protons per point, all mitochondria depolarized and no mitochondria showed a different response. At 50 carbon ions per point, there was already a large proportion of cells (>40%) that showed a partial effect, ie. an initial dip in fluorescence signal intensity with a returning signal but lower than the starting signal. When further decreasing the ion numbers the total depolarization effect disappeared and the majority of cells either showed only a partial effect (flickering) of no change in signal after irradiation. Even the lowest number of carbon ions applied (10 carbon ions) would, if targeted in a single point to the nucleus induce ~6 Gy dose to the whole nucleus. 6 Gy applied to the nucleus would under normal conditions, lead to a cellular response which in ~70% of the cells would end in cell death. The results from both AIFIRA and SNAKE indicate that mitochondria in relation to instant membrane depolarization at least, are highly radio resistant. The results show that large numbers of ions are required to induce this instant and total depolarization event. However since the experiments were only done with larger ion numbers over short times (up to 30 minutes) the results cannot be used to extrapolate down to lower ion numbers and the longer term effects of these irradiation procedures over time. It is however very possible, that cellular responses to such high numbers of ions may well present themselves hours or days after irradiation. There was no sign of instant cell death, in the form of detachment, disintegration or membrane bubbles as could possibly be expected by cells challenged with such high numbers of ions.

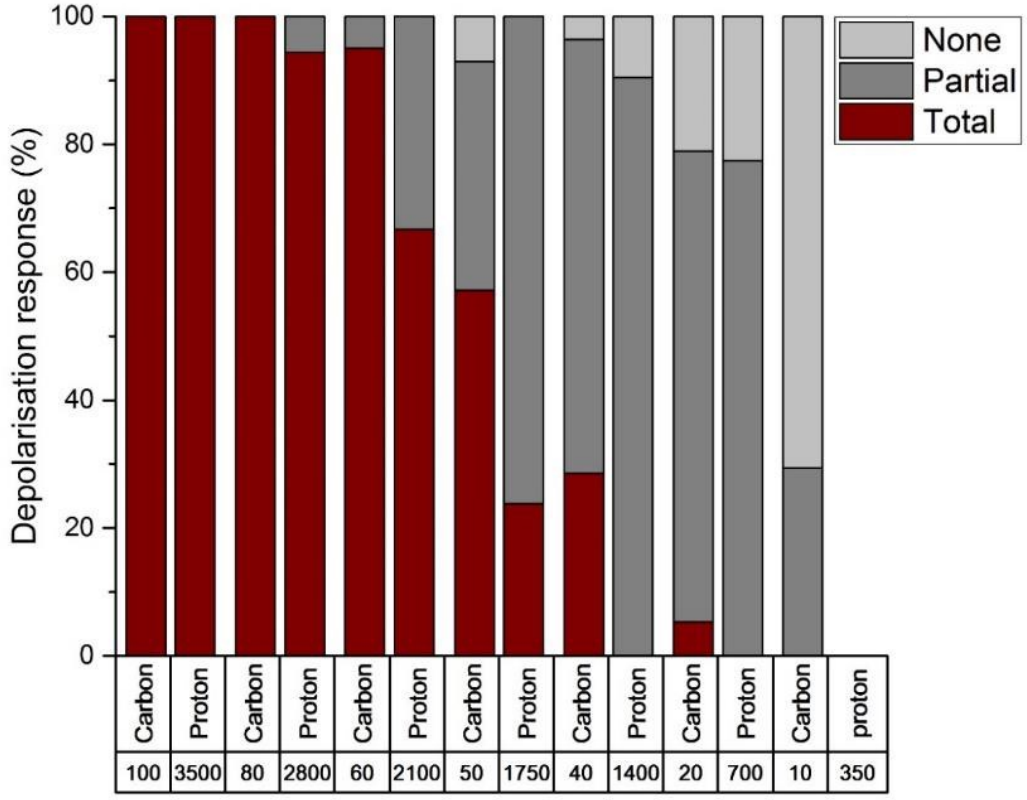

Carbon ions per point (6x6)	Cells Irradiated	Total		Partial		None	
		Nr	%	Nr	%	Nr	%
100	4	4	100.0	0	0.0	0	0.0
80	20	20	100.0	0	0.0	0	0.0
60	20	19	95.0	1	5.0	0	0.0
50	28	16	57.1	10	35.7	2	7.1
40	28	8	28.6	19	67.9	1	3.6
20	19	1	5.3	14	73.7	4	21.1
10	17	0	0.0	5	29.4	12	70.6

AIFIRA

Protons per point (6x6)	Cells Irradiated	Total		Partial		None	
		Nr	%	Nr	%	Nr	%
3500	19	19	100.0	0	0.0	0	0.0
2800	18	17	94.4	1	5.6	0	0.0
2100	12	8	66.7	4	33.3	0	0.0
1750	21	5	23.8	16	76.2	0	0.0
1400	21	0	0.0	19	90.5	2	9.5
700	31	0	0.0	24	77.4	7	22.6

Fig.29 Histogram depicting the quantification of polarization state of irradiated mitochondria for experiments at SNAKE (carbon ions) and AIFIRA (protons). The overall percentage of cells featuring total, partial or no (none) depolarization are plotted above the number of carbon ions per point (100-10) and equivalent protons (3500-350), both ion types decreasing to the right, required to deposit the same amount of energy in a 6x6 irradiation point matrix. The number of cells analyzed and the outcomes are displayed for SNAKE and AIFIRA in the tables below.

6.2.3.5 CyclosporinA, an initial test for a mechanism behind the depolarization

Mitochondrial depolarization in cells undergoing apoptosis or in "flickering mitochondria" is, in the literature, often attributed to mitochondrial membrane transition pore (MTP) formation. MTP formation is a phenomenon which has been investigated and documented widely in the mitochondrial field. Briefly, the IMM opens causing a temporary pore through which the built up charge across the IMM can equilibrate. The process is suspected to be involved in depolarization, which precludes cell death by means of apoptosis (Halestrap, 2009). It was therefore possible that the near instant mitochondrial depolarization that was visualized after targeted irradiation could be related to the opening of the MTP. A known inhibitor of the MTP, CyclosporinA (CsA) was acquired and a test conducted. CsA is widely used in the literature to inhibit MTP opening and at concentrations of 10µM is known to nearly totally block the formation of the MTP.

CsA was therefore an ideal candidate to test if targeted irradiation induced MTP opening. Cells were pre-treated for 20 minutes with 10µM of CsA and TMRE for mitochondria visualization, then irradiated at the beamline at SNAKE (Fig.30). All mitochondria in the cells treated with CsA were irradiated using the "AutoTarget" macro. When applying 100 carbon ions per point all the mitochondria targeted depolarized. The result indicated that there was no difference between CsA treated cells and cells in previous experiments where no CsA was added. The unirradiated cells showed no change, as observed in other experiments.

These initial experiments are an indicator that MTP does not play a major role in the depolarization seen after targeted irradiation. It may also be a further indicator that the damage is not solely a biological process, such as the opening of a pore, but more likely by damage caused by ionizing radiation to the mitochondrial structure leading to the loss of polarization. The initial results indicate that CsA does not afford any protection to the depolarization induced by radiation.

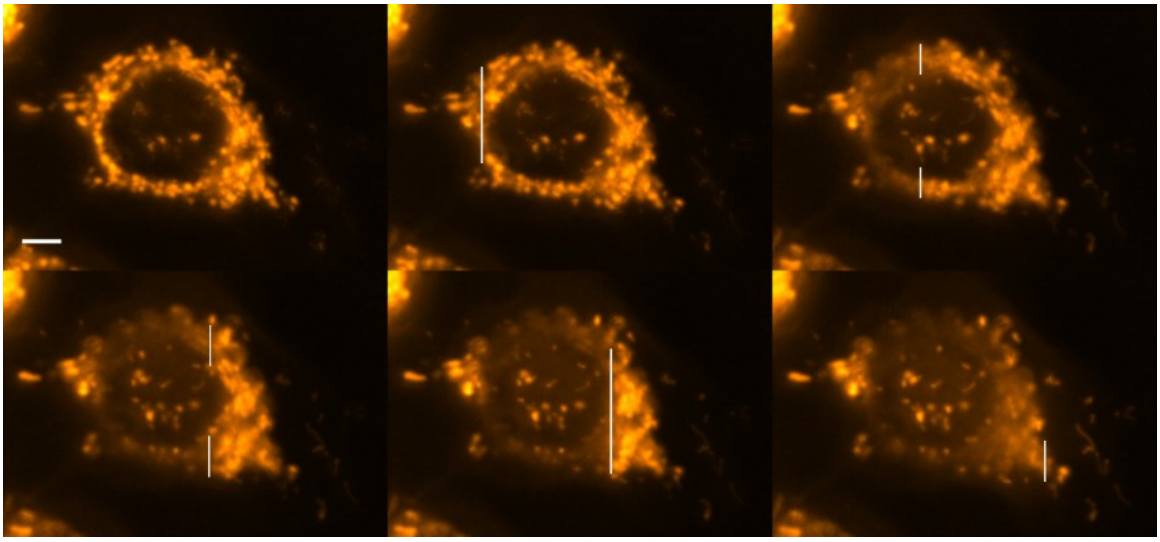

Fig.30 The figure shows a cell being irradiated in real time using the concurrent irradiation and imaging technique. The MCF7 cell has previously been treated with CsA for 30 minutes which acts as a blocker of the MTP. The beam position is estimated by the white line. Scale bars represents 10µm

6.3 Mitochondrial membrane integrity

6.3.2 MTG overview and specific methods

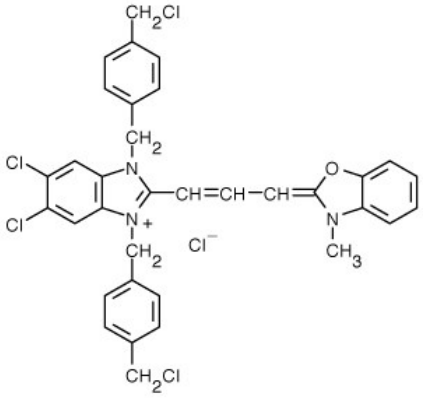

Mitotracker Green (ThermoFischer)

When trying to understand the effects of the irradiation on the mitochondria and the cell as a whole it was important to investigate the mitochondrial membrane integrity following targeted mitochondrial irradiation to see if damage to the membrane could be the dominating factor in the response seen. As the mitochondrial membranes are the physical barriers that enable mitochondrial potential to be maintained it was of interest to see if the membranes are physically damaged by ionizing radiation. Mitotracker green (MTG) is a mitochondria targeted fluorophore commercially available through Thermofischer. The fluorophore is plasma membrane permeable and is readily taken up by live cells and can be excited at a peak of 490nm and emits at a peak of 516nm. MTG is widely believed to be integrated into the mitochondrial outer membrane and is usually used as a marker for mitochondrial mass (Pendergrass et al., 2004). The dye, once loaded into living cells exhibits a strong mitochondria specific signal (Fig.31) due to its integration into the membrane. The dye is widely acknowledged not to be membrane potential dependent (Kholmukhamedov et al., 2013b). The localization of the dye in the membrane makes it an ideal candidate to understand the response of the mitochondrial membranes to targeted irradiation.

An elegant experimental approach would have been the imaging of both MTG and TMRE in the same cells sequentially to understand depolarization and membrane integrity at the same time. However due to the amount of dye and the overlap in Ex/Em spectrum, some initial test experiments showed that light-induced phototoxic damage and consequent depolarization are unavoidable in this experimental setup. The results gained from such an experiment would therefore contain depolarizations induced by light as well as those produced by radiation and untangling the two causes for depolarization would not yield reliable results. For this reason MTG staining experiments were performed in the absence of TMRE, however with the same total number of ions applied to the areas as in the experiments using TMRE.

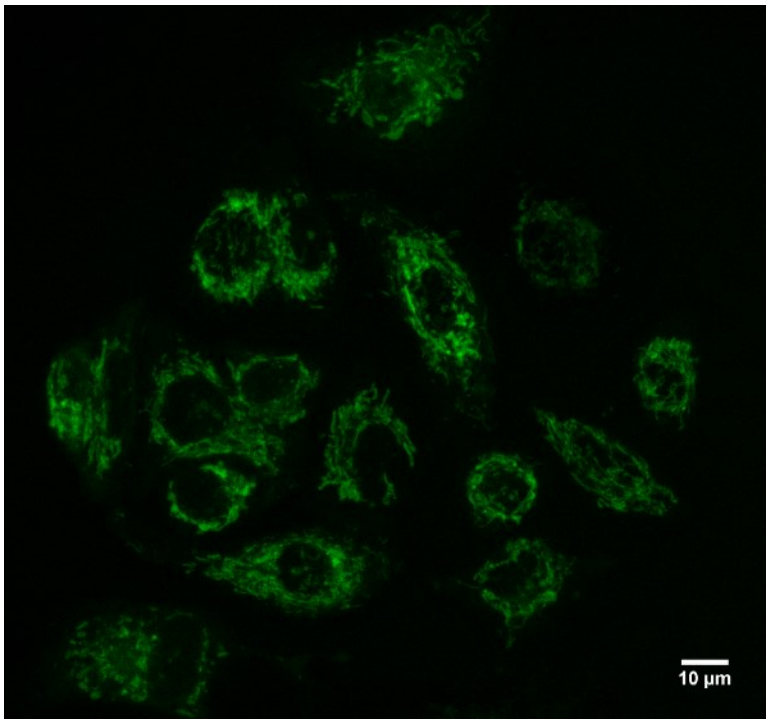

Fig.31 The figure shows a z-stack projection of all mitochondria in the mitotracker green stained MCF7 cells. Cells were imaged offline using the Leica SP8 confocal microscope.

6.3.2.1 Experiments using MTG

MTG staining at a final concentration of 200nM was performed on MCF7 cells during beamtimes at SNAKE and AIFIRA. As the stain is specific to the mitochondrial membrane, any alterations with regard to mitochondrial membrane integrity could be analyzed after targeted irradiation of mitochondria. Carbon ion irradiation of MTG stained mitochondria with an 8x8 matrix and 100 ions per point at SNAKE showed no changes in fluorescence intensity signal of MTG (Fig.32). A slight blurring of the samples was observed when imaging at SNAKE which is believed to be attributed to a short term loss of focus during the experiment. The same experiments were repeated twice at SNAKE with a total of 21 cells irradiated with an 8x8 matrix and 100 ions per point. The irradiated mitochondria with MTG dye showed no fluorescence intensity change after irradiation. Fig.32 depicts montages of 5 cells imaged at SNAKE showing cells before irradiation, with irradiation targets and cells after irradiation. Intensity plots of 20 pixel thick lines drawn over 11 cells show the signal across the irradiated area before and after irradiation (Fig.33), also here no great changes are detected as compared to the TMRE signal (Fig.34). The lack of signal intensity change seen in these irradiated cells indicates no change in mitochondrial membrane and no destruction of the MTG dye itself. The results indicate no visible change in OMM using fluorescence microscopy. In comparison the same irradiation matrix with the same ion number completely depolarizes targeted mitochondria.

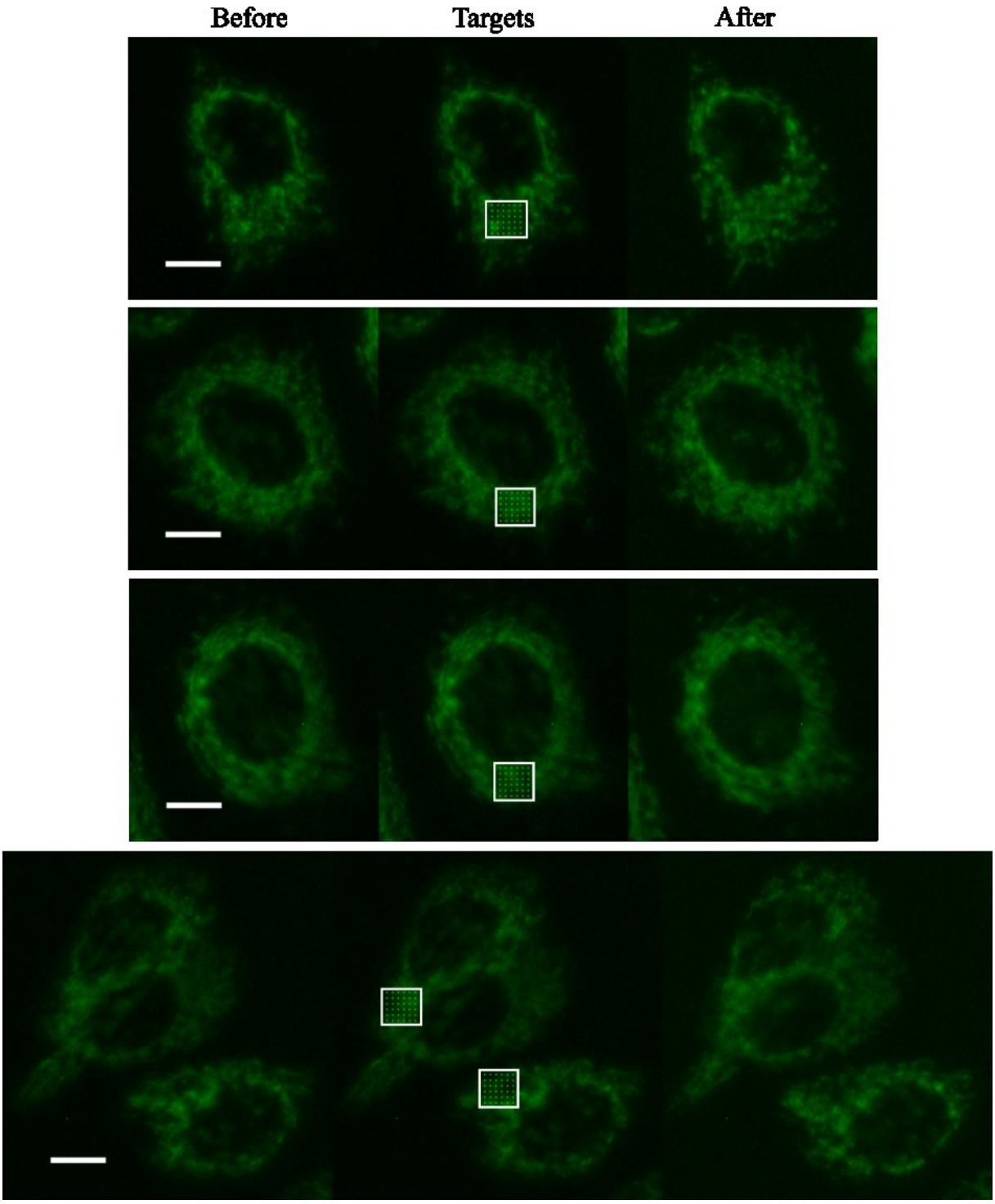

Figure.32 Micrographs of MTG stained MCF7 cells. The first image in each triplet is the image before irradiation, the second image shows the radiation targets superimposed on the unirradiated image and the third image shows the image after irradiation. The micrographs show six MTG stained MCF7 cells before and after irradiation. There is no change in MTG signal after radiation with 8x8 matrix and 100 carbon ions per point. The scale bar represents 10μm.

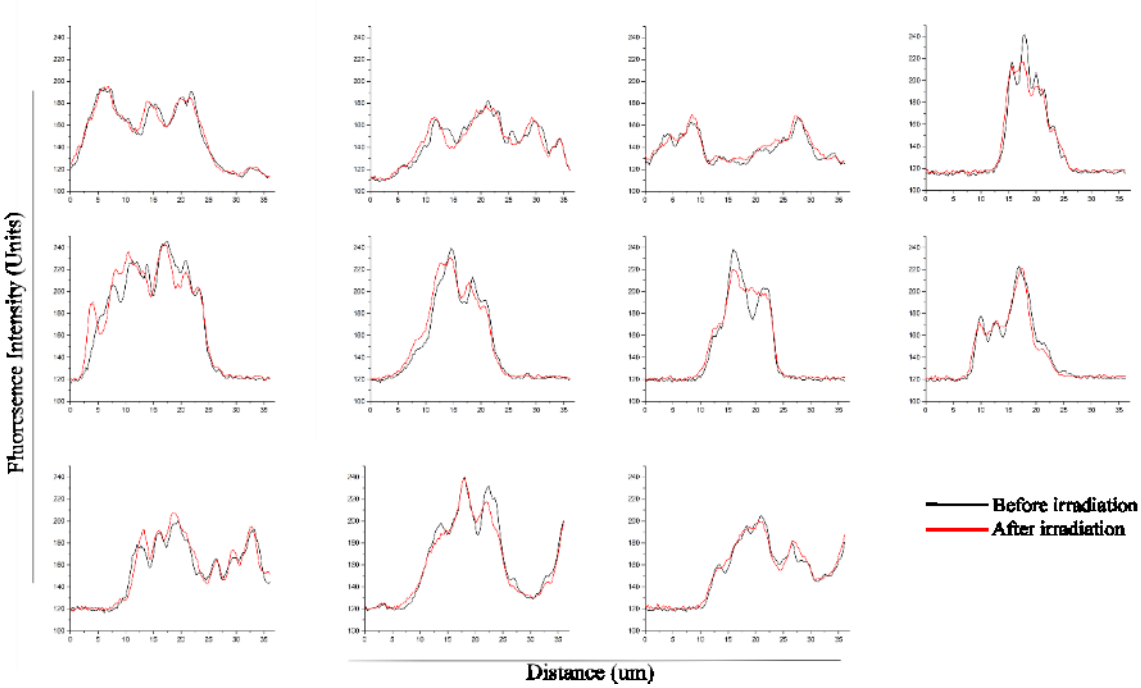

Fig.33 Quantification of MTG signal from 11 irradiated areas. The graphs show the averaged signal before and after irradiation of 11 mitochondrial regions stained with MTG. No major changes are seen in the micrographs indicating no loss in fluorescence intensity.

Although no direct change in MTG signal was observed after targeted irradiation at SNAKE this is not conclusive evidence that there was not a change to the mitochondrial membrane integrity. Damage to the membrane can manifest itself in many ways and small structural changes such as nanopore formation may indeed occur and not change the MTG signal. Further investigation to determine if membrane damage was a factor in mitochondrial depolarization test was performed to verify if the plasma membrane encompassing the cell was damaged after irradiation. Since the ions traverse the membrane and the cytoplasm surrounding the mitochondria and the energy deposited by a particle per nm is the same it may well be possible to correlate damage induced to the plasma membrane to mitochondrial membrane damage.

A decrease of MTG signal was however observed when a very high number of ions were applied to mitochondria in a single cell. These results were seen at both SNAKE and AIFIRA. In the range of 100 000 carbon ions (in the micro Joule range) a highly specific loss of MTG was seen followed by the bursting of the plasma membrane. In Bordeaux a 40x30 matrix large enough to cover a single cell was placed over the cell and 7000 protons per point were applied (8.4 million protons in total as shown in Fig.34) The slight decreases and loss of clarify if the MTG signal as seen here was however not very surprising as applying 8.4 million protons to a cell is an enormous stress and a loss of any fluorescence signal would be expected given these numbers.

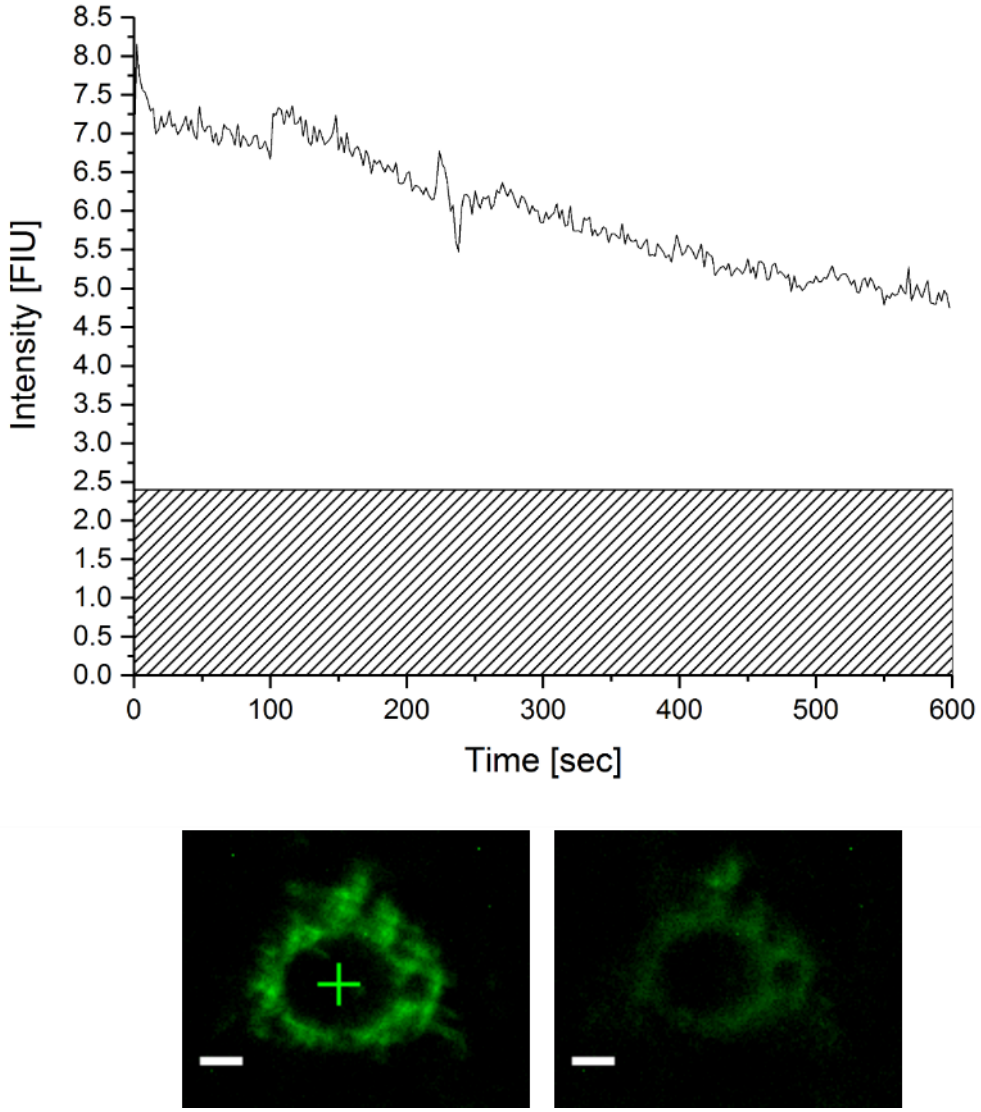

Figure.34 The loss of MTG fluorescence intensity is shown as a graph (upper) and with the corresponding micrograph (lower). MTG signal can be destroyed when the whole cell is bombarded with high numbers of protons (total of ~8.4x10^6).The cross represents the center of the 40x60 target matrix within which the protons were applied. The signal decreases during the radiation process, but was not observed to reach the extracellular background level (shaded area in graph).

6.4 Plasma membrane integrity

The plasma membrane of a cell is a highly dynamic phospholipid construct containing many integrated proteins and pores for cellular transport and signaling. This membrane is the cell's first form of defense from the extracellular space. For this reason damage to the extracellular membrane, if sufficiently extensive almost always will lead to aberrant effects within the damaged cell. The analysis of membrane integrity was vital to determine if targeted irradiation of mitochondria also induced plasma membrane damage. Such experiments require a marker for membrane integrity which would not interfere with the TMRE signal and could reliably distinguish cells with an intact membrane from those with structural damage in their plasma membrane. Two chemical dyes were potential candidates, propidium iodide (PI) and 4',6-Diamidino-2-Phenylindole, Dihydrochloride (DAPI) (Cummings et al., 2004). Both dyes act in the same way as they are cell-impermeable at low concentrations (Fig.35). After experiments with both PI and DAPI, it was found that DAPI was, even at low concentrations rather cell permeant compared to PI. When testing membrane disruption with 70% Ethanol and Triton-X100 in the presence of DAPI, it was found that even before mitochondrial membrane disruption was visible a DAPI specific nuclear signal was visible (Fig.36). Furthermore when testing background DAPI stain at experiments using AIFIRA a distinct DAPI signal was visible even before irradiation experiments had started.

These problems were not encountered with PI which was therefore an ideal candidate for this task as at low concentrations (1µM) it can be added to the cell's growth medium and will not actively penetrate intact membranes. In addition it shares the excitation/emission spectrum with TMRE while having a very different staining pattern. This feature enabled imaging of the effect of both dyes simultaneously. If the membrane of an irradiated cell would become porous, due to direct or indirect membrane damage then PI would be able to enter the cell and intercalate with the DNA, causing a specific nuclear fluorescence signal (Fig.35). Since the excitation/emission spectra of TMRE and PI overlap to a large extent, it is possible to monitor both dyes simultaneously unlike with DAPI. The signals of TMRE and PI are sufficiently different that crosstalk between the two dyes is negligible. TMRE staining is a specific mitochondrial signal and has a low homogenous cytoplasmic background. PI on the other hand is very weakly fluorescent in media, no cytoplasmic presence while the plasma membrane is intact, and only becomes detectable when intercalated with DNA forming a specific nuclear signal with a highly defined structure. Using two dyes with the same excitation/emission also reduces the amount of light exposure as no second excitation light is required which in turn could cause photactivation effects in TMRE resulting in unwanted depolarizations.

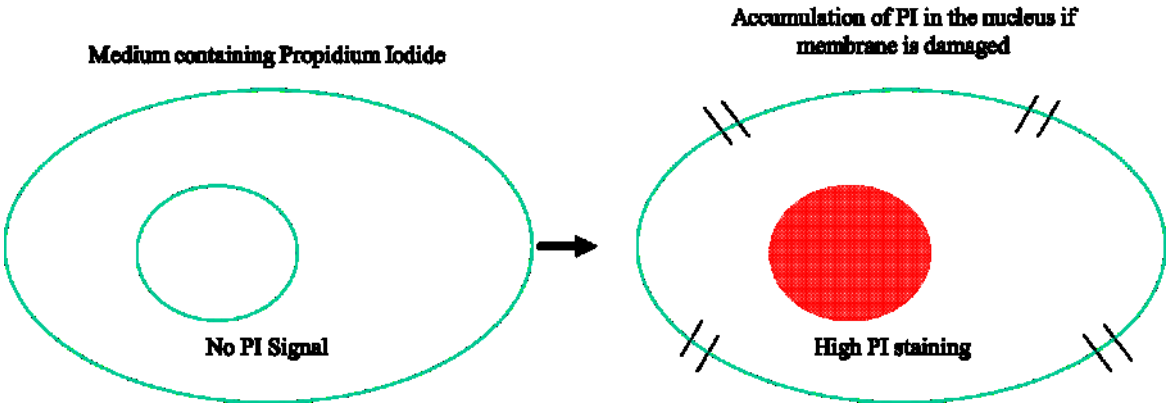

Figure.35: Depiction of the method by which PI tests for plasma membrane integrity. The cell depicted by an oval (cell membrane) and a smaller oval inside (nucleus) is maintained in medium containing 1µM PI which cannot enter the cell if the membrane is intact. However if the membrane were to become leaky or damaged PI would enter the cell and stain the DNA in the nucleus leading to a nuclear signal.

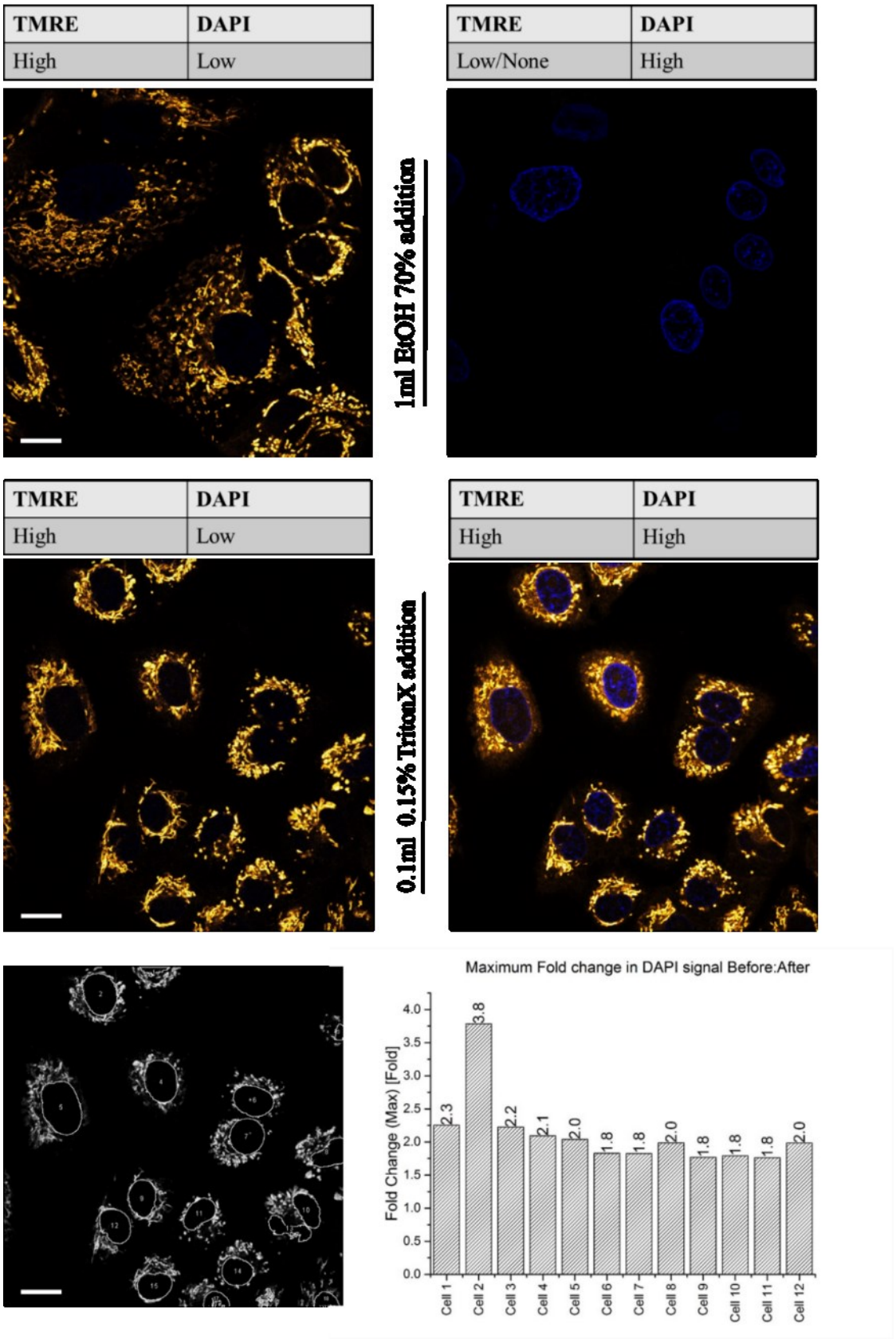

Figure.36: Experiments performed with DAPI to verify its ability to measure membrane permeability. The micrographs shows MCF7 cells stained with TMRE and with 1µM DAPI in the medium. The cells were then challenged with 70% Ethanol (first row) or Triton-X100 (second row). The third row depicts a quantification of 12 cells fold change in nuclear signal after the Triton-X100 treatment. The scale bars represent 10µm.

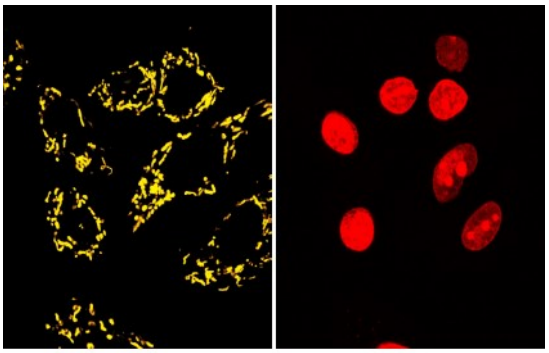

Fig.37 Test for the function of our PI containing medium cells stained with TMRE (yellow) in a medium of 1µM PI are challenged with Triton-X100. Triton-X100 destroys biological membranes allowing the PI to enter the now damaged plasma membrane. The mitochondrial signal is also lost as Triton-X100 also destroys the mitochondrial membrane.

6.4.2 Experiments investigating plasma membrane integrity

Initial experiments were performed "offline" using the confocal microscope at the Universität der Bundeswehr München under live cell conditions and using eight well Ibidi live cell imaging slides to determine how fast a PI signal could be visualized and if TMRE/PI could in fact be imaged in the same cells at the same time. Propidium iodide and TMRE have a highly overlapping Ex/Em spectrum, but their signal localization however is distinctly different. TMRE was loaded into cells as described in this work and in addition a PI was added to the imaging medium to a concentration of 1µM. The media was left on the cells during the irradiation and, in case of a change in membrane integrity, would enter the cells, intercalate with the DNA and cause a highly specific nuclear staining pattern. Experiments with PI in the medium were performed at both SNAKE and AIFIRA with different batches of PI and both A549 and MCF7 cell lines. In the short times after irradiation (up to 30 minutes), PI signals were never seen even after irradiation with very high ion numbers (>10000 protons). Initial experiments at AIFIRA with 1400 protons per point and 14000 protons per point in a 6x6 point matrix, showed no visible PI signal for up to 10 minutes (Fig.38)

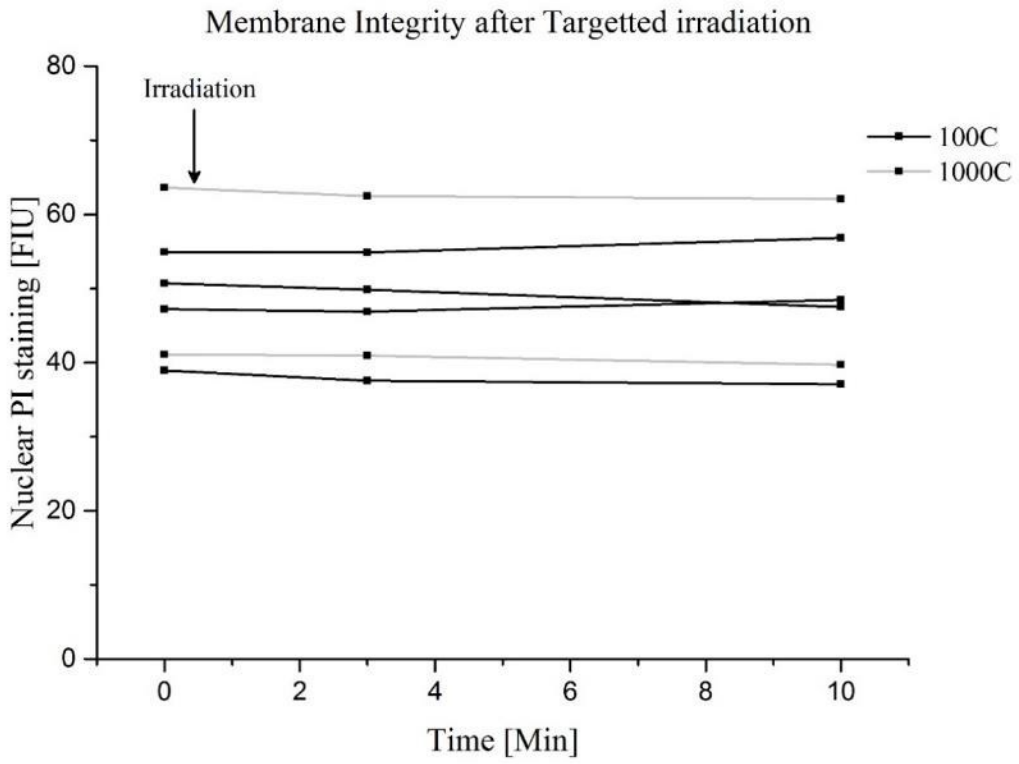

Figure.38 A quantification of nuclear specific PI staining after irradiation with 100 or 1000 carbon ions per point. The graph shows the Fluorescence intensity values from 0-10 minutes and during this time there is no visible change in PI signal.

However in the samples there were occasional cells with PI and no TMRE staining indicating that the PI was in fact in the irradiation container and working. In addition control experiments with TritonX-100 were performed to ensure that PI signal was visible after total membrane permeabilization. TritonX-100 detergent unsurprisingly induced a total loss of TMRE signal and a very rapid nuclear PI signal due to the detergent's fast acting membrane disruption (Fig.37).

Experiments performed at SNAKE made use of the AutoTarget macro to probe mitochondrial and membrane potential and plasma membrane integrity using both PI and TMRE simultaneously. The cells were loaded with both dyes and the PI was left in the sample during imaging. Irradiation was performed using 100 ions per point and cells were irradiated with a variety of different numbers of ions (10-100). As the representative images in Fig.39 show, even up to 30 minutes after irradiation with 80 ions per point, there was no sign of PI staining in the nucleus indicative of membrane integrity loss. The test however is limited to a few hours as the longer the cells remain in the container the more likely it becomes that they do not survive as they are being bombarded with light and are surrounded by PI. Therefore the experiment is only able to give a short term initial insight into membrane integrity. However similar experiments run with lasers show PI staining within 10 minutes (Jonghee et al., 2015).

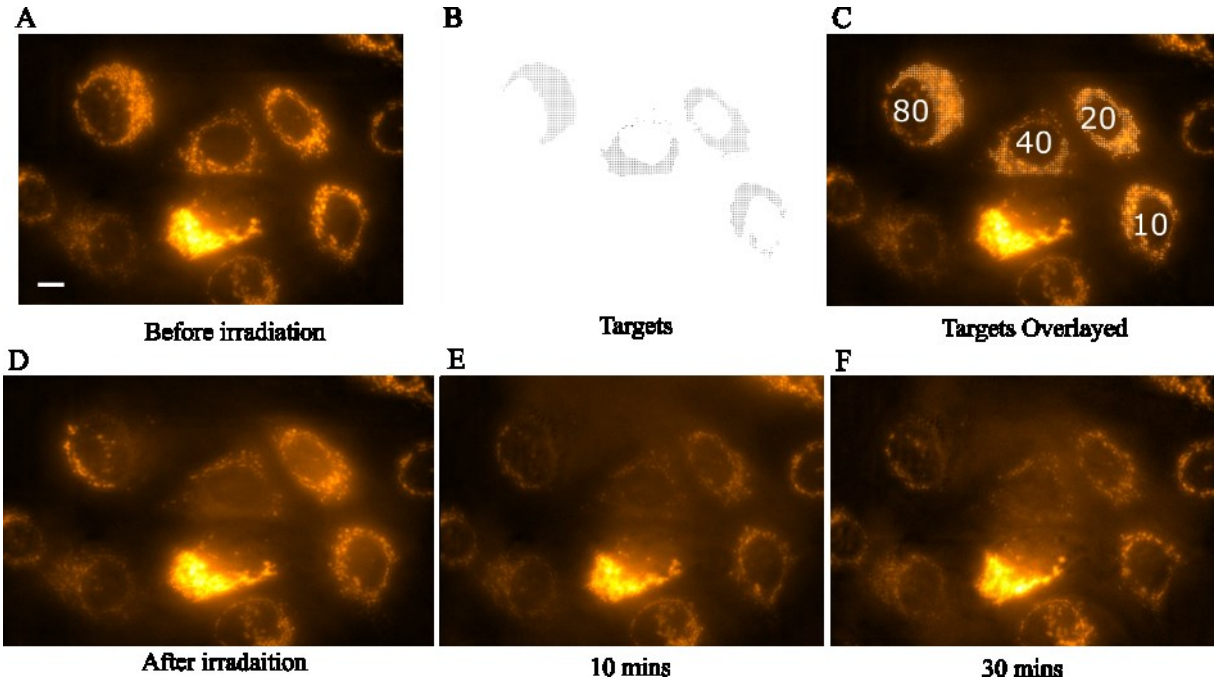

Figure.39: A series of micrographs (A-F) are shown, which depict the process of irradiation of cells stained with TMRE and irradiated using the AutoTarget macro (B) with varying ion numbers (C). The micrographs show no PI specific nuclear staining up to 30 minutes after irradiation indicating that there was no damage for these ion applications.

6.5 Reactive oxygen species: ROS

Reactive oxygen species (ROS) are chemically active oxidizing agents which can induce damage to biological samples when induced in cells. Key examples of ROS are superoxide (O_2^-), hydroxyl radicals (OH^-) and singlet oxygen. ROS interacts with water or biological matter and induces damage by transfer of electrons between the reactive oxygen species and the affected chemical or biological electron acceptor. These reactions are usually fast as primary ROS are not long-lived chemical species (range from pico to micro seconds) because they are inherently unstable and react with their surroundings. Radiation is a potent inducer of ROS, as the ionization events caused in biological matter are sufficient to induce the production of ROS species (Mikkelsen and Wardman, 2003).

Mitochondria are the major source of ROS in cells as the constant pumping of protons across the membranes using the membrane transport chain and the enzymes involved in glucose metabolism creates superoxide radicals (Murphy, 2009). Mitochondria are however very well equipped to deal with this source of intracellular stress as they possess superoxide dismutase enzymes (SOD). SOD either adds or removes an electron from superoxide to produce either molecular oxygen or H_2O_2 both of which are less damaging to the cell than superoxide (Culotta et al., 2006). When studying mitochondria and radiation induced damage, ROS production is a key factor which must be examined. When examining cells as the biological targets of ionizing radiation the majority of the matter contained within the cells is water. Therefore the likelihood of radiation interacting with water and ions dissolved in the water is high. The interaction of radiation and water leads to radiolysis which as stated above leads to the production of radicals species which then interact with the cell and cause damage which is investigated by radiation biology.

When investigating radiation induced ROS and mitochondria it is important to note that mitochondria are the most potent sources of indigenous ROS in the cell. The production of ROS by mitochondria in healthy cells is balanced, however greater imbalances in cellular ROS, such as are present in cancer cells, or as can be induced by ionizing radiation can cause problems with cell signaling and homeostasis (Sabharwal and Schumacker, 2014). There is a wealth of literature on ROS and its effects on the cell both from the mitochondria-centric literature and the radiobiology literature. In both cases ROS formation is equated to cell damage and adverse effects which have various negative outcomes for the affected cells from DNA damage to cell death (Azzam et al., 2012, Ishikawa et al., 2008, COOKE et al., 2003). Therefore being able to detect ROS in cells during irradiation is of great interest as the induction and propagation of radiation induced ROS may play a major role in the induction of the damage. Furthermore having an understanding of the radiation induced ROS produced by targeted mitochondrial irradiation could shed some light on the mitochondrial role in radiation induced damage.

6.5.2 MitoSOX

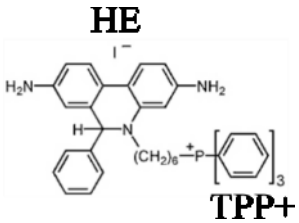

MitoSOX

MitoSOX is the most commonly used mitochondrial targeted fluorescent probe for superoxide anion detection. The probe at its core is hydroethidine (HE) with a mitochondrial targeting linker (TPP+) sequence (Mito-HE aka MitoSOX). The probe is one of the most widely used in many biological disciplines to understand the production of O_2^- after treating cells with various stressors. Fundamentally the probe functions by interacting with either O_2^- at a rate of 1.6x10^4 $Mol^{-1}s^{-1}$.(Zielonka and Kalyanaraman, 2010). As O_2^- is produced by mitochondria and ionizing radiation the aim was to detect any changes in mitochondrial O_2^- after targeted irradiation to verify if this could also be a possible reason why mitochondrial depolarization was seen after irradiation.

In this body of work MitoSOX was used to test for the production of O_2^- after targeted irradiation. MitoSOX exhibits an increased fluorescence intensity when it interacts with O_2^-, however this increase in fluorescence intensity can be caused by one of two products of MitoSOX; Mito-E^+ and Mito-E-OH. Only the latter is a product of O_2^- interaction, the Ethidium (E^+) product can be produced by a variety of other non-superoxide driven processes. To test specifically for the Mito-E-OH product imaging of the fluorescence intensity increases at both the standard excitation wavelength 488nm and with the Mito-E-OH specific 400nm excitation was performed.

Live cell imaging of O_2^- after irradiation is not a widely performed process and especially capturing the O_2^- specific signal as it is produced has not been documented before. Therefore this work is the first time that live cell imaging of superoxide induced fluorescence change after targeted irradiation has been attempted and is only possible due to real time concurrent targeted irradiation combined with epifluorescence imaging. These techniques were used to visualize radiation induced MitoSOX fluorescence signal intensity increases during irradiation.

Although HE and mito-HE (MitoSOX) are often used to determine O_2^- the results are very often misinterpreted and the conclusions drawn from the experiments are often taken at face value without assessing the caveats of the detection method (2 fluorescent products) which will be discussed in full in the discussion. The primary analysis of the data involved assessing changes in MitoSOX specific fluorescence intensity and comparison of the peaks with irradiation times, ion numbers and values before and after irradiation.

The analysis method used to assess the fluorescence intensity was largely the same as that used when assessing TMRE: automatic readout of the irradiation fields followed by profiling of the individual irradiated fields across the stack of time-lapse images. The measurement of fluorescence intensity before, during and after irradiation are presented in graphs plotted using Origin Pro.

6.5.2.1 Experiments using MitoSOX to investigate targeted irradiation induced superoxide production

Experiments performed to analyze O_2^- involved staining MCF7 cells with MitoSOX for 15 minutes at 37°C and 5% CO_2 and then washing out the remaining signal once with imaging media before imaging the cells in the LCI container online at SNAKE. The protocol for staining and washing is the same as that for TMRE apart from the varying incubation time. The experiments performed at SNAKE were performed twice on separate cells with separate staining procedures and both yielded similar results.

The fluorescence signal represented by the MitoSOX staining of the mitochondria was, at first, imaged without applying radiation to understand phototoxic effects of the illumination light on MitoSOX. Capturing images every 4.5 seconds with 100% LED illumination caused the imaged cells to exhibit a light induced phototoxic fluorescence intensity increase. The MitoSOX specific mitochondrial signal (similar to that seen in TMRE experiments) as shown in Fig.40, showed a homogenous increase in MitoSOX signal in all of the cells in the imaged area. The signal increase depicted in Fig.40 as well as the micrographs are from a representative cell in the illuminated field.

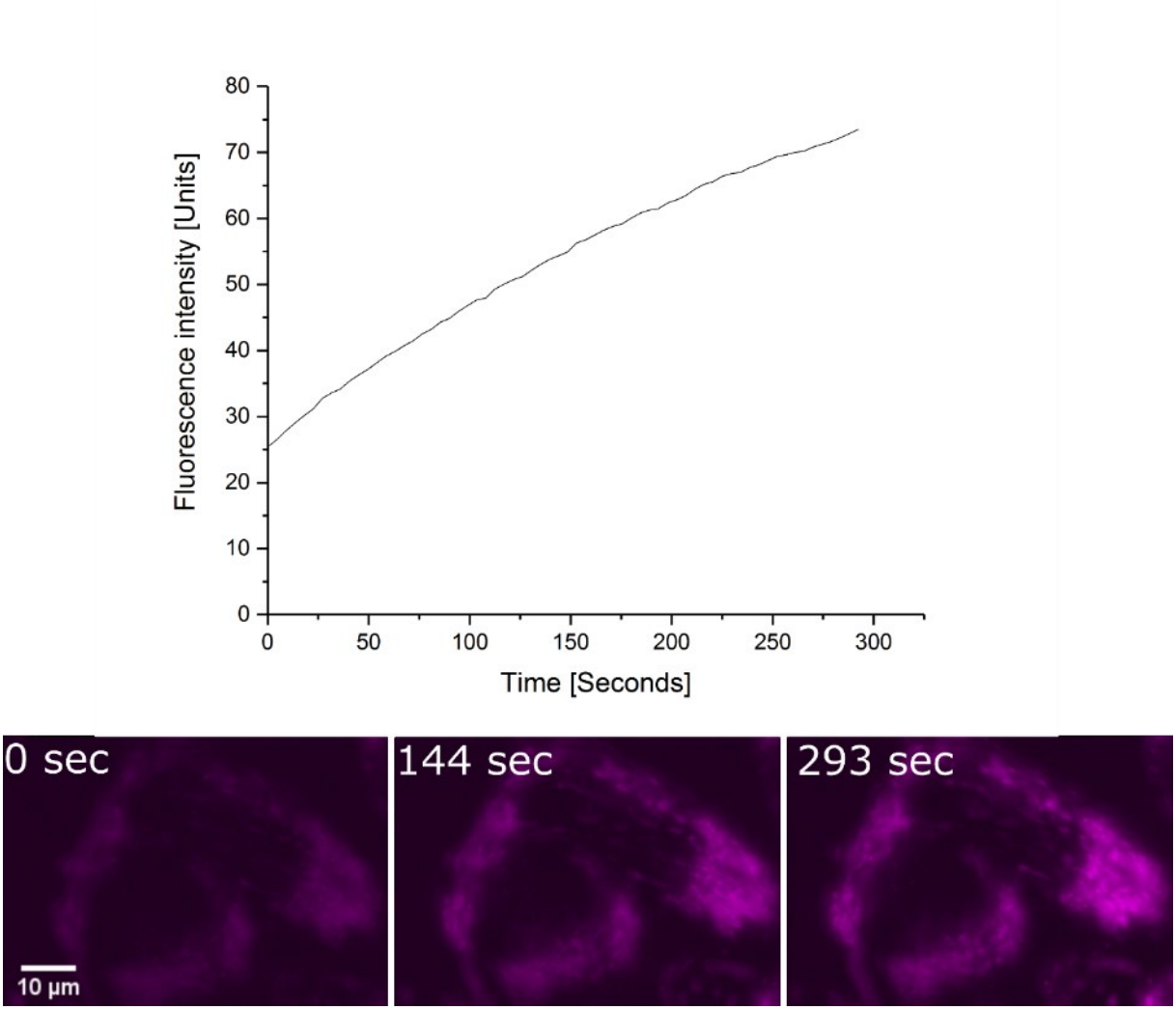

Figure.40 The figure depicts micrographs of MitoSOX stained cells and a quantification of the increase in fluorescence intensity during a light exposure experiment. The MCF7 cells stained with MitoSOX were excited with light alone to show the phototoxic effect of too much excitation light on the MitoSOX experiments. The graph (upper) shows the increase in FI over time (100% LED, 500ms exposure time) the lower images are the visual representation of the cells at the corresponding time points. The exposure of MitoSOX to too much light therefore introduces light induced photo-ROS and thus results in a false positive reading for ionizing radiation experiments since no ionizing radiation was used in these control experiments.

Decreasing the exposure time by a factor two lead to stable imaging conditions, whereby no detectable photo activation occurred. Optimizing the exposure time in this way lead to a slight imaging related photo bleaching in all time-lapse images. Photo bleaching manifested itself in such a way that all signals captured showed a slow and constant decrease over time. This photo bleaching could be corrected by background correction over the extent of the time-lapse. Once the imaging parameters were defined and shown to be working well, irradiation of the MitoSOX stained mitochondrial was performed.

Irradiation was performed using the 6x6 irradiation point matrix and the number of ions per point was varied from 1000-15. In order to perform the irradiation procedure, concurrent imaging and irradiation methods were employed which make use of a stable count rate of particles at SNAKE and defines an exposure time instead of a counted number of ions. The carbon ion numbers are therefore prone to an error of about ±25%. Initial imaging was performed in the same way that TMRE was imaged, an initial image was taken and used as an irradiation target template. After irradiation the time-lapse imaging was started and the consequences of the irradiation were analyzed over time. This did not prove to be the best strategy as the fluorescence intensity increase after irradiation was very fast and only well detectable for larger numbers of ions (125+). This severely limited this technique as it was of interest to understand not only the induction of the effect but also the outcome. To obtain such knowledge, concurrent imaging and irradiation proved to be a far more powerful method of analysis as it enabled, at least for the higher ion number, a direct visualization of the fluorescence intensity peak, from start to end. The peak for such a 6x6 irradiation point matrix irradiated with 1000 ions is depicted in Fig.41.

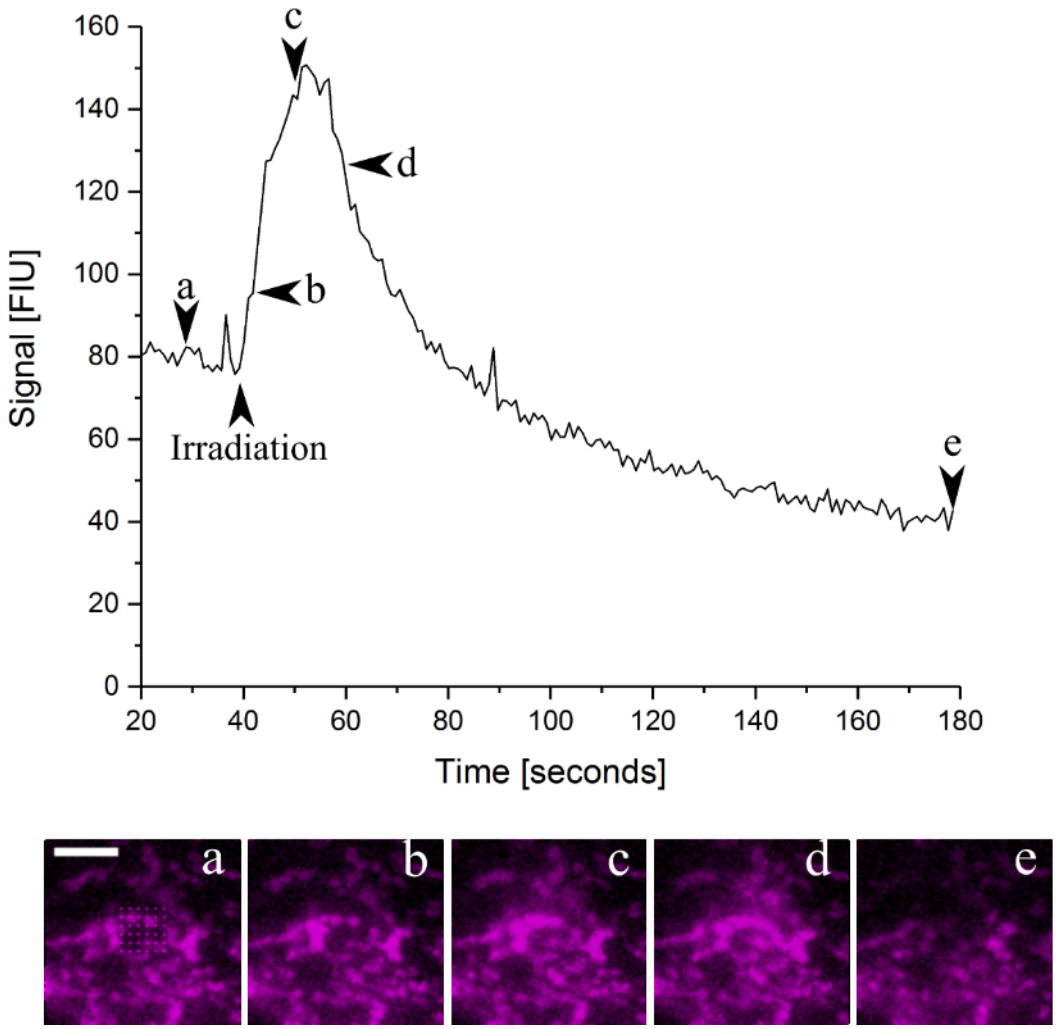

Fig.41 The figure shows a quantification of the signal intensity of the MitoSOX signal over time is depicted along with the corresponding area in question in the form of micrographs (a-e). The initial signal of MitoSOX increases to a local maximum corresponding to the signal intensity seen in the micrographs (peak at c). The figure is one of 15 such irradiation performed using 1000 ions per point. Based on a countrate of 2 kHz for this experiment the application time for the ions was ~18 seconds. The scale bare represents 10µm.

From a radiation biology perspective a whole cell application of a large number of ions, as is performed, leads to DNA damage and in cases of insufficient DNA repair eventually leads to cell death. This application of ions (15-1000) is considered very high given the constraints of cellular biology and the knowledge of cellular damage from radiation biology. However due to the lack of knowledge on organelle specific response it was necessary to further investigate the effects of targeted irradiation of mitochondria with a wide range of ion numbers. The initial results from 1000 ion application in a 6x6 matric looked very promising as an instantaneous reaction of the MitoSOX dye to the superoxide produced by the ions vas visible (Fig.41). A step by step reduction of applied number of ions was conducted to investigate the extent of the effect seen. Given a count rate of 2 kHz ±20%, (which was verified at several intervals during the experiments) it was possible to reduce the applied number of ions, in a step-by-step fashion by changing the application time. Using count rate application of ions concurrent imaging and irradiation was possible however at the cost of a 20% error with regard to the ion number. While irradiation with 1000 ions per point yielded a well-defined and very prominent peak, lower ion numbers yielded less pronounced MitoSOX peaks. For each of the experiments 15-20 cells were targeted and analyzed for each ion number applied making sure to leave some cells in the field of view as non-irradiated controls. Since the initial fluorescence intensity of the stained mitochondria varied and the size of the effect decreased the fewer ions were applied, parameters like absolute peak height were not ideal. To compare the peaks a ratio of the peak of the signal to starting value before the irradiation was calculated and plotted on the same graph (Fig.42). The smallest number of ions required to visualize an effect using our imaging system was 125 carbon ions. Below 125 ions the peaks were not very pronounced and the imaging time for one frame was higher than the irradiation time so the effects could have been missed completely.

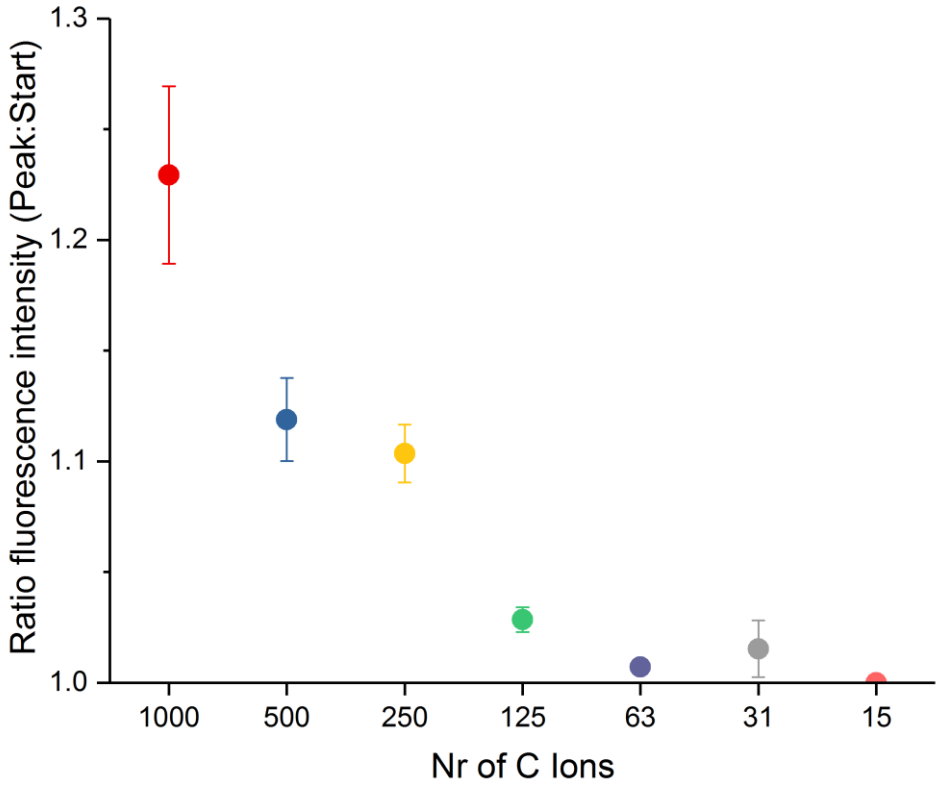

Figure.42: The ratio of the fluorescence intensity from the peak of the MitoSOX curve after irradiation to the start (baseline) of the reading for each number of ions applied from 1000-15 ions per point in a 6x6 matrix is shown. The error bars represent the standard error of the mean for 20 analyzed cells. The graph shows a high ratio value for 1000, 500 and 250 however at 125 and below the signal was very weak and for most values below 63 ions not detectable.

The ratio of peak to start signal intensity was able to shed some light on the range of the ROS induced effect. The intensity of the probe (MitoSOX) just before induction of fluorescent signal increase (start) and the peak value during irradiation (peak) were measured from the micrographs and used to calculate the peak:start ratio. A value of 1.0 indicates no difference between peak and start and therefore no detectable effect, any significant value higher than this demonstrates a detectable effect.

The peak to start values showed that at 1000 ions per point there was a distinct peak showing a strong effect of irradiation on the probe. When the number of ions was reduced to 500, there was a considerably less strong, but still detectable signal. When 250 ions were applied, the drop was far less severe than from 1000 to 500 ions in fact the value was rather comparable to that of the 500 ion irradiation. 125 ions per point was the value at which all of the irradiated areas still showed a change in signal; then below 125 ions the effect was only marginally detectable. For the case of 31 ion application per point, all but one irradiation areas showed no response to the irradiation. The 15 ion application case showed no visible response.

Furthermore it was possible to compare the time required to irradiate the 6x6 irradiation field with the signal peak rise time. When applying 1000 ions in a 6x6 matrix, a total of 36000 ions were applied to the targeted mitochondria at a rate of 2 kHz. The application of all 36000 ions to a single 6x6 matrix would take on average 18 seconds at the measured count rate. The average rise time for 1000 ions of the MitoSOX fluorescence signal as measured from the initial point at which the signal started to the peak was calculated from measurements for 15 cells to be 17.1s with a standard deviation of 3.1s. This time indicates that the signal intensity increase, as shown in the representative graph (Fig.43) and the measured values in the experiments overlap well with the time required to irradiate each targeted area. The hypothesis is therefore that the increase in MitoSOX signal is directly related to the time required to irradiate the area of interest. Therefore the measurement shows that there is a fluorescence intensity increase in relation to the radiation induced O_2^- production. The time required to apply sufficient amounts of carbon ions to each 6x6 matrix for ion numbers from 1000-62.5 aligns well with the average measured rise time.

The capability to measure the responses at lower ion numbers (below 62.5, for a 6x6 matrix) were severely limited, as it is possible that low ion numbers induce only very short duration of the effects with a small magnitude which could not be captured using our current microscopy equipment. The exposure time used in the experiments was relatively large (>1.5s) as it was important to obtain enough signal to analyze. In Fig.43 the graphs below 62.5 ions are not shown as there were no detectable MitoSOX related fluorescence peaks. The further optimization of the staining procedure and microscopy conditions could well lead to a better yield of signal intensity and therefore reduce the exposure time and, in turn, allow for a faster framerate.

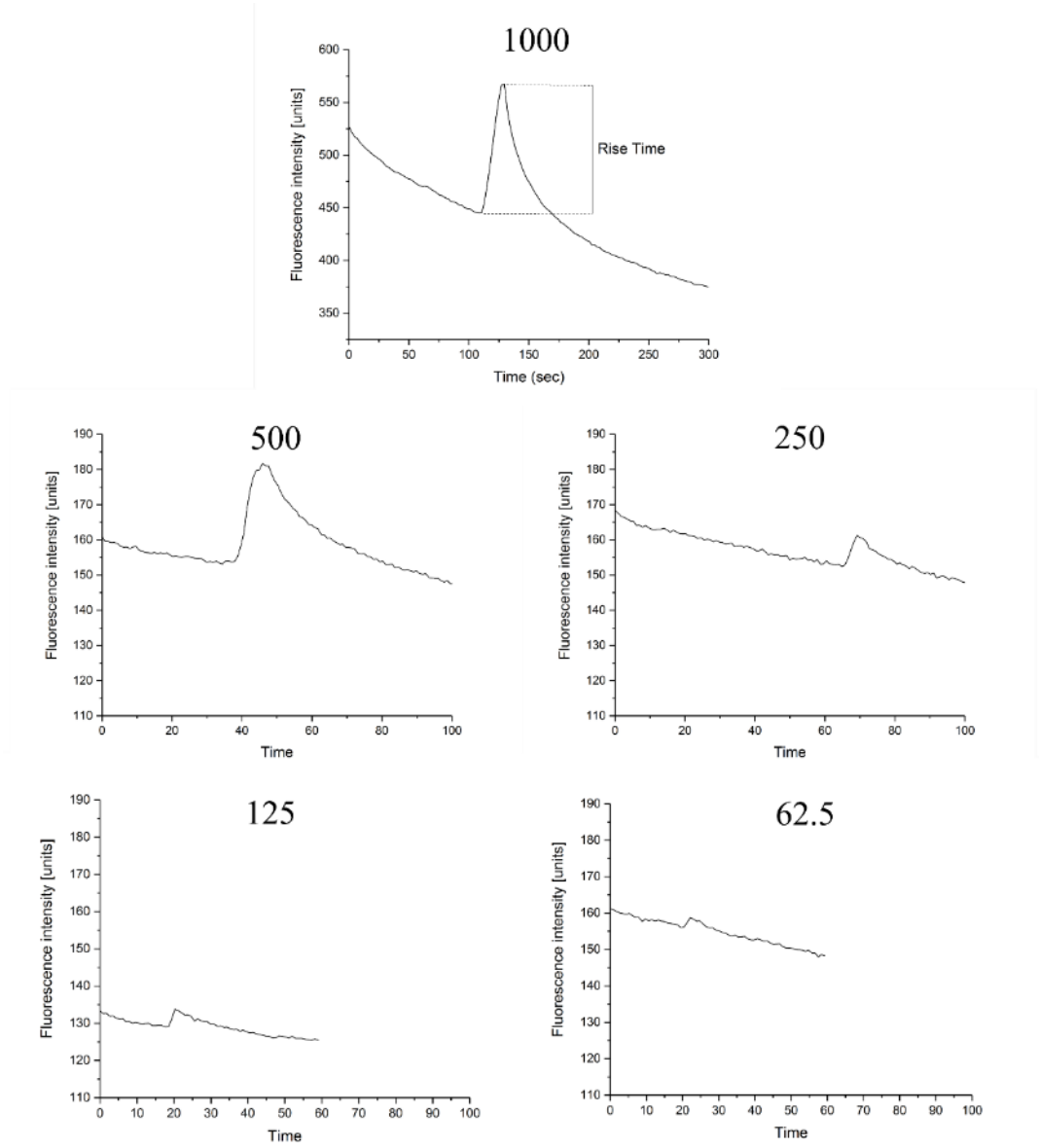

Ion number	Time to irradiate 6x6 (s)	Average measured peak rise time (s)	SD
2000 ± 200	18	17.100	3.064
500 ± 100	9	7.686	1.175
250 ± 50	4.5	4.500	0.559
125 ± 25	2.25	2.232	0.440
62.5 ± 12.5	1.125	1.109	0.396

Figure.43 Representative graphs for radiation induced MitoSOX peaks with the ion number per point above each graph. The upper plot shows how the peak rises and falls following irradiation. The table (lower) summarizes the time required to irradiate each 6x6 field based on the carbon ion count rate from the accelerator at SNAKE along with the average measured rise time (baseline to peak) and Standard Deviation (SD) for 15 cells.

6.5.3 roGFP2 a genetic biosensor to measure redox potential

6.5.3.1 Detection Method: Mito-roGFP2

There are many methods for measuring the production of reactive oxygen species after irradiation. The most commonly used methods are based around commercially available ROS sensitive fluorometric assays which rely on a change in fluorescence intensity corresponding to ROS increase based around a reaction of ROS with the fluorescent probe. Examples of such probes are DCFH-DA for measuring intracellular H_2O_2, dihydroethidium and MitoSOX for detection of intracellular $O_2^{\circ-}$ and dihydrorhodamine for measuring $ONOO^-$ (Kalyanaraman et al., 2012a, Woolley et al., 2013). All of these fluorescent probes have their own set of highly specific experimental requirements to ensure that the readout really represents a change in ROS and not a false positive signal. The problems with such probes have been documented in the literature (Kalyanaraman et al., 2012a, Benov et al., 1998). A new generation of probes such as Spin trap probes (Dikalov et al., 2011) and Boronate deprotection fluorescent probes (Miller et al., 2005) have been under development; however these have not yet become as widespread as the last generation of ROS probes.

In the light of the difficulty of measuring highly localized ROS after irradiation, specifically under highly controlled conditions such as are required for the above fluorophores another approach was taken. RoGFP2 is a genetically encoded glutathione redox potential biosensor first developed in 2004 by Dooley et al. (Dooley et al., 2004). This probe can further be attached to organelles of interest, such as mitochondria (mito-roGFP), for the highly specific localized measurement of the glutathione redox potential in the targeted organelles (Gutscher et al., 2008, Vevea et al., 2013). A derivative of roGFP2 targeted to mitochondria by a cytochrome oxidase complex IV tag was therefore chosen for analysis of changes in the redox potential after irradiation. The construct for the genetically encoded biosensor (Addgene: 49437) was transfected into U2OS cells using Viromer red transfection reagent (Lipocalyx) by Hervé Seznec and his group at the CENBG Bordeaux. The transfection efficiency was 95% or higher for all experiments.

The roGFP2 probe is a dual excitation ratiometric fluorescent probe which is excitable at 400nm and 480nm with a fixed emission maximum at 520nm. The excitation maxima shifts depending on the oxidation state of the probe. The oxidation state and therefore the excitation state depends upon two key cysteine residues within the GFP protein. In the reduced state the residues form a di-sulphide bond, and when the residues are oxidized, the di-sulphide bond is lost (Remington, 2011). The emission intensity measured at 520nm for an excitation at 400nm and 470nm forms the ratio of 400:470nm which defines the oxidation state of the probe. A ratio of 0.1 indicates that the probe is reduced and ranges up to 0.8 if the probe is oxidized. In cultured cells without any intervention, the probe tends towards the oxidized state. Initial experiments at the beamline showed this. However recalibrating the probe to a more reduced state is possible by the addition of 100-200µM β-mercapto-ethanol. Experiments with the cell lines performed between beam times in Munich showed that the probe can efficiently be reduced by addition of β-mercapto-ethanol into cultured cells (Fig.46).

6.5.3.2 Imaging requirements for roGFP2 ratiometric imaging

The imaging of ratiometric biosensors, such as roGFP2, requires a particular microscope setup. Most experimental setups employ two filter cubes with the same emission filter (520nm) and varying excitation filters (400nm, 470nm). This setup requires a fast and highly accurate filter cube wheel which is capable of changing rapidly between filters, enabling a fast image acquisition. The setup chosen for SNAKE however diverged slightly from this "standard" setup for epiflouresence microscopy. As the Zeiss Axiovert microscope used at SNAKE does not have a particularly fast filter cube changer and constant movement of the changer could lead to overall vibrations which would interfere with ion beam targeting, an alternative method employing a single filter cube and multiple light sources was employed.

A custom Filter cube was designed and crafted by CHROMA Technologies for this purpose. The filter cube (Figs.44, 45) enabled excitation via two Zeiss Colibri LED units with 470nm and 400nm as well as an emission at 520nm. The Zeiss Colibri LED light sources were introduced into the Colibri and a 425nm beam combiner (Zeiss) was used

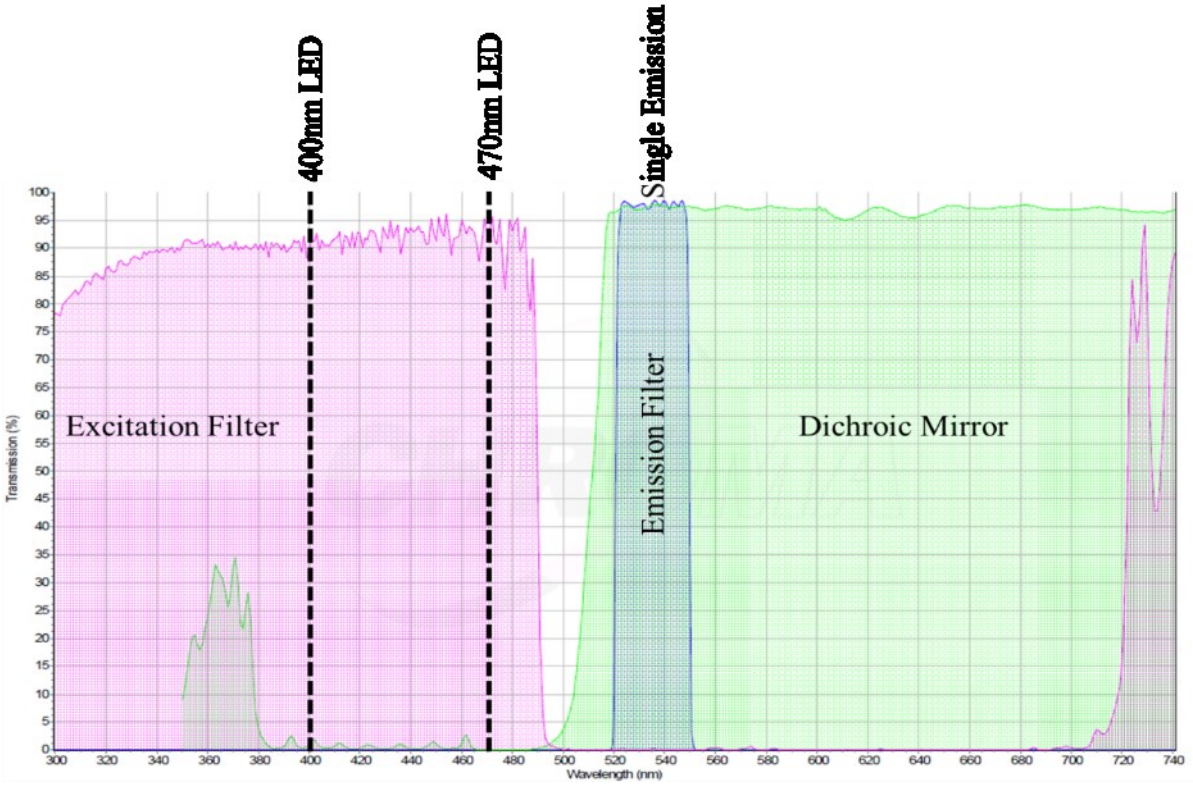

Fig.44 The transmission and wavelength graph for the custom Chroma filter cube along with markers for the 400nm and 470nm excitation LEDs and the single emission filter. This custom filter was used for roGFP2 experiments at Bordeaux. Graph was adapted from the Delivered materials from CHROMA Technologies.

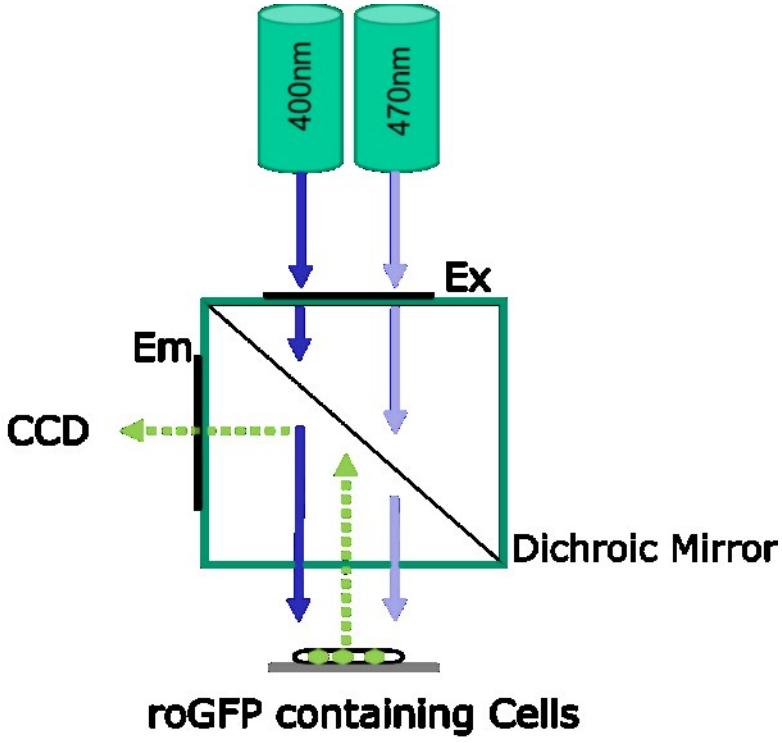

Figure.45 Overview of the excitation/emission system for the imaging of the roGFP2 cells at SNAKE and AIFIRA (upper). The system is based around dual excitation with individual excitation LEDs and a custom filter cube (lower) which filters the single emission wavelength back to the CCD. Filter cube components: Excitation filter: ET490SO; Emission filter ET 535/30; Dichroic mirror T510lpxrxt.

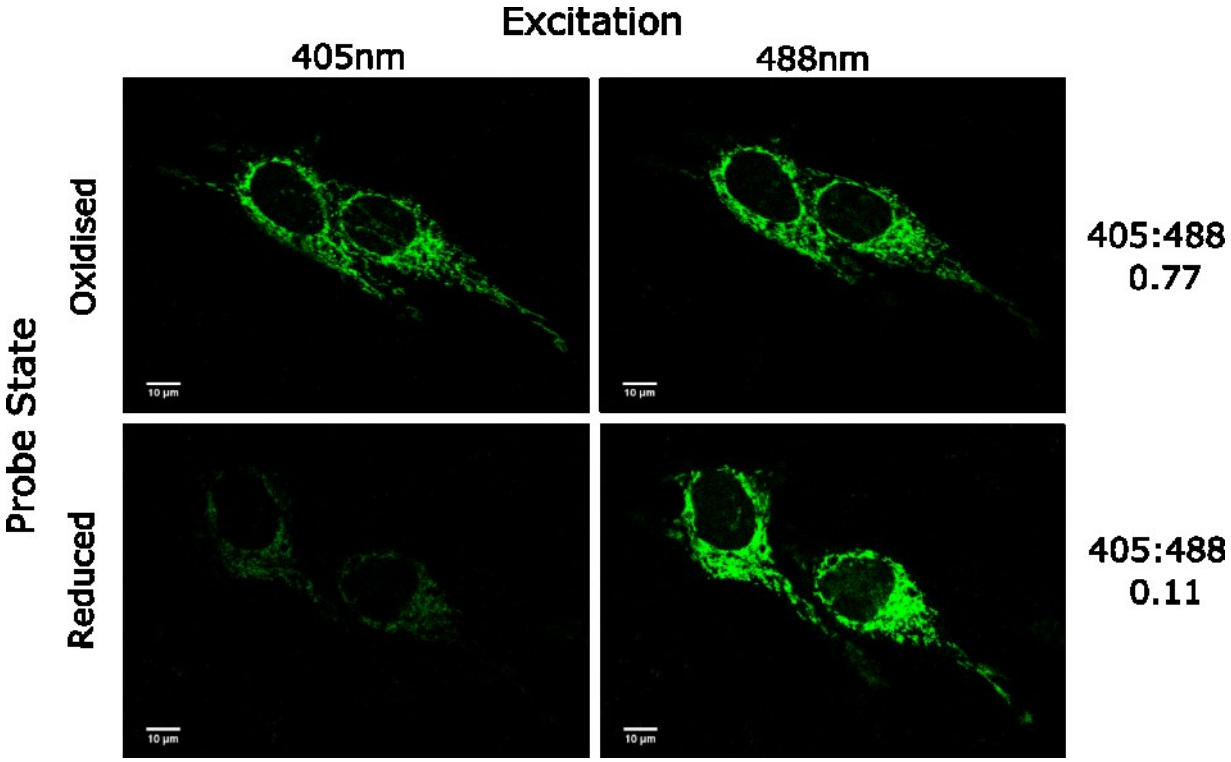

Fig.46 The micrograph shows two cells for each probe state; oxidized (upper) and reduced (lower). The oxidized state shows a relatively equal fluorescence intensity signal and a 405:488 ratio of 0.77 which indicates that the probe in its natural state is already oxidized. After addition of 2-mercaptoethanol, the system can be reduced in which case it shows a decreased 405nm signal and a stronger 488nm signal changing the ratio to 0.11 which indicates a reduced state.

6.5.3.3 roGFP2 as a probe for IMS integrity

In addition to being a potential redox probe, roGFP2, which in our experimental system is linked to cytochrome-c-oxidase subunit, can be used to test if changes in the IMS have occurred. Cytochrome-c-oxidase subunit is present in the IMS of the mitochondria and the protein of interest is attached to the target, therefore any change to the distribution of the targeted protein would be detectable. The GFP signal perturbations or changes in signal structure/intensity could be interpreted as a change in the constituents of the IMS. Since radiation is known to be a major damage inducing agent, changes to the structure of mitochondria which could lead to a change of fluorescent probe distribution are not out of the question. The roGFP2 probe therefore serves a double purpose as a glutathione redox potential measuring system and as an integrity marker for the mitochondrial IMS. This system was therefore used as a secondary marker for mitochondrial inner membrane integrity.

6.5.3.4 Experiments

Mito-roGFP2 tagged U2OS cells were tested in two beam times in Bordeaux with targeted proton irradiation. The aim was to use the Mito-roGFP2 targeted to cytochrome c oxidase subunit IV to understand if there were any changes to the glutathione redox reaction state and, in addition, to use it as a genetically encoded marker for IMS integrity. Changes in distribution or intensity of the GFP signal may indicate changes to the IMS following irradiation. After plating U2OS cells on the imaging container at AIFIRA and allowing them to adhere overnight, the medium was changed for pre-warmed media before irradiation. The sample was loaded into the microscope and imaged using the Chroma filtercube and dual LED setup above. The irradiation of cells expressing roGFP2 in mitochondria was followed by imaging every 300ms using both wavelengths 400nm and 470nm. When looking at the probe with respect to its information about IMS integrity, the results showed no change in localized signal intensity or structure of the probe. The results as shown by a representative cell micrographs in Fig.47 indicate no change in overall intensity or structure even after irradiation with a 6x6 matrix with 7000 protons per point (equivalent to 200 carbon ions per point)

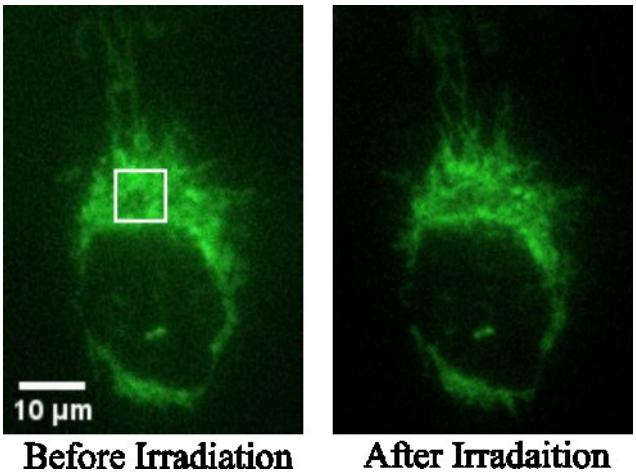

Fig.47 The micrographs show U2OS cells expressing roGFP2 before and after irradiation at AIFIRA. The white box marks the point of irradiation using a 6x6 matrix of 7000 protons per point.

6.5.3.5 Glutathione Redox Potential

The Initial measurement of the U2OS tagged cells with the ratiometric imaging approach indicated no change in irradiated vs unirradiated sample cells (Fig.48). The ratio of the fluorescence intensity of the emission wavelength 520nm was measured for excitation at 400 and 470nm and a ratio of signal 470:400nm calculated. For this particular probe the range of values extended from 0.1 when the probe is fully reduced, to 0.6, when the probe is oxidized. The initial ratio of unirradiated cells was ~0.47. After irradiation of cells with 3500 protons per point there was no visible change over 10 minutes when imaging every 300ms for a total imaging time of 200 seconds. The results indicated that the probe was already nearly fully oxidized and showed no increased oxidation after irradiation.

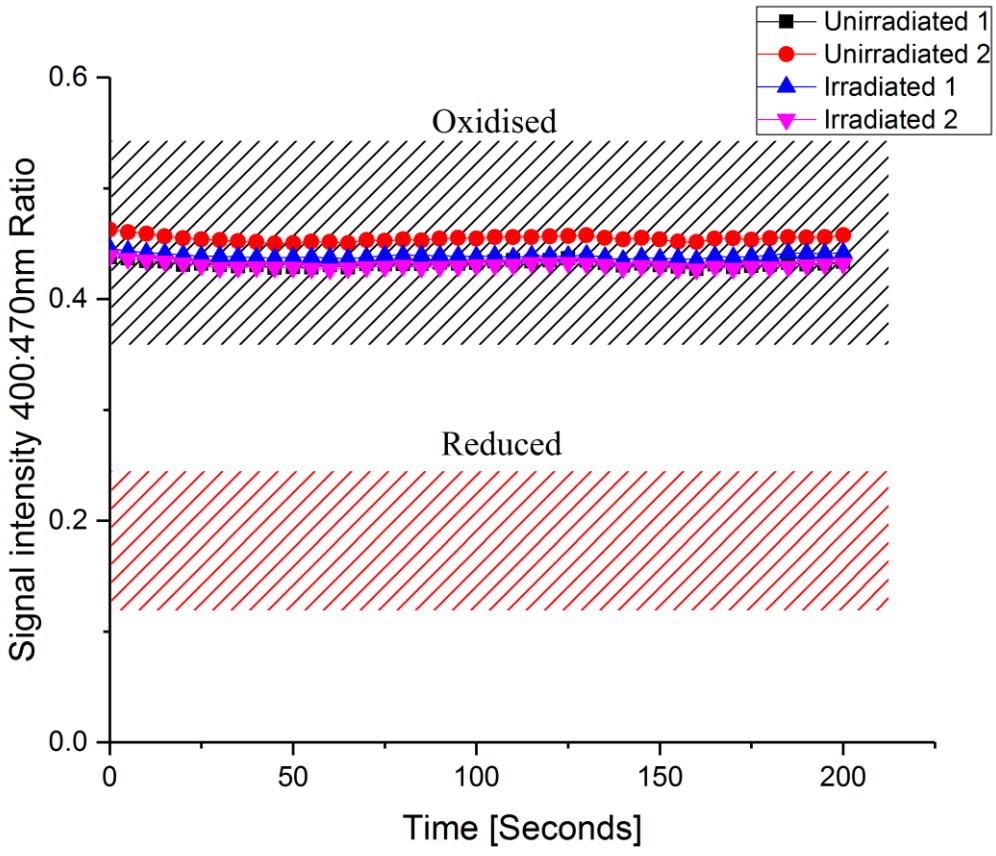

Fig.48 Graphical representation of the signal intensity ratio of 400:470nm excitation for two irradiated and 2 unirradiated areas of roGFP2 expressing mitochondria showing the change of signal intensity ratio over time. The samples ratios indicate a relatively oxidized state and no visible radiation induced effect.

The repeat experiment was performed a second time at AIFIRA in December 2015 with the same U2OS cell line, this time defrosted one week before experiments. The experimental setup was slightly different as another, faster, EmCCD camera was used for acquisition and the cells were treated with dithioltheritol (DTT) before irradiation to reduce the probe. The detection was performed using an Rolera EM-C2 EM-CCD (Q Imaging) camera with a faster framerate and 16bit image depth. Since the probe showed a totally oxidized state when linked to mitochondria in U2OS cells, it was necessary to reduce the probe before the experiment. 1μM DTT was added to the medium before irradiation for 30 minutes and then removed again in order to reduce the roGFP2 probe. The aim was to capture fast perturbations in redox state during the irradiation process using a reduced probe and a faster camera.

The repeat experiment was set up with a 6x6 irradiation matrix used to apply 7000 protons per point to mitochondria tagged with roGFP2. The resulting change was monitored for 10 minutes post irradiation. When analyzing the results, the irradiated and the unirradiated cells show no difference in their signals. The irradiation was performed in the first 10 seconds. Although all of the signals in the analyzed field (Fig.49) showed an overall more reduced phenotype due to the DTT treatment, there was no radiation specific effect seen. Overall it seems that either the light is inducing the slow change in signal towards the oxidized state or that the probe has a natural propensity to the oxidized state within cells. There was however no sign of a radiation induced effect as seen in the MitoSOX data. The inherent lack of radiation induced signal could either be due to the fast activity of mitochondrial SOD or the lack of sensitivity of the probe to detect radiation induced superoxide bursts and consequent changes in redox state.

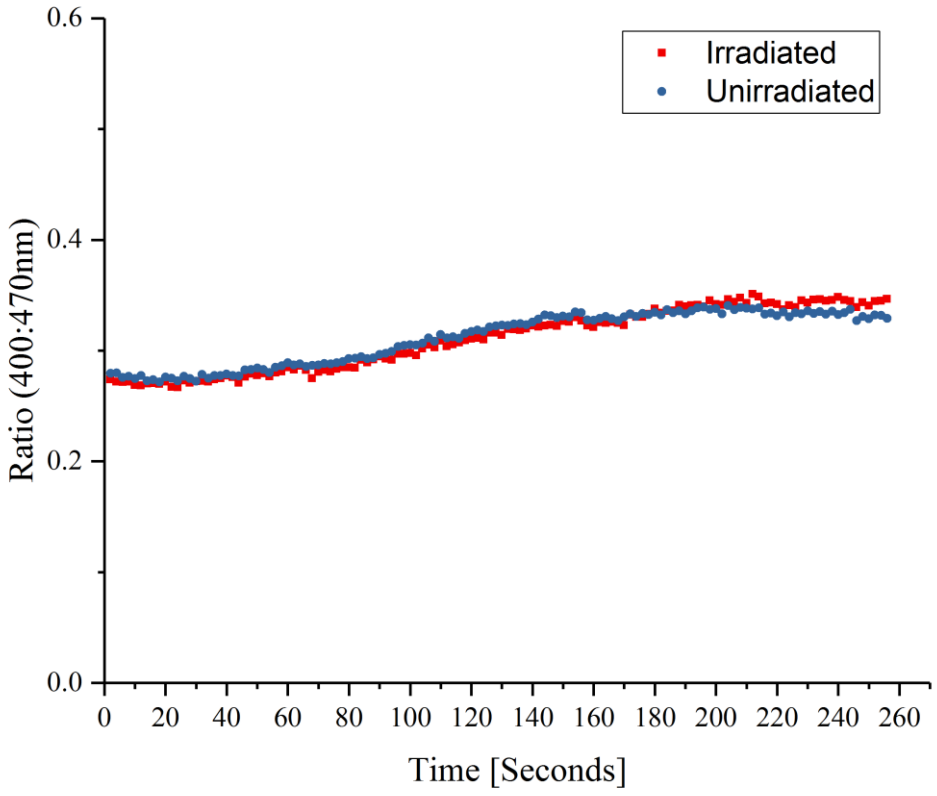

Fig.49. Measurement of the signal intensity ratio of the response of roGFP2 to ionizing radiation in irradiated and unirradiated mitochondrial clusters. Images were captured every 2 seconds and the signal of emission (520nm) after varying the excitation wavelengths (400,470nm) was assessed.

Although there were no visible changes in the signal intensity ratio 400:470nm ratiometric readout of the probe indicating a change in redox state of the roGFP2 probe, the probe was able to be used for membrane integrity analysis. Due to its location, roGFP2 was used as a marker for the integrity of the IMS. There was no change in signal intensity or GFP signal distribution of either of the probes wavelengths after targeted irradiation. The lack of change would indicate that there was no change in the integrity of the IMS either.

roGFP2 may well be an excellent marker for detecting changes in redox state induced by chemical oxidizing or reducing agents. However when challenging cells encoded with roGFP2 with short burst of ionizing radiation no changes were detected. It is highly likely that the amount of ROS produced either dissipates too fast or is converted by SOD, so that not enough of the radiation induced ROS interacts with the cysteine residues in the roGFP protein barrel to change the di-sulphide bond and therefore its conformation. RoGFP2 is therefore not an ideal candidate for this form of experimentation, however the sensitivity of the probe could potentially be further improved to detect ionizing radiation induced ROS.

6.6 Overview of experiments performed

The Table below provides an overview of the experiments performed, the responses seen in the irradiated cells, the doses at which these events were seen and the extent of the response

Experiment		Carbon			Dose	Protons			Dose
Mitochondrial membrane potential	**Effect**	**Total**	**Partial**	**None**		**Total**	**Partial**	**None**	
Targeted irradiation and imaging of mitochondria stained with TMRE (MCF7, A549 cells)	Extent of depolarization of targeted mitochondria (Loss of Specific mitochondrial signal)	X			13.9 kGy	X			13.9 kGy
			X		8.7 kGy		X		6.9 kGy
				X	Below 1.7 kGy			X	Below 1.7 kGy
Mitochondrial membrane integrity	**Effect**	**Change in intensity**	**No Change**			**Change in intensity**	**No Change**		
Targeted irradiation of MitoTracker Green labelled mitochondrial membranes	Change in signal intensity after irradiation		X		up to 17 kGy		X		up to 17 kGy
						X			Above 170 kGy
Plasma membrane integrity	**Effect**	**Signal**	**No Signal**			**Signal**	**No Signal**		
Targeted irradiation of mitochondria labelled with TMRE in medium containing 1uM Propidium iodide for membrane integrity test	Nuclear specific PI signal as measured after 30 minutes		X		up to 170 kGy ions		X		up to 170 kGy ions
Superoxide imaging	**Effect**	**Signal**	**No Signal**			**Signal**	**No Signal**		
Targeted irradiation of cells stained with MitoSOX. Intensity increases in response to superoxide	Imagaing of superoxide bursts during irradiation (live cell)	X			Above 5.5 kGy	No Data			
			X		Below 5.5 KGy				
Glutathione redox potential imaging	**Effect**	**Increased ratio**		**No change**		**Increased ratio**		**No change**	
Targeted irradiation of the roGFP2 live cell construct in mitochondria. Ratiometric imaging shows a change in excitation:emission ratio upon oxidation of the probe	ratiometric Imaging of roGFP2 construct in U2OS cells after and during irradiation	No Data						x	up to 348 kGy

Page Intentionally Left Empty

7 Discussion

In this section the results from the experiments conducted in this thesis will be discussed in context with the literature on mitochondria, radiation and laser experiments.

7.2 Depolarization TMRE experiments

Mitochondrial membrane potential was the central mitochondrial trait to be analyzed during the course of this thesis. The membrane potential of mitochondria is an indicator of function and was a simple on/off readout which could be visualized very quickly and has been utilized since 1988 (Ehrenberg et al., 1988). Recent studies using stimulated emission depletion (STED) super resolution microscopy have unequivocally localized TMRE signal to the inner mitochondrial membrane and not the mitochondrial matrix or the outer membrane (Ishigaki et al., 2016). This finding indicates that TMRE which accumulates on the IMM border in relation to the charge built up in the mitochondrial matrix is due to the electron transport chain. As the readout of signal from TMRE is highly dependent on the charged state of the IMM, minor perturbations in the membrane potential can be visualized after a stress has been inflicted on a cell.

The mitochondrial response caused by ionizing radiation, reported in this thesis was however rather unexpected as only the targeted areas depolarized leaving all untargeted mitochondria unchanged. To induce this effect, at first huge numbers (several 1000) of ions per point were used and as there is no direct literature reference for the relative radiation sensitivity of mitochondria this relatively large number of ions required to induce an effect in mitochondria is not unexpected. The extent of the depolarization seen was however less surprising. In 1988 Amchenkova et al. from Russia, using lasers to irradiate mitochondrial in cardiomyocytes showed that when only a subsection of mitochondria were targeted the whole connected network of mitochondria depolarized (Amchenkova et al., 1988). The results were described as a bleaching of the dye and not depolarization, this result however matches very well with the findings of this thesis which show “out of field” depolarizations of mitochondria which are connected to the area of irradiation (Figs.20, 21). In the 1988 paper there was no proposed cause for this “bleaching” (depolarization), though the experiments described that the laser light is absorbed by the Rhodamine staining and therefore causes damage (Amchenkova et al., 1988). We have been able to verify that the depolarization process is in fact biological and not bleaching, and that the mitochondrial and plasma membranes show no visible damage. However we now know that the membrane potential breakdown is dependent on how much energy is deposited into a single mitochondria. This 1988 paper was however by no means the first to investigate the mitochondrial response to laser irradiation. A seminal paper from 1972 (Berns et al.) showed the first laser irradiation of mitochondria using a 442nm Argon laser. This was followed by Rhodamine 123 experiments with laser irradiation in 1982 (Siemens et al., 1982). Some of the responses seen in these papers closely mirror those found in this thesis. The similarity between the response of mitochondria to lasers and ions is however unsurprising as it shows that both methods of damage have the same overall biological effect. The laser

papers did not go into further detail on modulating the energy or pulse length of the laser so we do not know if the required energy was relatively high or low compared to the energy deposited by ions. This still means that the amount of energy required to disrupt the mitochondrial membrane potential remains unclear. In comparison to all of the original work using lasers the experiments using ions has enabled a more precise quantification of the energy required to induce a biological effect on mitochondria.

The work presented in this thesis dedicated experimental beam times to further understanding the energy threshold of this phenomenon. The further the mitochondrial depolarization response was analyzed using the SNAKE and AIFIRA beamlines the more precisely the radiation induced depolarization effect could be quantified. The ability to use two separate beamlines and laboratories strengthened the experimental data by verifying that the depolarization seen was an effect of total energy deposited and not on the specific particles used and their specific LET. Only when applying the same total energy at both SNAKE and AIFIRA were the effects seen. The depolarization effect was identified with lower numbers of ions and was reduced so far, until no simple irreversible depolarization was seen (Fig.29) after irradiation. The initial amount of ions used (1000) to induce a depolarization effect proved to be more than a factor 10 more than was necessary to induce a total effect, which was seen around 80 carbon ions (in the 6x6 matrix, 13.9 kGy, $1.6x10^{-10}$ Joule). Some partial depolarizations and or flickering effects were captured after low ion number (<50 ions, $1.01x10^{-10}$ Joule) application. These effects were seen in the range of 50-10 carbon ions or protons with equivalent energy per irradiation point. The partial effect was classified as an initial depolarization event with post irradiation fluorescence not returning to starting levels. The effect suggests that mitochondria have a mechanism of coping with being challenged with the amount of energy as deposited by such a “small” number of ions. It may well be that short term damage to membranes, which in turn would lead to depolarization is repaired due to membrane realignment and shutting of the holes. Larger number of ions sufficient enough to induce a direct and total depolarization may pose an irreparable source of damage to the targeted mitochondria. In comparison, only partially damaged mitochondria could regenerate their membrane potential and reverse the effect caused by the irradiation, in some cases however not quite to the pre-irradiation level. The possible damage types caused by ionizing radiation range from membrane lipid peroxidation (Yalinkilic and Enginar, 2008), to physical membrane damage inducing channel formation (Stark, 1991). In the case of membrane damage, the possibility of only partially damaged mitochondrial membranes rebuilding/reconnecting was high as membrane fluidity and chemistry is such that smaller holes in membranes do not usually stay open for long periods of time unless the damaging agent is still present. The mitochondria which show an irreversible depolarization may have received a level of damage which cannot be repaired within the timescale of the experiments and therefore the membrane polarization will not return back to the levels before irradiation.

Localized loss of signal after irradiation was in line with the hypothesis that radiation could in fact induce depolarization (Leach et al., 2001). To actually verify that the loss of mitochondria specific signal was a biological effect and not a highly localized dye destruction took further experimentation TMRE as a cationic fluorophore only accumulates within charged regions and therefore measuring a redistribution of TMRE from point-like mitochondrial signal to increased homogenous background would be a good indication that the

dye was not destroyed but released from the depolarized mitochondria. The experiments performed initially with smaller matrices (6x6) did not release enough dye to visualize a homogenous background increase of TMRE signal inside the cell, or the TMRE redistributed within the cell too fast to be visualized. Only when larger areas or all mitochondria (Fig.23) were targeted was such a background increase seen. This was evidence for a biological depolarization effect as a highly localized destruction of the dye would not have been followed by a TMRE redistribution. The TMRE released from the depolarized mitochondria was then further taken up into neighboring mitochondria due to the now perturbed equilibrium of TMRE between the cytoplasm and the mitochondria. The relocalization of TMRE (Fig.21) indicates that the mitochondria in the region flanking the irradiated region now absorb more TMRE as this has become available and therefore seem brighter. When comparing peak height before depolarization, it is visible that the more TMRE is released into the cytoplasm the more the peak height increases before depolarization (Fig.24). This highly dynamic redistribution of TMRE is at the core of the evidence provided that this effect is in fact biological and not just a destruction of the dye.

In order to ensure that there was no difference between the function of mitochondria in cancerous and non-cancerous cell lines umbilical cord endothelial cells (EA.Hy.926) were tested as a “normal” control cell line. The experiments showed no difference in the depolarization response after targeted irradiation: all the targeted mitochondria depolarized. The depolarization response therefore seemed to be related to the energy deposited in the mitochondria and not to some cancer-specific biological response of the mitochondria. This is interesting as it shows that even if mitochondria function differently in normal cells as compared to cancer cell lines, the effect of ionizing radiation is the same. In both cases the effects seen are only visible when a large amount of energy (kGy range) is deposited in the targeted area. The overall response of a cell to the same amount of energy deposited into the nucleus would undoubtedly be cell death, by which mechanism and how quickly this would happen is however unclear as the cells are not directly destroyed by ionizing radiation alone.

7.3 Mitotracker green

MitoTracker green is a polarization insensitive mitochondrial dye which preferentially stains structures in the OMM (Keij et al., 2000, Ishigaki et al., 2016). Having an outer mitochondrial membrane stain, which was insensitive to the mitochondrial polarization state, enabled an analysis of membrane integrity after irradiation, irrespective of depolarization. The irradiation of mitochondria stained with MTG showed no change in fluorescence intensity when challenged with the carbon ion numbers at SNAKE which were sufficient to show depolarization. The localization of the dye did also not change as was seen in TMRE stained mitochondria post irradiation. These results indicated that when challenged with 100 ions per point (5.6 pJ per beamspot) or less using an irradiation matrix (6x6 for example) there was no detectable change in MTG (Figs.32, 32) and therefore overall membrane composition. When the AIFIRA beamline was used to challenge the MTG staining with very high ion numbers an effect was seen (Fig.34). This effect however was only invoked at extremely high numbers (>100 000) of ions deposited over the total cell. The heat

generated by the ionization events, even at these high ion numbers is however still negligible and cannot be considered a key contributing factor to any of the effects seen in this work (private communication with Dr Christoph Greubel). The loss of MTG specific signal was however rather slow in comparison to TMRE. This slow loss of signal as shown in Fig.36 could be an indicator of membrane dissociation in the targeted mitochondria. The loss of signal over time was also not as abrupt as seen in TMRE results indicating that the damage seen in these high ion number irradiations was not related to depolarization which would have manifested itself as a far more abrupt drop in signal intensity. When MTG is observed with super resolution methods like STED the stain manifests itself as a diffuse point like mitochondrial membrane staining (Ishigaki et al., 2016), so changes in mitochondrial morphology or damage to the membrane may well induce a change in staining pattern over time. In addition the high number of total ions applied (>1 million) could have lead to a structural change in MTG and therefore a loss of signal intensity.

In summary, the MTG staining provided an important membrane counterstain which showed no changes after irradiation as compared to the depolarization dependent loss of TMRE signal. In 20 separately irradiated cells at SNAKE and further experiments performed at AIFIRA, there was no loss of MTG signal when irradiated with the same ion numbers capable of inducing depolarization. MTG has been shown by other literature to colocalize in the mitochondrial membrane by binding to proteins (Kholmukhamedov et al., 2013a) so we can therefore conclude that no major or lasting membrane perturbations were seen during/after irradiation.

7.4 Membrane integrity

Plasma membrane integrity after targeted irradiation was another interesting aspect analyzed. The ions used to irradiate the mitochondria traverse the media above the cells, the plasma membrane, the cytoplasm and then the mitochondria before exiting the cell by the same route on the other side before being stopped in the scintillator. When applying 100 carbon ions per point there is an undeniable and total loss of mitochondrial membrane potential which is very likely due to a short term membrane disruption of sufficient magnitude to depolarize the mitochondria. In light of this finding the question arose what effect the ionizing radiation had on the plasma membrane as the amount of energy deposited per µm distance travelled would be the same at the plasma membrane as at the mitochondrial membrane. The main differences between mitochondrial and plasma membrane are that the IMM has a high electric field across it and has, compared to the plasma membrane, a different distribution of proteins especially for pumping protons and cardiolipin. It is therefore not clear if the membranes respond differently due to their composition and or their differences in electric field. A test of the damage to the plasma membrane was performed by loading the extracellular space, in this case the cell growth media with PI which is held outside of the cell if the membrane is undamaged but can enter if the membrane is ruptured. If the membrane were to be damaged the PI would enter the cell and intercalate with the DNA in the nucleus which would manifest itself as a bright nuclear fluorescence signal. Targeted irradiation of mitochondria using either small matrices with 4x4 and 6x6 irradiation points and AutoTarget regimes based on >1000 total points per cell, were performed in the presence of PI in the media.

In none of the cases was a PI signal seen within the timeframe of imaging (up to 6 hours). Therefore it was concluded that there was no damage to the membrane that would allow PI to enter the cell. Investigating longer time points (up to 24 hrs) may yield different results; however these later stage membrane alterations may be due to the biological response of a cell and not the direct interaction of radiation with the membrane. The intrinsic limitation of this assay is however the size of the PI molecule as it will only be able to detect holes through which it can readily pass.

PI is able to pass through membrane holes ~2-3nm in diameter as this is the size of the molecule. The molecule size was therefore the major limitation as smaller nanopores of < 2nm would not enable PI to pass into the cell. Electroporation experiments on cells have conclusively shown that the small scale (1nm) nanopores produced during electroporation do not enable PI to enter the cell and intercalate with the DNA, but only when larger holes are created can PI enter the cell (Beebe et al., 2013). Work using Thallium ions has also conclusively shown that PI is not an ideal candidate for nanopore detection (Bowman et al., 2010a). Therefore the PI experiments allow us to measure the production of larger perturbations in the cell membrane which in the case of irradiation did not occur. The possibility that transient nanopores were created by the ions traversing the membrane is therefore still to be investigated. What can however be stated is that the transient changes in membrane integrity did not change into more severe membrane purturbations. Also investigating longer time points may yield different results, however these later stage membrane alterations would undoubtedly be due to the biological response of a cell and not the direct interaction of radiation with the membrane. There has been a renewed interest in membrane integrity and nanopore formation after electroporulation techniques became popular. Electroporulation uses pulsed electric fields to induce short-term membrane permeability (Chen et al., 2006, Ho and Mittal, 1996). Many of the techniques used to investigate this phenomenon will be invaluable for the further analysis of radiation induced membrane damage. There is a specific modern technique based on Thallium ion uptake which could shed light on nanopore formation (Bowman et al., 2010b). The analysis of membrane integrity after ionizing radiation is an area of interest and will require further research.

7.5 ROS

In the field of radiation biology ROS is a commonly used explanation for the responses which have no other measurable origin. ROS measurements using ROS probes in combination with non-imaging techniques such as flow cytometry or fluorescence plate readers are likely to yield false positive results (Kalyanaraman et al., 2012a, Woolley et al., 2013, Polster et al., 2014). The interaction of ionizing radiation with water and biological matter creates radical chemical species which can cause further damage (Azzam et al., 2012) however the ROS species created very rapidly react with the matter around them and the initial effect relating to water hydrolysis occurs in the time scale of femtoseconds (Azzam et al., 2012). Our investigation of ROS looked at the initial superoxide production upon targeted mitochondrial irradiation, as well as the changes in glutathione redox potential of a biosensor attached to the IMS of mitochondria. The consensus in the field of radiation biology is that ROS are behind a vast array of different detrimental effects in cells treated with

ionizing radiation (Yamaguchi and Kashiwakura, 2013, Reisz et al., 2014, Riley, 1994). The majority of these studies use irreversible fluorescent dyes to detect O_2^- or H_2O_2 such as DCF-DA, MitoSOX, CellROX or dihydroethidium. In these cases most effects are measured after homogenous irradiation of cells so the ROS signal measured, usually by a fluorescence plate reader or in the best case by a confocal microscope, can show a general increase in a fluorescence-based signal after ionizing radiation. The issues with such measurements are the probes themselves. There is no doubt that ionizing radiation induces production of radicals but in most cases the changes in fluorescence intensity do not reflect these changes accurately as the probes are not specific enough to differentiate between non-specific interactions with other cellular processes and interactions with the radical moiety (Kalyanaraman et al., 2012b). A prime example of the problems faced in ROS measurement is the widely used probe Dihydroethidium and its mitochondrial variety MitoSOX. MitoSOX produces two distinct products which both show an increased fluorescence signal, the first product Mito-E+ is not specific to superoxide interaction, the second, Mito-OH-E+ is specific to superoxide interaction (Zielonka and Kalyanaraman, 2010). MitoSOX is therefore not a good readout for experiments where irradiation and analysis cannot be performed and analyzed in real time. Other dyes specific to a variety of ROS have been shown to be produced by X-ray interaction with cells (Rappole et al., 2012). The benefit of SNAKE is that a defined number of high LET ions can be applied to a known location within a defined timeframe. Water radiolysis experiments with high LET particles have shown that superoxide production increases with LET and that the estimated yield of Superoxide with high LET particles of 250eV/nm is $6x10^{-9}$ mol/Joule (Baldacchino, 2008). The ability to apply high LET (350 kev/µm) carbon ions at a rate of ~2 kHz allows the production of superoxide to be probed in real time.

The experiments showed a distinct and very rapid peak in fluorescence after targeted irradiation (Fig.41). The peak was very distinct at between 1000-250 ions (Fig.42) however below 125 ions per point the fluorescence intensity peak was far smaller and at the lowest ion applications (30-15 ions) was not detectable. As the fluorescence intensity peak seems to depend on the energy deposited, it is very likely that the smaller numbers of ions applied are not sufficient, given the limitation of the experimental setup relating to the exposure time required, imaging speed and sensitivity to image MitoSOX. The exposure time will play a vital role here as during the experiments at SNAKE an exposure time of 1s was required to image MitoSOX. Given the values in Fig.43 this would indicate that the effect at ion applications below 62 ions was missed due to the ion application time being below 1s. This could mean that the fast, low amplitude peaks as seen below 125 ions could appear and disappear again during the time between images. It is therefore very possible that the events in the lowest ion numbers (30-15) were missed. However the decreasing fluorescence intensity maxima caused by mitoSOX would indicate that we are reaching the limit of our detection capability, as the changes were in the range of single gray scale values and could not be interpreted as superoxide events.

In addition to the MitoSOX fluorescence intensity peaks, an undershoot of signal below initial background level was observed for higher ion numbers. This could be related to one of two reasons, firstly, MitoSOX, which is irreversibly changed to its product by superoxide, could photo bleach. The other option is that the depolarization of the mitochondria leads to the dissociation of the MitoSOX signal into the cytoplasm as MitoSOX accumulates only in Polarized mitochondria. The dissociation of MitoSOX into the cytoplasm is

not a sign of ROS spreading throughout the cell (Polster et al., 2014). The ion numbers required to induce the MitoSOX peaks are within the same range required to cause instant and total depolarization of the targeted mitochondria. Therefore this decrease could well be related to depolarization and consequent dye loss due to the TPP+ targeting marker. The effects of ionizing radiation on mitochondria as measured by two separate experiments one with TMRE and another with MitoSOX with the same ion number and similar exposure times were compared. The rise time to the peak of the fluorescence intensity for the MitoSOX, correlated with the ion application time (Fig.43) caused by a 6x6 matrix with 125 ions/point which may well be a trigger for mitochondrial depolarization. From the TMRE experiments it is known that 100 ions per point are more than enough to induce localized depolarization, so a MitoSOX burst may well be occurring along with a mitochondrial depolarization event. The literature on mitochondrial ROS and depolarization states that ROS bursts can occur when mitochondria depolarize (Zorov et al., 2014). Weather the superoxide burst causes the depolarization or the depolarization causes the MitoSOX peak (Fig.50) is debatable. The two processes are, however, linked as the loss of polarization will lead to MitoSOX signal dipping below background as the accumulation of MitoSOX depends on the membrane potential of the mitochondria as Mitosox is targeted to the mitochodnria with a TPP+ group.

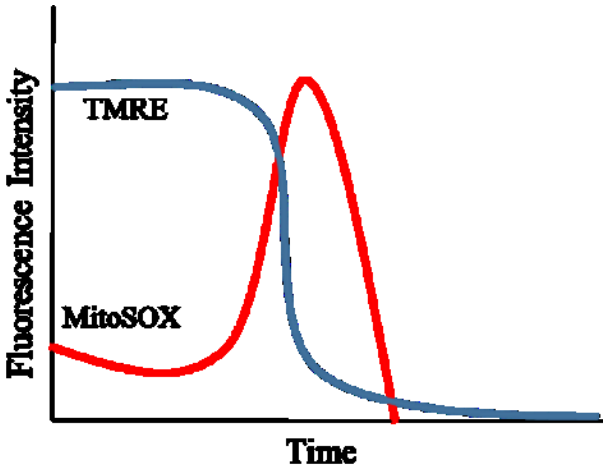

Fig.50 Graphical representation of a hypothesis relating ROS (MitoSOX) and membrane polarization (TMRE) to one another in a hypothesis relating to the relationship between ROS and depolarization

To further investigate the superoxide production it would be necessary to upgrade the imaging setup with a faster and more sensitive sCMOS detector system. Currently the imaging system is limited to a few images per second and if this could be increased along with the quantum efficiency of the detector then perhaps the same effect could be detected at lower ion levels. Currently the imaging setup could be the limitation for not seeing the effect at lower ion numbers.

However there is one further biological factor which could explain the lack of superoxide peak seen after targeted irradiation with low number of ions, superoxide dismutase (SOD). SOD is an enzyme present in mitochondria of cells which has an astoundingly fast superoxide to oxygen (O_2) conversion rate of 10^9 mol^{-1} sec^{-1}(Culotta et al., 2006). This is one of the fastest known catalytic enzymes and its sole purpose is to regulate the levels of superoxide, which is also a potent side product of the mitochondrial activity relating to energy metabolism.

Given the current limitations in measuring ROS and specifically superoxide by fluorescent dyes, we made use of a combination of MitoSOX and roGFP2 probes to try to determine if there was a measurable increase in detectable ROS after irradiation. roGFP2 irradiation experiments were not as conclusive as the MitoSOX experiments. roGFP2 is a genetically encoded biosensor which can measure changes in redox potential in cells. The sensor system works by shifting its excitation spectrum from 400 to 470nm when the cysteine residue in the green fluorescent proteins (GFP) beta-barrel structure is either oxidized or reduced (Schwarzländer et al., 2008). roGFP2 has been used for assessing the ability of chemicals to induce intracellular ROS (Schwarzländer et al., 2009). When linked to mitochondria, the initial idea was to use the probe to measure the change in ROS after ionizing radiation. The plasmid was grown in E.coli bacteria, purified and introduced into U2OS cells by our collaborators in Bordeaux so the experiments performed were limited to the two beamtimes at AIFIRA. The first set of experiments showed no change in the 400:470nm emission value after irradiation indicating no change of the cysteine residues oxidation state in the roGFP protein. After initial experiments were performed on the beamline, further analysis of the roGFP attached to the mitochondria showed that the residue was already nearly completely oxidized during the initial experiments (Fig.48). Analysis of the biosensor showed that the sensor could be "reset" to a reduced state before experiments using a reducing agent.

During the second set of experiments 1μM DTT was used in an attempt to reduce the sensor prior to irradiation (Fig.49) as was performed in Dooley et al. (Dooley et al., 2004). The second batch of experiments performed in Bordeaux showed a lower starting value of the 400:470nm indicating a more reduced state of the probe. However after challenging the tagged mitochondria with ionizing radiation, in the form of protons, no difference was seen between unirradiated and irradiated mitochondria. Both of the mitochondrial clusters compared showed a slight increase in 400:470nm ratio. However this is most likely due to the photo toxicity induced by imaging the system with the two excitation wavelengths at a high framerate (Fig.49). The experiments performed during this second beamtime also did not show any conclusive radiation induced change of the roGFP2 probe leading us to question the suitability of the probe for radiation induced effects. The results thus far indicate that the probe is either not sensitive enough to measure the perturbations cause by ionizing radiation or that there is no detectable effect at this energy. The energy applied was within the same range as the 100 carbon ions/point applied at SNAKE; this number lead only to a very small increase in MitoSOX (Fig.43).

Tests on the roGFP2 cell line performed in Munich offline, using a laser scanning microscope and a strong reducing agent, 2-mercaptoethanol showed that μM concentrations were sufficient to reduce the cysteine residues in the biosensor within seconds. The reducing agent showed the expected shift in 400:470nm ratio

and therefore proved that the biosensor works and is responsive to changes in redox potential. The resetting of the sensor into its reduced state lead to the expected 400:470nm value range. However, no further experiments could be performed using either the AIFIRA or SNAKE microbeams so this result should further be investigated in future experiments. The results in this work show no conclusive evidence for the change in the biosensor after irradiation. However this is not due to the inability of the sensor to perform a Redox measurements, as reducing agents change the 400:470nm ratio. roGFP2 appears not to be an ideal sensor for testing ionizing radiation induced ROS produced by mitochondrial irradiation as there are no visible changes which can be correlated with the irradiation of the tagged mitochondria. It is possible that the short bursts of superoxide production as measured by MitoSOX are converted to H_2O_2 and O_2 and diffuse so quickly that their interaction with roGFP2 is not sufficient to produce oxidation of enough cysteine residues to show a change in 400:470nm ratio. In other words, the probe sensitivity may well be far below that of the irradiation system.

To further test roGFP2 a more sophisticated experiment would be necessary in which a delicate balance of reducing agent and medium transfers would require a new experimental setup. Using a LCI container with an input and output in which reducing agent containing medium could be introduced into a sample just before irradiation before being washed out again and replaced with warm medium.

In summary, there is a strong indication that targeted irradiation of mitochondria leads to a highly localized increase of superoxide as measured by MitoSOX. This production of ROS could be a mechanistic reason for mitochondrial depolarization. However, until the secondary product of the initial superoxide ROS formation, H_2O_2, is conclusively shown it is not possible to prove that the radiation applied is sufficient to produce enough damage to lead to mitochondrial depolarization. Due to the high catalytic turnover of SOD, O_2^- is rapidly turned into either H_2O_2 or O_2 both of which are far more stable and in the case of H_2O_2 also has the potential for further damage production. Only with the highest ion applications (1000/point) was a high peak of fluorescence intensity measured with the fluorescence microscopy. When 125 ions were applied in a 6x6 matrix, which is more than sufficient to depolarize mitochondria, the MitoSOX fluorescence signal intensity increase was very small. Measurements from experiments using ions below this value show no visible superoxide peaks. In contrast the roGFP2 experiments did not conclusively show a change of the probes redox state after irradiation. The probe requires further investigation and the sensitivity of the probe needs to be further assessed as there are more sensitive roGFP2 variants (Bhaskar et al., 2014, Tormos and Chandel, 2011)

Investigating radiation induced mitochondrial ROS using targeted irradiation will enable a much more accurate description of the initial response of a cell to ionizing radiation. The results show an initial insight into the ROS response of mitochondria to ion beams but further experiments will be required to fully quantify the responses.

7.6 Further developments and objectives

During the three years allocated for this thesis many experiments were performed at the SNAKE microbeam facility. During the 11 months of downtime that the facility experienced in 2015 experiments were performed during two beamtimes at AIFIRA. Due to the limited number of beamtimes available not all of the planned experiments could be performed. There are therefore aspects of this work which are currently still "work in progress". Longer term imaging (longer than 6 hours) is a key aspect that still needs further work so that the effects of ionizing radiation on mitochondria can be put into a cell survival/death context. This along with a single cell survival test would be an ideal way to verify the response of the overall cell to ionizing radiation. In many of the experiments a more sensitive and faster imaging setup would have been ideal to elucidate the time required for certain effects such as depolarization and mitoSOX flashes. In addition a more robust methodological analysis of the mitochondrial pathways is necessary to understand the mechanism of the mitochondrial depolarization seen. This is another methodological and technical aspect that needs more work. An upgraded imaging system with higher quantum efficiency and faster imaging capabilities would allow for realtime ROS measurements and elucidation of real-time depolarization responses to individual ion impacts. A more easily achievable goal would also be to have a time-stamped irradiation point whereby it would be possible to define when each irradiation point was actually targeted and the duration of each application of ions.

As some of the experiments performed would have benefitted from changing medium, washing or applying inhibitors or dyes while the sample was in the microscope while being irradiated, a solution was needed as the current LCI had no way of dealing with the requirements. In order to solve these issues online, a closed system LCI with flow was designed and created as a prototype for future experiments (Fig.51). The design of the system was modelled and created with the help of Judith Reindl. The design added holes to the lid of the LCI and holes to the bottom of the LCI along with a set of channels perpendicular to the lid hole creating a channel from the lid to the medium reservoir. This design allows for the replacement of the medium inside the LCI with fresh medium/wash buffer containing any dye, inhibitor or fluid necessary. The addition of a syringe pump enabled a constant flow rate into the sample.

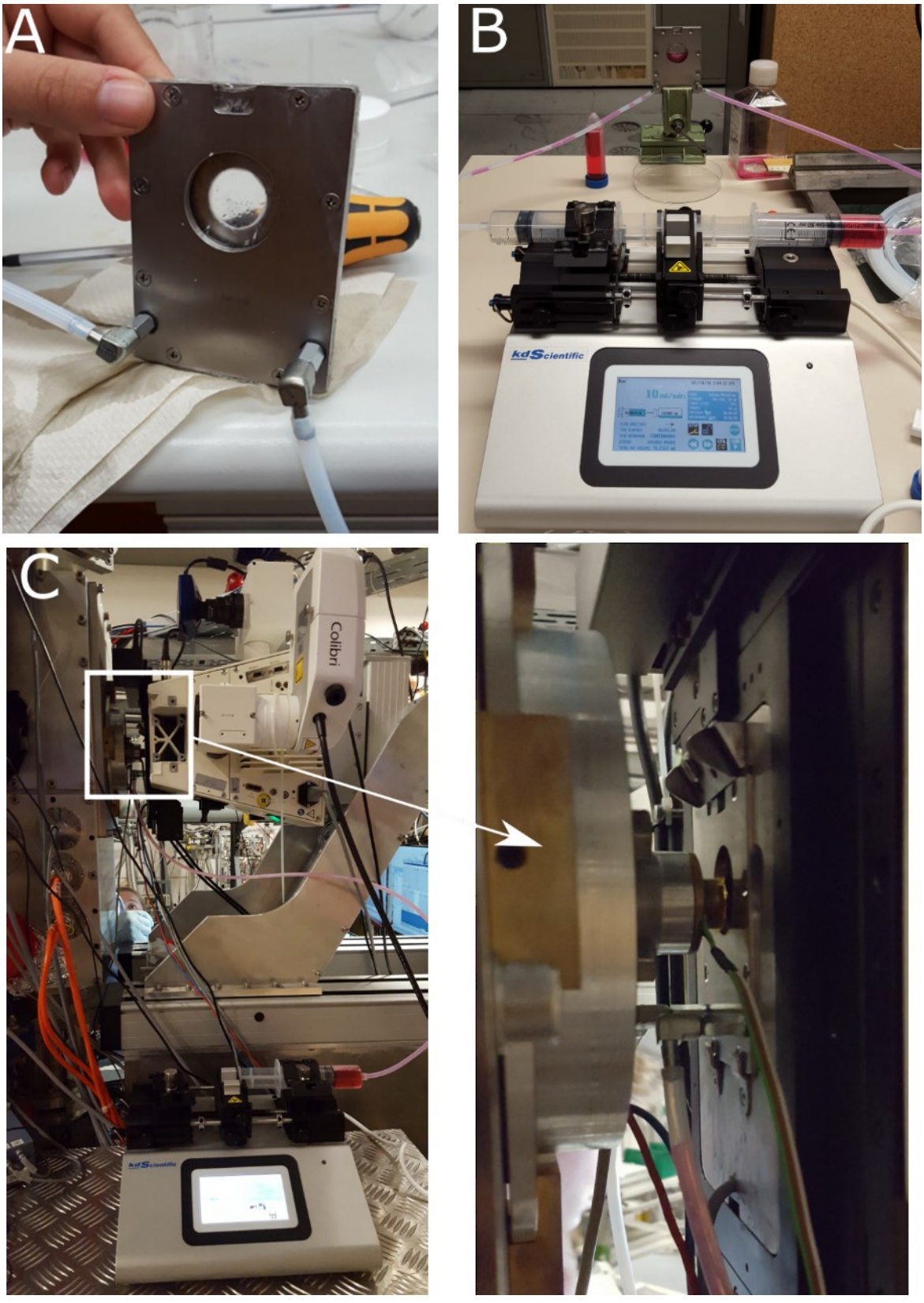

Fig.51 Images show the pump LCI(A) which is a modification which adds inlets and 90° rotatable hose adapters to the LCI container. The system can be hooked up to a pump which can pump medium in and out of the closed LCI (B). The container online at SNAKE (C) shows how the system will be used during irradiation.

8 Conclusion

The capability to perform targeted irradiation of mitochondria in live cells has been demonstrated in this thesis. Furthermore it has been shown that it is possible to analyse mitochondrial markers in real time using online fluorescence microscopy during irradiation. Mitochondrial irradiation using carbon ions and protons of varying LET, above a threshold, induces irreversible depolarization in the targeted mitochondria and does not show any changes to unconnected mitochondria in the same cell. All mitochondria connected to the area of irradiation however will undergo mitochondrial depolarization as visualized by the loss of TMRE signal. The depolarization phenomenon has been unequivocally shown to be a biological effect and not an effect of highly localised dye destruction. The dye leaves the irradiated mitochondria once these become depolarized and lose their charge and the dye dissipates into the cytoplasm. This relocalization of TMRE indicates that the TMRE itself is not lost but just released from the mitochondria. Depolarization can be induced by both protons and carbon ions of varying LET as long as the same amount of energy is deposited per unit area. The results on this radiation induced depolarization are consistent but a definitive cause remains to be established. Initial experiments would suggest that radiation induced ROS may play some role in the effect as targeted irradiation induces flashes of superoxide as measured by MitoSOX. There were no changes observed in MTG staining at the lower levels of ion application which indicated no alteration in outer mitochondrial membrane integrity. In addition the roGFP2 probe was used as a marker for IMS integrity and this marker also did not show any change in intensity/distribution. Although highly indicative of zero change in membrane integrity only experiments using a soluble mitochondrial marker such as cytochrome c would indicate if the membrane was really damaged or not as its release would indicate a change in membrane integrity.

The body of work has been the development of a methodology to perform and assess targeted irradiation of mitochondria in live cells using ion beams. The method established allows for a defined deactivation of the mitochondrial membrane potential by localized energy deposition. Although these drastic effects on mitochondrial polarization state have been seen, in the short term (up to 30 min), long term analysis of cells after irradiation has not yet been possible. It can therefore not be ruled out that the amounts of energy required to depolarize mitochondria are also not enough to induce cell death. Further methodological advances and experimental time is required to see if this may be the case or not. Apoptosis induction, signaling cascades and clonogenic survival of individual cells would be ideal experiments to perform to assess the overall effect of ionizing radiation targeted to the mitochondria. The ion microbeam SNAKE has the ability to be a fundamental tool in the analysis of the mitochondrial response to ionizing radiation. Fundamental questions about the mitochondrial response to ionizing radiation were answered in this body of work and optimization of the experimental setup and conditions required for further experiments have also been establish

9 Publications

2017:

- *Live cell imaging of mitochondria following targeted irradiation in situ reveals rapid and highly localized loss of membrane potential*. Dietrich W. M. Walsh, Christian Siebenwirth, Christoph Greubel, Katarina Ilicic, Judith Reindl, Stefanie Girst, Giovanna Muggiolu, Marina Simon, Philippe Barberet, Hervé Seznec, Hans Zischka, Gabriele Multhoff, Thomas E. Schmid & Guenther Dollinger , Scientific Reports 7, 2017. doi:10.1038/srep46684
- *Chromatin organization revealed by nanostructure of irradiation induced γH2AX, 53BP1 and Rad51 foci*. Judith Reindl, Stefanie Girst, Dietrich W. M. Walsh, Christoph Greubel, Benjamin Schwarz, Christian Siebenwirth, Guido A. Drexler, Anna A. Friedl & Günther Dollinger. Scientific Reports 7, 2017. doi:10.1038/srep40616

2016:

- Low LET proton microbeam to understand high-LET RBE by shaping spatial dose distribution,NIMB, Christoph Greubel, Katarina Ilicic, Thomas Rösch, Judith Reindl, Christian Siebenwirth, Marcus Moser, Stefanie Girst, Dietrich W.M. Walsh, Thomas E. Schmid, Günther Dollinger.
- Reduced side effects by proton minibeam radiotherapy in a mouse ear model, Radiation oncology, S. Girst, C. Greubel, J. Reindl, C. Siebenwirth, O. Zlobinskaya, D.W.M. Walsh, K. Ilicic, M. Aichler, A. Walch, J. J. Wilkens, G. Multhoff, G. Dollinger, T. E. Schmid

2015:

- Determination of the accuracy for targeted irradiations of cellular substructures at SNAKE. NIMB 348, C. Siebenwirth, C. Greubel, S.E. Drexler, S. Girst, J. Reindl, D.W.M. Walsh, G. Dollinger, A.A. Friedl, T.E. Schmid, G.A. Drexler

10 Acknowledgements

I would like to thank all of my fellow scientists at both the Klinikum Rechts der Isar and the Universität der Bundeswehr München for the support, discussion and assistance throughout the duration of this project. Without these people the experiments would not have been possible. In particular I would like to thank Christoph Greubel for advice on the physics side of the experiments and the support during data analysis. Christian Siebenwirth for his help during experiments at SNAKE. Judith Reindl for organization of beamtimes, CAD work on the LCI and enthusiasm about data analysis. Katarina Ilicic for the many long discussions about the intricate details of radiation biology and the long nights of work in the lab at SNAKE. My Supervisors Thomas Schmid, Günther Dollinger and Gabrielle Multhoff for the discussions and support during the project.

An extra thanks goes to Hans Zischka who has been involved in this project for the last year and who very kindly donated chemicals for mitochondrial analysis as well as discussion and proofs for the publication.

I would like to thank my fantastic collaborators at the AIFIRA facility for preparing cells, organizing beam times for me and enabling me to perform my experiments there during our year of downtime at the SNAKE facility. Hervé Seznec especially for the invite to work at the facility and the effort to accommodate me, as well as Philippe Barberet for the advice and expertise during experiments at AIFIRA. I would like to thank Giovanna Muggiolu for the great discussions, help with preparing for beam times in Bordeaux and for the non-beamtime activities in and around Bordeaux!

All members of SPRITE and the Marie Curie ITN Fellowship organizers, for the fantastic workshops, meetings and discussions across physics and biology.

Last but by far not least my Parents and my partner Zsuzsanna for putting up with me during beam times and throughout the emotional rollercoaster that has been this thesis throughout the last three and a half years. Especially, at this point I would like to thank Dr. Jeremy Walsh and Dr. Linda Walsh for emotional, financial and academic support as well as for the experimental planning and discussions had over many meals, which, in many instances lead me to new analysis methods and experimental approaches. Every time I came home frustrated by paper revisions or beam times not working my family was there for me to cheer me up. Thank you!

11 References

ALAYNICK, W. A. 2008. Nuclear receptors, mitochondria and lipid metabolism. *Mitochondrion,* 8**,** 329-337.

ALEXEYEV, M., SHOKOLENKO, I., WILSON, G. & LEDOUX, S. 2013. The Maintenance of Mitochondrial DNA Integrity—Critical Analysis and Update. *Cold Spring Harbor Perspectives in Biology,* 5.

AMCHENKOVA, A. A., BAKEEVA, L. E., CHENTSOV, Y. S., SKULACHEV, V. P. & ZOROV, D. B. 1988. Coupling membranes as energy-transmitting cables. I. Filamentous mitochondria in fibroblasts and mitochondrial clusters in cardiomyocytes. *The Journal of Cell Biology,* 107**,** 481-495.

AMOÊDO, NÍVEA D., VALENCIA, JUAN P., RODRIGUES, MARIANA F., GALINA, A. & RUMJANEK, FRANKLIN D. 2013. How does the metabolism of tumour cells differ from that of normal cells. *Bioscience Reports,* 33**,** e00080.

ANDREY, V. K. & RAIMUND, M. 2009. Heterogeneity of Mitochondria and Mitochondrial Function within Cells as Another Level of Mitochondrial Complexity. *International Journal of Molecular Sciences,* 10.

ASSMANN, W., DE BOER, J., MEYER-BERKHOUT, U., SKORKA, S., HUENGES, E., KIENLE, P., MORINAGA, H., NOLTE, E., VONACH, H., MÜNZER, H., ROHRER, L. & SCHNITTER, H. 1974. The Munich MP tandem. *Nuclear Instruments and Methods,* 122**,** 191-203.

AZZAM, E. I., JAY-GERIN, J.-P. & PAIN, D. 2012. Ionizing radiation-induced metabolic oxidative stress and prolonged cell injury. *Cancer letters,* 327**,** 48-60.

BALDACCHINO, G. 2008. Pulse radiolysis in water with heavy-ion beams. A short review. *Radiation Physics and Chemistry,* 77**,** 1218-1223.

BARBERET, P., DAUDIN, L., GORDILLO, N., SORIEUL, S., SIMON, M., SEZNEC, H., IDARRAGA, I., INCERTI, S., BALANA, A. & MORETTO, P. 2011. First results obtained using the CENBG nanobeam line: performances and applications. *Nuclear Instruments and Methods in Physics Research Section B: Beam Interactions with Materials and Atoms,* 269**,** 2163-2167.

BARBERET, P. & SEZNEC, H. 2015. Advances in microbeam technologies and applications to radiation biology. *Radiation Protection Dosimetry,* 166**,** 182-187.

BEEBE, J. S., SAIN, M. N. & REN, W. 2013. Induction of Cell Death Mechanisms and Apoptosis by Nanosecond Pulsed Electric Fields (nsPEFs). *Cells,* 2.

BENOV, L., SZTEJNBERG, L. & FRIDOVICH, I. 1998. Critical evaluation of the use of hydroethidine as a measure of superoxide anion radical. *Free radical biology & medicine,* 25**,** 826-831.

BENZ, R. & MCLAUGHLIN, S. 1983. The molecular mechanism of action of the proton ionophore FCCP (carbonylcyanide p-trifluoromethoxyphenylhydrazone). *Biophysical Journal,* 41**,** 381-398.

BERNS, M. W., GROSS, D. C. L., CHENG, W. K. & WOODRING, D. 1972. Argon laser micro-irradiation of mitochondria in rat myocardial cells in tissue culture. *Journal of Molecular and Cellular Cardiology,* 4**,** IN15-IN16.

BHASKAR, A., CHAWLA, M., MEHTA, M., PARIKH, P., CHANDRA, P., BHAVE, D., KUMAR, D., CARROLL, K. S. & SINGH, A. 2014. Reengineering Redox Sensitive GFP to Measure Mycothiol Redox Potential of Mycobacterium tuberculosis during Infection. *PLOS Pathogens,* 10**,** e1003902.

BOURRET, S., VIANNA, F., DEVÈS, G., ATALLAH, V., MORETTO, P., SEZNEC, H. & BARBERET, P. 2014. Fluorescence time-lapse imaging of single cells targeted with a focused scanning charged-particle microbeam. *Nuclear Instruments and Methods in Physics Research Section B: Beam Interactions with Materials and Atoms,* 325**,** 27-34.

BOWMAN, A. M., NESIN, O. M., PAKHOMOVA, O. N. & PAKHOMOV, A. G. 2010a. Analysis of Plasma Membrane Integrity by Fluorescent Detection of Tl(+) Uptake. *The Journal of membrane biology,* 236**,** 15-26.

BOWMAN, A. M., NESIN, O. M., PAKHOMOVA, O. N. & PAKHOMOV, A. G. 2010b. Analysis of Plasma Membrane Integrity by Fluorescent Detection of Tl+ Uptake. *The Journal of Membrane Biology,* 236**,** 15-26.

CHEN, C., SMYE, S. W., ROBINSON, M. P. & EVANS, J. A. 2006. Membrane electroporation theories: a review. *Medical and Biological Engineering and Computing,* 44**,** 5-14.

CHEN, X. J. & BUTOW, R. A. 2005. The organization and inheritance of the mitochondrial genome. *Nat Rev Genet,* 6**,** 815-825.

COLLINS, T. J. & BOOTMAN, M. D. 2003. Mitochondria are morphologically heterogeneous within cells. *Journal of experimental biology*.

COOKE, M. S., EVANS, M. D., DIZDAROGLU, M. & LUNEC, J. 2003. Oxidative DNA damage: mechanisms, mutation, and disease. *The FASEB Journal,* 17**,** 1195-1214.

CULOTTA, V. C., YANG, M. & O'HALLORAN, T. V. 2006. Activation of superoxide dismutases: Putting the metal to the pedal. *Biochimica et biophysica acta,* 1763**,** 747-758.

CUMMINGS, B. S., WILLS, L. P. & SCHNELLMANN, R. G. 2004. Measurement of Cell Death in Mammalian Cells. *Current protocols in pharmacology / editorial board, S.J. Enna (editor-in-chief) ... [et al.],* 0 12**,** 10.1002/0471141755.ph1208s25.

DATZMANN, G., DOLLINGER, G., GOEDEN, C., HAUPTNER, A., KÖRNER, H.-J., REICHART, P. & SCHMELMER, O. 2001. The Munich microprobe SNAKE: First results using 20 MeV protons and 90 MeV sulfur ions. *Nuclear Instruments and Methods in Physics Research Section B: Beam Interactions with Materials and Atoms,* 181**,** 20-26.

DIKALOV, S. I., KIRILYUK, I. A., VOINOV, M. & GRIGOR'EV, I. A. 2011. EPR Detection of Cellular and Mitochondrial Superoxide Using Cyclic Hydroxylamines. *Free radical research,* 45**,** 417-430.

DISTELMAIER, F., KOOPMAN, W. J. H., TESTA, E. R., DE JONG, A. S., SWARTS, H. G., MAYATEPEK, E., SMEITINK, J. A. M. & WILLEMS, P. H. G. M. 2008. Life cell quantification of mitochondrial membrane potential at the single organelle level. *Cytometry Part A,* 73A**,** 129-138.

DOOLEY, C. T., DORE, T. M., HANSON, G. T. & JACKSON, W. C. 2004. Imaging dynamic redox changes in mammalian cells with green fluorescent protein indicators. *Journal of Biological ….*

DREXLER, G. A., SIEBENWIRTH, C., DREXLER, S. E., GIRST, S., GREUBEL, C., DOLLINGER, G. & FRIEDL, A. A. 2015. Live cell imaging at the Munich ion microbeam SNAKE – a status report. *Radiation Oncology,* 10**,** 42.

EHRENBERG, B., MONTANA, V., WEI, M. D., WUSKELL, J. P. & LOEW, L. M. 1988. Membrane potential can be determined in individual cells from the nernstian distribution of cationic dyes. *Biophysical Journal,* 53**,** 785-794.

ERNSTER, L. & SCHATZ, G. 1981. Mitochondria: a historical review. *The Journal of Cell Biology,* 91**,** 227s-255s.

GAN, Z., AUDI, S. H., BONGARD, R. D., GAUTHIER, K. M. & MERKER, M. P. 2011. Quantifying mitochondrial and plasma membrane potentials in intact pulmonary arterial endothelial cells based on extracellular disposition of rhodamine dyes. *American Journal of Physiology - Lung Cellular and Molecular Physiology,* 300**,** L762-L772.

GERENCSER, A. A., CHINOPOULOS, C., BIRKET, M. J., JASTROCH, M., VITELLI, C., NICHOLLS, D. G. & BRAND, M. D. 2012. Quantitative measurement of mitochondrial membrane potential in cultured cells: calcium-induced de- and hyperpolarization of neuronal mitochondria. *The Journal of Physiology,* 590**,** 2845-2871.

GRAAFF, R. J. 1960. Tandem Electrostatic Accelerators. *Nuclear Instruments and Methods,* 8**,** 195-202.

GRAY, M. W., BURGER, G. & LANG, B. F. 2001. The origin and early evolution of mitochondria. *Genome Biology,* 2**,** reviews1018.1-reviews1018.5.

GUTSCHER, M., PAULEAU, A.-L., MARTY, L., BRACH, T., WABNITZ, G. H., SAMSTAG, Y., MEYER, A. J. & DICK, T. P. 2008. Real-time imaging of the intracellular glutathione redox potential. *Nat Meth,* 5**,** 553-559.

HABLE, V., GREUBEL, C., BERGMAIER, A., REICHART, P., HAUPTNER, A., KRÜCKEN, R., STRICKFADEN, H., DIETZEL, S., CREMER, T., DREXLER, G. A., FRIEDL, A. A. & DOLLINGER, G. 2009. The live cell

irradiation and observation setup at SNAKE. *Nuclear Instruments and Methods in Physics Research Section B: Beam Interactions with Materials and Atoms,* 267**,** 2090-2097.
HAKEM, R. 2008. DNA-damage repair; the good, the bad, and the ugly. *The EMBO Journal,* 27**,** 589-605.
HALESTRAP, A. P. 2009. What is the mitochondrial permeability transition pore? *Journal of Molecular and Cellular Cardiology,* 46**,** 821-831.
HINDERER, G., DOLLINGER, G., DATZMANN, G. & KÖRNER, H. J. 1997. Design of the new superconducting microprobe system in Munich. *Nuclear Instruments and Methods in Physics Research Section B: Beam Interactions with Materials and Atoms,* 130**,** 51-56.
HO, S. Y. & MITTAL, G. S. 1996. Electroporation of Cell Membranes: A Review. *Critical Reviews in Biotechnology,* 16**,** 349-362.
HONGNING, Z., MEI, H., YUNFEI, C. & TOM, K. H. 2009. Consequences of Cytoplasmic Irradiation: Studies from Microbeam. *Journal of Radiation Research,* 50.
ISHIGAKI, M., IKETANI, M., SUGAYA, M., TAKAHASHI, M., TANAKA, M., HATTORI, S. & OHSAWA, I. 2016. STED super-resolution imaging of mitochondria labeled with TMRM in living cells. *Mitochondrion,* 28**,** 79-87.
ISHIKAWA, K., TAKENAGA, K., AKIMOTO, M., KOSHIKAWA, N., YAMAGUCHI, A., IMANISHI, H., NAKADA, K., HONMA, Y. & HAYASHI, J.-I. 2008. ROS-Generating Mitochondrial DNA Mutations Can Regulate Tumor Cell Metastasis. *Science,* 320**,** 661.
J. D. COCKCROFT, E. T. S. W. 1932. Artificial Production of Fast Protons. *Nature Reviews Cancer,* 129**,** 242.
JIN, W.-G., KATOH, K., MINOWA, T. & IKEDA, T. 2013. Light Microbeams by Tapered Glass Capillaries for Biological Irradiation. *Journal of Computer and Communications,* 01**,** 5.
JONGHEE, Y., SEUNG-WOOK, R., SEUNGHEE, L. & CHULHEE, C. 2015. Cytosolic Irradiation of Femtosecond Laser Induces Mitochondria-dependent Apoptosis-like Cell Death via Intrinsic Reactive Oxygen Cascades. *Scientific Reports,* 5.
KALYANARAMAN, B., DARLEY-USMAR, V., DAVIES, K., DENNERY, P. A., FORMAN, H., GRISHAM, M. B., MANN, G. E., MOORE, K., L, J., II & ISCHIROPOULOS, H. 2012a. Measuring reactive oxygen and nitrogen species with fluorescent probes: challenges and limitations. *Free Radical Biology and Medicine,* 52.
KALYANARAMAN, B., DARLEY-USMAR, V., DAVIES, K. J. A., DENNERY, P. A., FORMAN, H. J., GRISHAM, M. B., MANN, G. E., MOORE, K., ROBERTS, L. J. & ISCHIROPOULOS, H. 2012b. Measuring reactive oxygen and nitrogen species with fluorescent probes: challenges and limitations. *Free radical biology & medicine,* 52**,** 1-6.
KAM, W. W. & BANATI, R. B. 2013. Effects of ionizing radiation on mitochondria. *Free radical biology & medicine,* 65C**,** 607-619.
KARNKOWSKA, A., VACEK, V., ZUBÁČOVÁ, Z., TREITLI, S. C., PETRŽELKOVÁ, R., EME, L., NOVÁK, L., ŽÁRSKÝ, V., BARLOW, L. D., HERMAN, E. K., SOUKAL, P., HROUDOVÁ, M., DOLEŽAL, P., STAIRS, C. W., ROGER, A. J., ELIÁŠ, M., DACKS, J. B., VLČEK, Č. & HAMPL, V. A Eukaryote without a Mitochondrial Organelle. *Current Biology,* 26**,** 1274-1284.
KEIJ, J. F., BELL-PRINCE, C. & STEINKAMP, J. A. 2000. Staining of mitochondrial membranes with 10-nonyl acridine orange MitoFluor Green, and MitoTracker Green is affected by mitochondrial membrane potential altering drugs. *Cytometry,* 39**,** 203-210.
KHOLMUKHAMEDOV, A., SCHWARTZ, J. M. & LEMASTERS, J. J. 2013a. Mitotracker probes and mitochondrial membrane potential. *Shock,* 39**,** 543.
KHOLMUKHAMEDOV, A., SCHWARTZ, J. M. & LEMASTERS, J. J. 2013b. MitoTracker Probes and Mitochondrial Membrane Potential. *Shock (Augusta, Ga.),* 39**,** 543-543.
KUZNETSOV, A. V., TROPPMAIR, J. & SUCHER, R. 2006. Mitochondrial subpopulations and heterogeneity revealed by confocal imaging: possible physiological role? *… et Biophysica Acta (BBA …*.

LEACH, J. K., VAN TUYLE, G., LIN, P.-S., SCHMIDT-ULLRICH, R. & MIKKELSEN, R. B. 2001. Ionizing Radiation-induced, Mitochondria-dependent Generation of Reactive Oxygen/Nitrogen. *Cancer Research,* 61**,** 3894-3901.

LEMASTERS, J. J. & RAMSHESH, V. K. 2007. Imaging of Mitochondrial Polarization and Depolarization with Cationic Fluorophores. *Methods in Cell Biology.* Academic Press.

MASAO SUZUKI, N. U. 2015. Cell-killing effect by the targeted cytoplasmic irradiation for normal human fibroblasts with monochromatic X-ray microbeams. *Photon Factory Activity Report* 33.

MIKKELSEN, R. B. & WARDMAN, P. 2003. Biological chemistry of reactive oxygen and nitrogen and radiation-induced signal transduction mechanisms. *Oncogene,* 22**,** 5734-5754.

MILLER, E. W., ALBERS, A. E., CHANG, C. J., PRALLE, A. & ISACOFF, E. Y. 2005. Boronate-Based Fluorescent Probes for Imaging Cellular Hydrogen Peroxide. *Journal of the American Chemical Society,* 127**,** 16652-16659.

MURPHY, MICHAEL P. 2009. How mitochondria produce reactive oxygen species. *Biochemical Journal,* 417**,** 1-13.

O'REILLY, C. M., FOGARTY, K. E., DRUMMOND, R. M., TUFT, R. A. & WALSH, J. V. 2003. Quantitative Analysis of Spontaneous Mitochondrial Depolarizations. *Biophysical Journal,* 85**,** 3350-3357.

PAGLIARINI, D. J. & RUTTER, J. 2013. Hallmarks of a new era in mitochondrial biochemistry. *Genes & Development,* 27**,** 2615-2627.

PENDERGRASS, W., WOLF, N. & POOT, M. 2004. Efficacy of MitoTracker Green™ and CMXrosamine to measure changes in mitochondrial membrane potentials in living cells and tissues. *Cytometry Part A,* 61A**,** 162-169.

PERRY, S. W., NORMAN, J. P., BARBIERI, J., BROWN, E. B. & GELBARD, H. A. 2011. Mitochondrial membrane potential probes and the proton gradient: a practical usage guide. *BioTechniques,* 50**,** 98-115.

POLSTER, B. M., NICHOLLS, D. G., GE, S. X. & ROELOFS, B. A. 2014. Use of Potentiometric Fluorophores in the Measurement of Mitochondrial Reactive Oxygen Species. *Methods in enzymology,* 547**,** 225-250.

PRAKASH, A. & DOUBLIÉ, S. 2015. Base Excision Repair in the Mitochondria. *Journal of cellular biochemistry,* 116**,** 1490-1499.

R.L. WARTERS, K. G. H. 1977. Radionuclide Toxicity in Cultured Mammalian Cells: Elucidation of the Primary Site for Radiation-Induced Division Delay. *Radiation Research,* 69**,** 348-358.

RAHA, S. & ROBINSON, B. H. Mitochondria, oxygen free radicals, disease and ageing. *Trends in Biochemical Sciences,* 25**,** 502-508.

RAPPOLE, C. A., MITRA, K. & WEN, H. 2012. Dynamic fluorescence imaging of the free radical products of X-ray absorption in live cells. *Optical Nanoscopy,* 1**,** 5.

REINDL, J., GIRST, S., WALSH, D. W. M., GREUBEL, C., SCHWARZ, B., SIEBENWIRTH, C., DREXLER, G. A., FRIEDL, A. A. & DOLLINGER, G. 2017. Chromatin organization revealed by nanostructure of irradiation induced γH2AX, 53BP1 and Rad51 foci. *Scientific Reports,* 7**,** 40616.

REISZ, J. A., BANSAL, N., QIAN, J., ZHAO, W. & FURDUI, C. M. 2014. Effects of Ionizing Radiation on Biological Molecules—Mechanisms of Damage and Emerging Methods of Detection. *Antioxidants & Redox Signaling,* 21**,** 260-292.

REMINGTON, S. J. 2011. Green fluorescent protein: A perspective. *Protein Science : A Publication of the Protein Society,* 20**,** 1509-1519.

RILEY, P. A. 1994. Free Radicals in Biology: Oxidative Stress and the Effects of Ionizing Radiation. *International Journal of Radiation Biology,* 65**,** 27-33.

RODRIGUEZ-CASTRO, K. I., HEVIA-URRUTIA, F. J. & STURNIOLO, G. C. 2015. Wilson's disease: A review of what we have learned. *World Journal of Hepatology,* 7**,** 2859-2870.

SABHARWAL, S. S. & SCHUMACKER, P. T. 2014. Mitochondrial ROS in cancer: initiators, amplifiers or an Achilles' heel? *Nat Rev Cancer,* 14**,** 709-721.

SCADUTO JR, R. C. & GROTYOHANN, L. W. 1999. Measurement of Mitochondrial Membrane Potential Using Fluorescent Rhodamine Derivatives. *Biophysical Journal,* 76**,** 469-477.

SCHINDELIN, J., ARGANDA-CARRERAS, I., FRISE, E., KAYNIG, V., LONGAIR, M., PIETZSCH, T., PREIBISCH, S., RUEDEN, C., SAALFELD, S., SCHMID, B., TINEVEZ, J.-Y., WHITE, D. J., HARTENSTEIN, V., ELICEIRI, K., TOMANCAK, P. & CARDONA, A. 2012. Fiji: an open-source platform for biological-image analysis. *Nat Meth,* 9**,** 676-682.

SCHMID, T. E., GREUBEL, C., DOLLINGER, G. & SCHMID, E. 2017. The influence of reference radiation photon energy on high-LET RBE: comparison of human peripheral lymphocytes and human–hamster hybrid AL cells. *Radiation and Environmental Biophysics,* 56**,** 79-87.

SCHMITT, E. O., ANDREA; DINGFELDER, MICHAEL; FRIEDLAND, WERNER; KUNDRAT, PAVEL; BAIOCCO, GIORGIO. Track structure based modelling of light ion radiation effects on nuclear and mitochondrial DNA. Committee on Space Research 41, 2016 Istanbul.

SCHWARZLÄNDER, M., FRICKER, M. D., MÜLLER, C., MARTY, L., BRACH, T., NOVAK, J., SWEETLOVE, L. J., HELL, R. & MEYER, A. J. 2008. Confocal imaging of glutathione redox potential in living plant cells. *Journal of Microscopy,* 231**,** 299-316.

SCHWARZLÄNDER, M., FRICKER, M. D. & SWEETLOVE, L. J. 2009. Monitoring the in vivo redox state of plant mitochondria: Effect of respiratory inhibitors, abiotic stress and assessment of recovery from oxidative challenge. *Biochimica et Biophysica Acta (BBA) - Bioenergetics,* 1787**,** 468-475.

SCHWARZLÄNDER, M., MURPHY, M. P., DUCHEN, M. R., LOGAN, D. C., FRICKER, M. D., HALESTRAP, A. P., MÜLLER, F. L., RIZZUTO, R., DICK, T. P., MEYER, A. J. & SWEETLOVE, L. J. Mitochondrial ‘flashes’: a radical concept repHined. *Trends in Cell Biology,* 22**,** 503-508.

SHAO, C., FOLKARD, M. & MICHAEL, B. D. 2004. Targeted cytoplasmic irradiation induces bystander responses. *PNAS*.

SHEN, N., DATTA, D., SCHAFFER, C. B., LEDUC, P., INGBER, D. E. & MAZUR, E. 2005. Ablation of cytoskeletal filaments and mitochondria in live cells using a femtosecond laser nanoscissor. *Mech. Chem. Biosyst,* 2**,** 17-25.

SHIMADA, T., WATANABE, W., MATSUNAGA, S., HIGASHI, T., ISHII, H., FUKUI, K., ISOBE, K. & ITOH, K. 2005. Intracellular disruption of mitochondria in a living HeLa cell with a 76-MHz femtosecond laser oscillator. *Optics Express,* 13**,** 9869-9880.

SIEBENWIRTH, C., GREUBEL, C., DREXLER, S. E., GIRST, S., REINDL, J., WALSH, D. W. M., DOLLINGER, G., FRIEDL, A. A., SCHMID, T. E. & DREXLER, G. A. 2015. Determination of the accuracy for targeted irradiations of cellular substructures at SNAKE. *Nuclear Instruments and Methods in Physics Research Section B: Beam Interactions with Materials and Atoms,* 348**,** 137-142.

SIEMENS, A., WALTER, R., LIAW, L. H. & BERNS, M. W. 1982. Laser-stimulated fluorescence of submicrometer regions within single mitochondria of rhodamine-treated myocardial cells in culture. *Proceedings of the National Academy of Sciences,* 79**,** 466-470.

SORIEUL, S., ALFAURT, P., DAUDIN, L., SERANI, L. & MORETTO, P. 2014. Aifira: An ion beam facility for multidisciplinary research. *Nuclear Instruments and Methods in Physics Research Section B: Beam Interactions with Materials and Atoms,* 332**,** 68-73.

STARK, G. 1991. The effect of ionizing radiation on lipid membranes. *Biochimica et Biophysica Acta (BBA) - Reviews on Biomembranes,* 1071**,** 103-122.

TANAKA, Y. 1969. Effect of the ruby laser microbeam on mitochondria of KB cells supravitally stained by pinacyanol. *The Journal of cell biology*.

TARTIER, L., GILCHRIST, S., BURDAK-ROTHKAMM, S., FOLKARD, M. & PRISE, K. M. 2007. Cytoplasmic Irradiation Induces Mitochondrial-Dependent 53BP1 Protein Relocalization in Irradiated and Bystander Cells. *Cancer research,* 67**,** 5872-5879.

TORMOS, KATHRYN V. & CHANDEL, NAVDEEP S. 2011. Seeing the Light: Probing ROS In Vivo Using Redox GFP. *Cell Metabolism,* 14**,** 720-721.

VEVEA, J. D., ALESSI WOLKEN, D. M., SWAYNE, T. C., WHITE, A. B. & PON, L. A. 2013. Ratiometric biosensors that measure mitochondrial redox state and ATP in living yeast cells. *Journal of visualized experiments : JoVE***,** 10.3791/50633.

WALDREN, C. A. 2004. Classical radiation biology dogma, bystander effects and paradigm shifts. *Human & experimental toxicology,* 23**,** 95-100.

WANG, C. & YOULE, R. J. 2009. The Role of Mitochondria in Apoptosis(). *Annual review of genetics,* 43**,** 95-118.

WANG, W., GONG, G., WANG, X., WEI-LAPIERRE, L., CHENG, H., DIRKSEN, R. & SHEU, S.-S. 2016. Mitochondrial Flash: Integrative Reactive Oxygen Species and pH Signals in Cell and Organelle Biology. *Antioxidants & Redox Signaling,* 25**,** 534-549.

WATANABE, W., ARAKAWA, N. & MATSUNAGA, S. 2004. Femtosecond laser disruption of subcellular organelles in a living cell. *Optics Express*.

WATANABE, W., MATSUNAGA, S., SHIMADA, T., HIGASHI, T., FUKUI, K. & ITOH, K. 2005. Femtosecond laser disruption of mitochondria in living cells. *Medical Laser Application,* 20**,** 185-191.

WOOLLEY, J. F., STANICKA, J. & COTTER, T. G. 2013. Recent advances in reactive oxygen species measurement in biological systems. *Trends in biochemical sciences,* 38**,** 556-565.

WU, L.-J., RANDERS-PEHRSON, G., XU, A., WALDREN, C. A., GEARD, C. R., YU, Z. & HEI, T. K. 1999. Targeted cytoplasmic irradiation with alpha particles induces mutations in mammalian cells. *Proceedings of the National Academy of Sciences of the United States of America,* 96**,** 4959-4964.

YALINKILIC, O. & ENGINAR, H. 2008. Effect of X-Radiation on Lipid Peroxidation and Antioxidant Systems in Rats Treated with Saponin-containing Compounds. *Photochemistry and Photobiology,* 84**,** 236-242.

YAMAGUCHI, M. & KASHIWAKURA, I. 2013. Role of Reactive Oxygen Species in the Radiation Response of Human Hematopoietic Stem/Progenitor Cells. *PLOS ONE,* 8**,** e70503.

ZHANG, B., DAVIDSON, M. M. & HEI, T. K. 2014. Mitochondria regulate DNA damage and genomic instability induced by high LET radiation. *Life sciences in space research,* 1**,** 80-88.

ZHANG, B., DAVIDSON, M. M., ZHOU, H., WANG, C., WALKER, W. F. & HEI, T. K. 2013. Cytoplasmic irradiation results in mitochondrial dysfunction and DRP1-dependent mitochondrial fission. *Cancer research,* 73**,** 6700-6710.

ZIELONKA, J. & KALYANARAMAN, B. 2010. Hydroethidine- and Mito-SOX-derived red fluorescence is not a reliable indicator of intracellular superoxide formation: Another inconvenient truth. *Free radical biology & medicine,* 48**,** 983-1001.

ZIRKLE, R. E. & BLOOM, W. 1953. Irradiation of parts of individual cells. *Science,* 117**,** 487-493.

ZONG, W.-X., RABINOWITZ, JOSHUA D. & WHITE, E. Mitochondria and Cancer. *Molecular Cell,* 61**,** 667-676.

ZOROV, D. B., JUHASZOVA, M. & SOLLOTT, S. J. 2014. Mitochondrial Reactive Oxygen Species (ROS) and ROS-Induced ROS Release. *Physiological Reviews,* 94**,** 909-950.